

Science and Technology of Nuclear Installations

Mechanical Properties in Nuclear Installation and the Relevant Measurement Methods

Guest Editors: Yan Yang, Alejandro Clause, Leon Cizelj, Xing Chen, and Parashuram Sahoo





Mechanical Properties in Nuclear Installation and the Relevant Measurement Methods

Science and Technology of Nuclear Installations

Mechanical Properties in Nuclear Installation and the Relevant Measurement Methods

Guest Editors: Yan Yang, Alejandro Clause, Leon Cizelj,
Xing Chen, and Parashuram Sahoo



Copyright © 2016 Hindawi Publishing Corporation. All rights reserved.

This is a special issue published in “Science and Technology of Nuclear Installations.” All articles are open access articles distributed under the Creative Commons Attribution License, which permits unrestricted use, distribution, and reproduction in any medium, provided the original work is properly cited.

Editorial Board

Nusret Aksan, Switzerland
Won P. Baek, Republic of Korea
Stephen M. Bajorek, USA
George Bakos, Greece
Jozsef Banati, Sweden
Giovanni B. Bruna, France
Nikola Čavlina, Croatia
Leon Cizelj, Slovenia
Alejandro Clausse, Argentina
Francesco D' Auria, Italy
Marcos P. de Abreu, Brazil
Mark Deinert, USA
Giovanni Dell'Orco, France
Cesare Frepoli, USA
Michel Giot, Belgium
Valerio Giusti, Italy
Horst Glaeser, Germany
Ali Hainoun, Syria
Tim Haste, France

Keith E. Holbert, USA
Toshimitsu Homma, Japan
Yacine Kadi, Republic of Korea
Tomasz Kozlowski, USA
Tomoaki Kunugi, Japan
Mike Kuznetsov, Germany
Jérôme Lamontagne, France
Jiri Macek, Czech Republic
Annalisa Manera, USA
Borut Mavko, Slovenia
Oleg Melikhov, Russia
Rafael Miró, Spain
Jozef Misak, Czech Republic
Michio Murase, Japan
Rahim Nabbi, Germany
Michael I. Ojovan, UK
D. Paladino, Switzerland
Manmohan Pandey, India
Yuriy Parfenov, Russia

L. Podofillini, Switzerland
Yves Pontillon, France
Nik Popov, Canada
Piero Ravetto, Italy
Enrico Sartori, France
Carlo Sborchia, France
Massimo Sepielli, Italy
Arkady Serikov, Germany
James F. Stubbins, USA
Iztok Tiselj, Slovenia
Rizwan Uddin, USA
E. Ušpuras, Lithuania
Hidemasa Yamano, Japan
Yanko Yanev, Bulgaria
Enrico Zio, Italy
Massimo Zucchetti, Italy
Hyeong-Yeon Lee, Republic of Korea

Contents

Mechanical Properties in Nuclear Installation and the Relevant Measurement Methods

Yan Yang, Alejandro Clausse, Leon Cizelj, Xing Chen, and Parashuram Sahoo
Volume 2016, Article ID 1948507, 2 pages

Effects of a Mixed Zone on TGO Displacement Instabilities of Thermal Barrier Coatings at High Temperature in Gas-Cooled Fast Reactors

Jian Wang, Jun Ding, Kun Song, Song Chen, and Xia Huang
Volume 2016, Article ID 9071237, 10 pages

Nondestructive Evaluation of Functionally Graded Subsurface Damage on Cylinders in Nuclear Installations Based on Circumferential SH Waves

Zhen Qu, Xiaoqin Shen, and Xiaoshan Cao
Volume 2016, Article ID 3035180, 7 pages

Development of a Composite Technique for Preconditioning of 41Cr4 Steel Used as Gear Material: Examination of Its Microstructural Characteristics and Properties

Jianjun Hu, Chaoping Ma, Hongbin Xu, Ning Guo, and Tianfeng Hou
Volume 2016, Article ID 5852328, 6 pages

The Definition Method and Optimization of Atomic Strain Tensors for Nuclear Power Engineering Materials

Xiangguo Zeng, Ying Sheng, Huayan Chen, and Tixin Han
Volume 2016, Article ID 4649870, 9 pages

A Comparative Study for Modeling Displacement Instabilities due to TGO Formation in TBCs of High-Temperature Components in Nuclear Power Plant

Xia Huang, Jian Wang, Kun Song, Feng Zhang, Tong Yi, and Jun Ding
Volume 2016, Article ID 2857065, 16 pages

Effect of Chemical Corrosion on the Mechanical Characteristics of Parent Rocks for Nuclear Waste Storage

Tielin Han, Junping Shi, Yunsheng Chen, and Zhihui Li
Volume 2016, Article ID 7853787, 11 pages

Editorial

Mechanical Properties in Nuclear Installation and the Relevant Measurement Methods

Yan Yang,¹ Alejandro Clause,² Leon Cizelj,³ Xing Chen,⁴ and Parashuram Sahoo⁵

¹Chongqing University of Technology, Chongqing, China

²National University of Central Buenos Aires, Buenos Aires, Argentina

³Jožef Stefan Institute, Ljubljana, Slovenia

⁴University of Utah, Salt Lake City, UT, USA

⁵Indira Gandhi Centre for Atomic Research, Tamil Nadu, India

Correspondence should be addressed to Yan Yang; yangyan@cqut.edu.cn

Received 26 October 2016; Accepted 27 October 2016

Copyright © 2016 Yan Yang et al. This is an open access article distributed under the Creative Commons Attribution License, which permits unrestricted use, distribution, and reproduction in any medium, provided the original work is properly cited.

The application of nuclear technology is currently spreading over the world. Given the possibility of considerable risks, the lifetime performance and especially the safety of nuclear installation are raising large concerns to human society. Therefore, the assessment of mechanical properties and development of relevant measurement methods in nuclear installations are becoming extraordinarily important and are being intensively investigated. This field of research usually covers a wide range of subtopics, with the main focus on both fundamental sciences and advanced technologies for boosting the study of mechanical properties of nuclear installation and its related measurement. For example, fracture mechanics is useful to predict the temporal and long-term reliability of nuclear reactors under aggressive loads. Advanced functional materials (e.g., alloys and thermal barriers coatings) with superior thermal and mechanical resistance to harsh environment can be applied in nuclear installations. Also, it is of significant interest to analyze and characterize these materials by using state-of-the-art measurement methods.

Following up with the special issue “Advanced Measuring (Instrumentation) Methods for Nuclear Installations” published in the year of 2012, this special issue continues to demonstrate the most recent research progress in mechanical properties in nuclear installations and their relevant measurement methods. Six papers are included in this special issue covering a wide range of nuclear installation related topics.

In the paper “Effects of a Mixed Zone on TGO Displacement Instabilities of Thermal Barrier Coatings at High Temperature in Gas-Cooled Fast Reactors,” thermally grown

oxide has been studied as suitable protective coatings, offering thermal insulation, heat resistance, and corrosion resistance for Generation IV nuclear energy systems. The effects of mixed zone on the displacement instability of thermally grown oxide were assessed. Quantitative data show that mixed zone formation induces an enormous stress in thermally grown oxide, resulting in a sharp change of displacement compared to the alumina layer. The displacement instability increases with an increase in the mixed zone growth rate, growth strain, and thickness. Thus, the formation of a mixed zone accelerates the failure of thermally grown oxide, which is in agreement with previous experimental observations. These results provide data for the understanding of thermal barrier coatings failure mechanisms associated with mixed zone formation and of how to prolong working life of surface coating for gas cooled fast reactors.

The paper “Development of a Composite Technique for Preconditioning of 41Cr4 Steel Used as Gear Material: Examination of Its Microstructural Characteristics and Properties” reports a new composite technique to process commercial 41Cr4 steel. In this method, an intermediate layer was introduced firstly at the 41Cr4 steel surface by traditional carburizing and nitriding. Then a hard Cr coating was brush-plated on the intermediate layer. Finally, the coating layer was modified by high current pulsed electron beam (HCPEB), followed by quenching and subsequent tempering treatment. The microstructure, mechanical properties, and fracture behavior were characterized. The results show that a nanocrystalline Cr coating is formed at the 41Cr4 steel

surface by the treatment of the new composite technique. Such nanocrystalline Cr coating has acceptable hardness and high corrosion resistance performance, which satisfies the demands of the gears working under high speed and corrosive environment. The composite process proposed in this study is considered as a new prospect method due to the multifunction layer design on the gear surface. In summary, a broad range of topics relating to the mechanical properties and nondestructive testing of advanced materials have been collected and presented in this special issue, including both theoretical models and experimental testing methods. These works are expected to be of great interest to scholars in this field.

In the work “The Definition Method and Optimization of Atomic Strain Tensors for Nuclear Power Engineering Materials”, a common measure of deformation between atomic scale simulations and the continuum framework is provided and the strain tensors for multiscale simulations are defined. In order to compute the deformation gradient of any atom, the weight function is proposed to eliminate the different contributions within the neighbor atoms which have different distances to atom, and the weighted least squares error optimization model is established to seek the optimal coefficients of the weight function and the optimal local deformation gradient of each atom. The optimization model involves more than 9 parameters. To guarantee the reliability of subsequent parameters identification result and lighten the calculation workload of parameters identification, an overall analysis method of parameter sensitivity and an advanced genetic algorithm are also developed.

“Effect of Chemical Corrosion on the Mechanical Characteristics of Parent Rocks for Nuclear Waste Storage” is a paper with the research interest of nuclear waste disposal repository. Granite was selected as the candidate of parent rocks for nuclear waste storage. The physical and mechanical properties of variation regularity immersed in various chemical solutions were analyzed. Meanwhile, the damage variable based on the variation in porosity was used in the quantitative analysis of chemical damage deterioration degree. Experimental results show that granite has a significant weakening tendency after chemical corrosion. The fracture toughness, splitting tensile strength, and compressive strength all demonstrate the same deteriorating trend with chemical corrosion time. However, a difference exists in the deterioration degree of the mechanical parameters; that is, the deterioration degree of fracture toughness is the greatest followed by those of splitting tensile strength and compressive strength, which are relatively smaller. Strong acid solutions may aggravate chemical damage deterioration in granite. By contrast, strong alkaline solutions have a certain inhibiting effect on chemical damage deterioration. The chemical solutions that feature various compositions may have different effects on chemical damage degree; that is, ions have a greater effect on the chemical damage in granite than ions.

“A Comparative Study for Modeling Displacement Instabilities due to TGO Formation in TBCs of High-Temperature Components in Nuclear Power Plant” reports two numerical simulation methods for modeling displacement instabilities around a surface groove in a metal substrate used in nuclear

power plant. The amplitude change in the groove, the downward displacement at the base node, and the groove displacement at the periphery were simulated using ABAQUS to compare the results from two methods, as well as the tangential stress in the elements at the groove base and periphery. The comparison showed that for the tangential stress two methods were in close agreement for all thermal cycles. It is concluded that the present work’s numerical simulation scheme worked better with a thinner thermally grown oxide layer than the classic method and could overcome the limitation of thermally grown oxide thickness by simulating any thickness.

In nuclear engineering, nondestructive evaluation and detection of the evaluation of the subsurface damage region are of great importance to ensure the safety of nuclear installations. “Nondestructive Evaluation of Functionally Graded Subsurface Damage on Cylinders in Nuclear Installations Based on Circumferential SH Waves” proposes the use of circumferential horizontal shear waves SH to detect mechanical properties of subsurface regions of damage on cylindrical structures. The regions of surface damage are considered to be functionally graded material and the cylinder is considered to be a layered structure. The Bessel functions and the power series technique are employed to solve the governing equations. By analyzing the SH waves in the 12Cr-ODS ferritic steel cylinder, which is frequently applied in the nuclear installations, we discuss the relationship between the phase velocities of SH waves in the cylinder with subsurface layers of damage and the mechanical properties of the subsurface damaged regions. The results show that the subsurface damage could lead to decrease of the SH waves’ phase velocity. The gradient parameters, which represent the degree of subsurface damage, can be evaluated by the variation of the SH waves’ phase velocity. Research results of this study can provide theoretical guidance in nondestructive evaluation for use in the analysis of the reliability and durability of nuclear installations.

In summary, a broad range of topics related to the mechanical properties in nuclear installations and their measurement methods have been collected and presented in this special issue, including both theoretical models and experimental testing methods. These works are expected to be of great interest to scholars in this field.

*Yan Yang
Alejandro Clause
Leon Cizelj
Xing Chen
Parashuram Sahoo*

Research Article

Effects of a Mixed Zone on TGO Displacement Instabilities of Thermal Barrier Coatings at High Temperature in Gas-Cooled Fast Reactors

Jian Wang,¹ Jun Ding,^{1,2} Kun Song,¹ Song Chen,¹ and Xia Huang¹

¹College of Mechanical Engineering, Chongqing University of Technology, Chongqing 400054, China

²Key Laboratory of Manufacture and Test Techniques for Automobile Parts, Ministry of Education, Chongqing 400054, China

Correspondence should be addressed to Xia Huang; huangxia@cqut.edu.cn

Received 1 June 2016; Revised 20 September 2016; Accepted 4 October 2016

Academic Editor: Michel Giot

Copyright © 2016 Jian Wang et al. This is an open access article distributed under the Creative Commons Attribution License, which permits unrestricted use, distribution, and reproduction in any medium, provided the original work is properly cited.

Thermally grown oxide (TGO), commonly pure α -Al₂O₃, formed on protective coatings acts as an insulation barrier shielding cooled reactors from high temperatures in nuclear energy systems. Mixed zone (MZ) oxide often grows at the interface between the alumina layer and top coat in thermal barrier coatings (TBCs) at high temperature dwell times accompanied by the formation of alumina. The newly formed MZ destroys interface integrity and significantly affects the displacement instabilities of TGO. In this work, a finite element model based on material property changes was constructed to investigate the effects of MZ on the displacement instabilities of TGO. MZ formation was simulated by gradually changing the metal material properties into MZ upon thermal cycling. Quantitative data show that MZ formation induces an enormous stress in TGO, resulting in a sharp change of displacement compared to the alumina layer. The displacement instability increases with an increase in the MZ growth rate, growth strain, and thickness. Thus, the formation of a MZ accelerates the failure of TBCs, which is in agreement with previous experimental observations. These results provide data for the understanding of TBC failure mechanisms associated with MZ formation and of how to prolong TBC working life.

1. Introduction

A new concept in nuclear energy systems, known as Generation IV, was proposed to meet future energy needs during the Generation IV International Forum in 2012. Generation IV nuclear reactors have a number of advantages compared to presently used nuclear reactors, including greater safety, dependability, durability, cost, and nonproliferation, and could help eliminate the use of plutonium and eventually lead to nuclear disarmament [1]. The Gas-Cooled Fast Reactor is one of the most researched concepts of Generation IV. It uses helium as a coolant and usually works under thermal cycle conditions with an external temperature of 850°C, which could even increase to a maximum of 1250°C. The ceramic materials used in the Gas-Cooled Fast Reactor must possess a high heat resistance, density, and thermal conductivity in order to protect the helium turbine components from high temperatures. Further, these ceramics should be corrosion resistant against a helium gas flow at speeds of 280 m/s

[2]. thermal barrier coatings (TBCs) have therefore been proposed as suitable protective coatings, offering thermal insulation, heat resistance, and corrosion resistance.

A typical TBC system usually consists of four components: (1) the ceramic top coat, (2) the bond coat (BC), (3) the thermally grown oxide (TGO), and (4) the metal substrate [3, 4]. The fast development of advanced engines has led to an increase in working temperatures, resulting in increased requirements from substrate materials; however, advances in substrate materials can hardly keep pace with the increase in demands. Therefore, the use of TBCs for thermal insulation is both convenient and efficient. TBCs play an important role in the thermal protection of the substrate components, since they are able to offer a temperature differential of up to 300°C [5]. As a result, various studies have been performed worldwide regarding the failure mechanisms and lifespan of TBCs.

The performance and durability of TBCs are controlled by both internal (i.e., sintering effects and residual stresses)

and external (i.e., actual service conditions such as calcium magnesium alumina-silicate attack, erosion, impact damage, and countermeasures [6]) factors. Karlsson and Evans [7] found that TGO was the main factor leading to TBC failure. In their studies, they developed three-layer TBCs without a ceramic layer to assess the instabilities caused by TGO growth and found that the constituent properties had a major influence on the instabilities. The growth of TGO at elevated temperatures can lead to a large compressive stress of up to 3 to 6 GPa [4]. Hsueh and Fuller [8] revealed the analytical expression of TGO growth stress in light of elastic-plastic mechanics and Euler beam theory, which predicted the stress field in each layer. Ding et al. [9] investigated the displacement instability of TGO through a novel quantitative method which could model TGO growth without the limitation of TGO thickness. Their work shows a good agreement with experimental observations, even at TGO thicknesses of up to 5 μm .

However, all of the above mentioned studies considered the TGO material in TBCs as a pure alumina layer, namely, Al_2O_3 . Nevertheless, a TGO layer is usually composed of various oxide phases such as NiAl_2O_4 , NiO , and Cr_2O_3 . The outward aluminum diffusion and uptake of zirconia will lead to the formation of a $(\text{Al}, \text{Cr})_2\text{O}_3$ mixed zone (MZ). Liu et al. [10] studied the microstructural evolution at the interfaces of TBCs by transmission electron microscopy during isothermal oxidation and found that the TGO layer would split into two sublayers, one of which consists of a mixture of $\alpha\text{-Al}_2\text{O}_3$, Cr_2O_3 , and $\text{Ni}(\text{Al}, \text{Cr})_2\text{O}_4$ and the other of dense Al_2O_3 and Cr_2O_3 . Their work helps clarify the failure mechanism due to microstructural changes caused by chemical reactions between the related elements. Hernandez et al. [11] studied TGO creep and the initiation of a class of fatigue cracks in TBCs using a thermal gradient mechanical fatigue test. In their study, they considered the MZ as a part of TGO layer and examined and quantified the thermomechanical performance of TGO through a finite element (FE) modelling method. Their results indicated that the stress-redistribution caused by creep can result in tensile stress in the TGO and that the stress was large enough to initiate cracks. Lv et al. [12] adopted a spherical shell model to investigate the effects of sintering and mixed oxide (MO) growth on interface cracking of TBCs at high temperatures and concluded that the smaller growth rate of MOs would delay interface cracking. Xu et al. [13] studied the interfacial fracture mechanism associated with MO growth in TBCs and found that MO plays an important role on interface integrity; high growth rates of MO and high coverage of MO would both accelerate the initiation and propagation of interface cracks. Braue et al. [14, 15] investigated the microstructural evolution of an alumina-zirconia MZ in a TBC system using analytical electron microscopy to investigate the instability of the MZ/TBC interface. Their experiments showed that the growth of a MZ occurred in three stages, namely, the formation of MZ during TBC spraying, followed by a constant MZ composition due to $\alpha\text{-Al}_2\text{O}_3$ densification, and resumed growth due to destabilization of TBCs. Nevertheless, these experimental results hardly reflect the real case scenario of TBCs under their extreme service conditions. Review of previous studies shows

that few have addressed the simulation of MZ formation and therefore the effects of this on the durability and performance of TBCs remain unknown.

Herein, the effects of MZ formation on the displacement instabilities of TGO have been investigated through a FE model. The thermal cycle growth of a four-component (alumina–MZ–alumina–MZ) TGO layer was simulated with the *USDFLD* and *UEXPAN* user subroutines in ABAQUS. MZ growth rate, growth strain, and thickness were studied to assess the influence of MZ on TGO displacement instabilities. The simulation results indicated that a MZ would cause a drastic change of displacement compared with the alumina layer and induced an enormous stress in TGO. An increase in MZ growth rate, growth strain, and thickness would lead to an increase in TGO displacement instabilities. On the other hand, a MZ might accelerate TBC failure. The results of this study reveal that the degradation mechanism of TBCs is related to MZ formation and can be used as a reference to improve the durability of and extend the service life of TBCs.

2. Finite Element Model

2.1. Geometry and Model Description. In order to investigate the displacement instability of TGO due to the formation of a MZ, a two-dimensional plane model was established as shown in Figure 1. The simplified TBC model takes into account three layers, namely, the TGO layer, a BC, and the super alloy substrate. The TGO layer is divided into two sublayers: an alumina layer adjacent to the BC and a MZ above it [11]. An initial alumina layer and an initial MZ layer are constructed to model oxidation during the spraying process. The periodic boundary condition is imposed on the FE model to simulate the random existence of the imperfections in TBC system. The command *EQUATION* in ABAQUS is used to impose x displacement in horizontal axis in order to keep the same displacement in x direction for the nodes on the right side. The same method is used to constrain the y displacement of the nodes at the bottom side to avoid the bending deformation induced by thermal expansion during the period of cooling and reheating. The first-order generalized plane strain elements, CPEG4 in ABAQUS software, are used to construct the FE model, and the number of elements is checked by the dependency of mesh. Each thermal cycle consisted of three steps: a 600 s cooling down from 1200°C to ambient temperature, heating to the highest temperature in 600 s, and holding of this temperature for 1800 s. Table 1 displays the material property configuration for the FE model.

2.2. TGO Growth. TGO usually forms during high temperature service conditions. The inward diffusion of oxidants and outward diffusion of aluminum leads to a reaction zone on the top coat/BC interface. The chemical reaction can be displayed as $4\text{Al} + 3\text{O}_2 \rightarrow 2\text{Al}_2\text{O}_3$. When diffused Ni and Cr from the BC react with O, MZ growth commences. The formation of MZ can be indicated by $[\text{Ni}] + \alpha\text{-Al}_2\text{O}_3 + \text{Cr}_2\text{O}_3 + [\text{O}] \rightarrow \text{Ni}(\text{Al}, \text{Cr})_2\text{O}_4$. An initial TGO layer usually forms during the manufacturing stage and the newly formed TGO usually has a columnar grain structure. As shown in

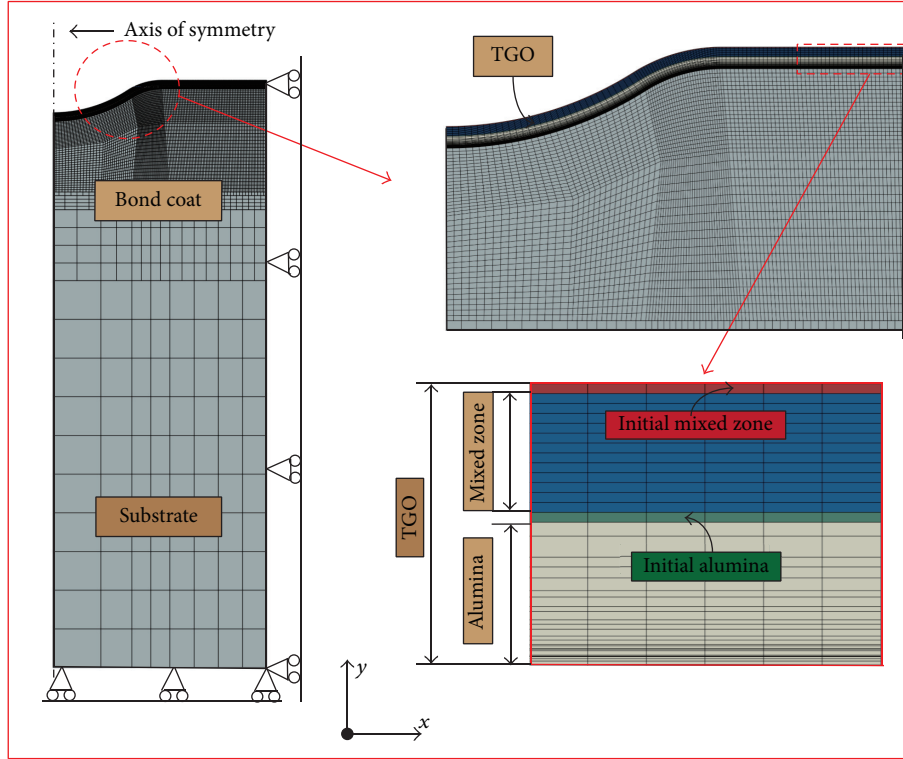


FIGURE 1: The geometry and boundary conditions used in the FE model analysis.

TABLE 1: Material property configuration for the finite element model.

Material property	Substrate	Bond coat	Alumina	Mixed zone [13]
Elastic modulus, E (GPa)	140	140	390	100
Poisson ratio, ν	0.3	0.3	0.2	0.3
Thermal expansion coefficient, α (10^{-6})	15	15	9	8

Figure 2, the reactions at the grain boundary gaps result in an increase in TGO length, while the TGO formed at the TGO/BC interface leads to thickening of the TGO layer. As a result, TGO grows in two directions, lateral growth and normal growth, during thermal cycling. Consequently, the growth strain of TGO is considered as two components: ϵ_t and ϵ_g , where ϵ_t is normal growth strain on the TGO/BC interface and ϵ_g is the lateral growth strain parallel to the interface. The growth of TGO can be divided into three stages, as in previous experimental observations [14, 15]. The MZ forms during the initial thermal exposure stage and remains at this thickness for a considerable time due to the formation of a dense α - Al_2O_3 layer preventing the outward diffusion of Cr and Ni anions, while in the late stage, the outward diffusion of Cr and Ni from the BC induces MZ growth.

2.3. The Numerical Simulation Procedure. The simulation procedure of TGO growth is shown in Figure 3. The red layer represents the initial MZ whilst the green layer represents

the initial alumina layer. The dark blue layers, composed of 12 sub-layers of equal thickness due to the constant growth rate at long time intervals as experimentally observed [16, 17], represent the MZ, with a total thickness of $2\ \mu\text{m}$. The light brown layers represent the alumina layers, with 24 sublayers of varying thicknesses since alumina layer growth usually follows a parabolic line [4]. The simulation of TGO growth was divided into three stages to match previous experimental observations [14, 15]. Firstly, the initial alumina and MZ layers were assigned a material property each and the subsequent alumina and MZ layers were assigned a BC material property. Secondly, the 24 alumina thickening sublayers transformed into alumina layers from top to down during 24 thermal cycles. Thirdly, the 12 MZ sublayers began to turn into the material property of MZ upon varying thermal cycles to study the effect of MZ growth rate.

The alumina layer grows at a relatively slow rate compared with that of MZ. A number of experiments had found that the MZ growth rate is usually several times faster than that of alumina [14, 18]. Herein, we adopted the user subroutine *USDFLD* in ABAQUS to simulate the thickening of TGO, as in previous studies [9]. As for the lateral growth strain, the magnitude of the alumina growth strain, ϵ_{Al} , ranges from 10^{-4} to 5×10^{-3} as shown by experimental observations, while the normal growth strain of alumina is usually one-tenth that of the alumina lateral growth strain [7]. When it comes to MZ, the normal growth strain usually equals lateral growth strain [12, 13]. What is more, MZ usually grows several dozen times of alumina [14]. In this work, we selected $\epsilon_{\text{Al}} = 2.4 \times 10^{-3}$ as indicated by Xu et al. [13]. The lateral growth strain, ϵ_m , of

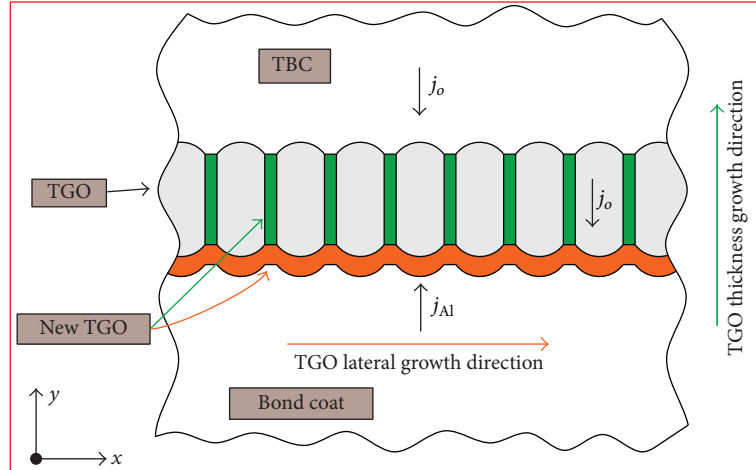


FIGURE 2: A schematic of TGO growth phenomena.

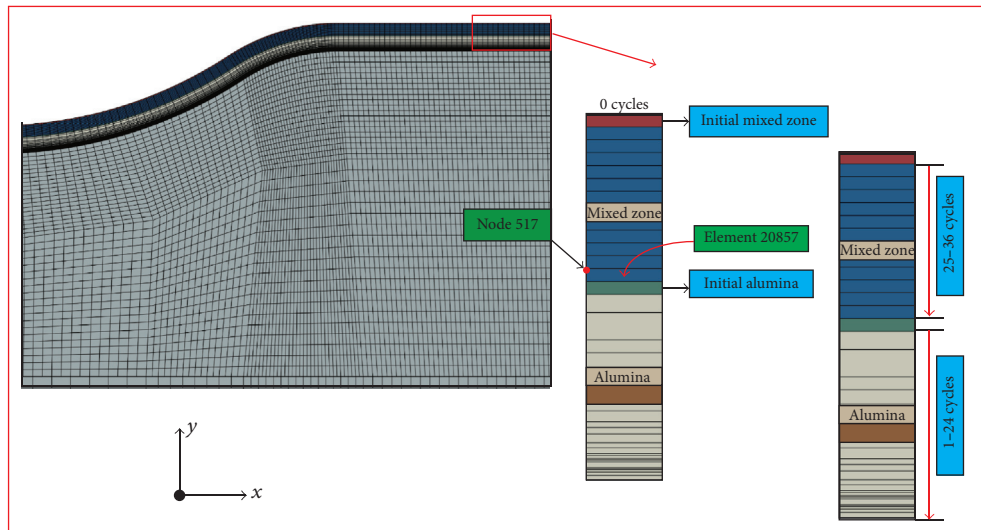


FIGURE 3: TGO thickening simulated by *USDFLD* in ABAQUS.

MZ was set as $\varepsilon_m = 2.4 \times 10^{-2}$, $\varepsilon_m = 4.8 \times 10^{-2}$, and $\varepsilon_m = 7.2 \times 10^{-2}$, which were 10, 20, and 30 times larger than ε_{Al} , respectively. During the simulation, the lateral growth strains were applied at high temperature period of each thermal cycle through user subroutine *UEXPAN* in ABAQUS, and no lateral growth strain was imposed at the cooling and reheating stages. The different lateral growth strains were implemented by user code in *UEXPAN*. The incremental thermal strains are applied to the corresponding elements during each thermal cycle to realize the lateral growth of alumina and MZ. For MZ thickness growth, the thickening strain is assumed equal to MZ lateral growth strain [13]. However, we used the material change method, as in our previous work [9], instead of MZ thickening strain. To study the effects of MZ thickness growth rate, MZ layers formed during each thermal cycle were assigned as one layer for each thermal cycle, two layers for each thermal cycle, three layers for each thermal cycle, and four layers for each thermal cycle. Thus, the thickness growth rate equals $v_1 = 0.2 \times 10^{-3}$ mm/h,

$v_2 = 0.4 \times 10^{-3}$ mm/h, $v_3 = 0.6 \times 10^{-3}$ mm/h, and $v_4 = 0.8 \times 10^{-3}$ mm/h when translating MZ formation during each thermal cycle into millimeters per hour. The specific research protocols were shown in Table 2. Analyses 1–4, 5–8, and 9–12 aimed to study the effect of MZ thickness growth rate on the displacement instability of TGO. Analyses 1, 5, and 9, 2, 6, and 10, 3, 7, and 11, and 4, 8, and 12 were set to investigate the effect of lateral growth strain on TGO displacement instability.

3. Results and Discussion

3.1. Effects of Mixed Zone Thickness Growth Rate. Previous studies assessing the displacement instability caused by TGO have usually regarded the TGO phase as a pure alumina layer. However, the TGO is mainly dense and uniform α - Al_2O_3 in the early stage of TBCs, then transforming to a MZ due to the depletion of aluminum [10, 14, 17]. The MZ is usually located between the top coat and the alumina layer [15, 18]. Herein, we established FE models with various MZ growth rates for

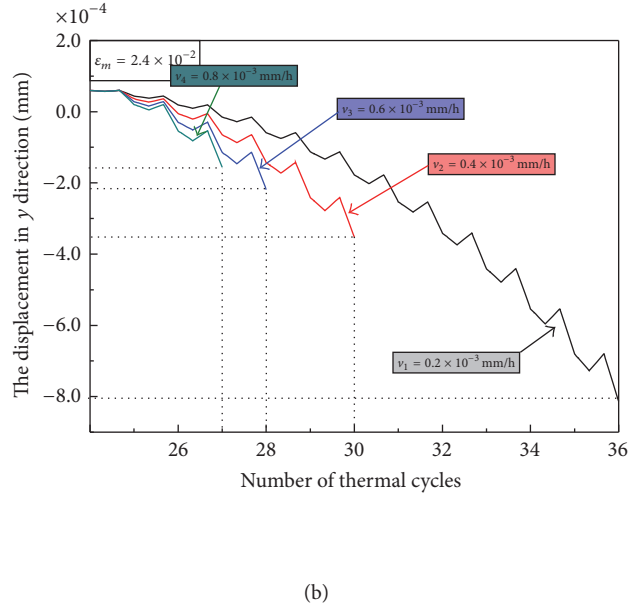
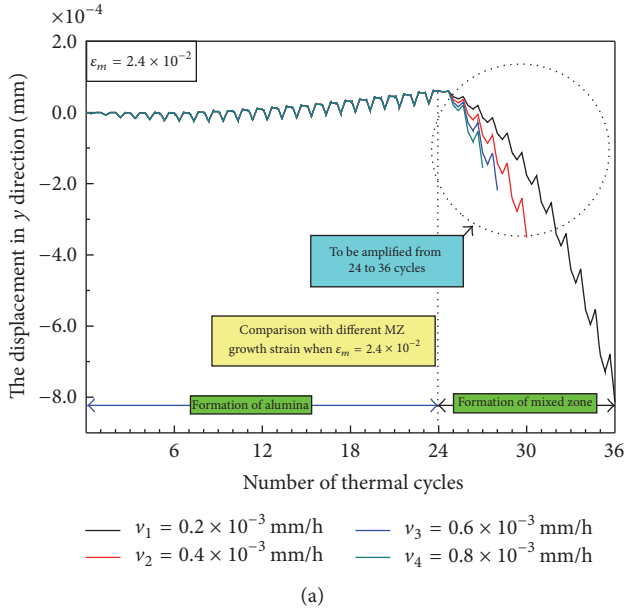


FIGURE 4: (a) The plot of displacement in y direction for node number 517 at the base of the surface groove against the number of thermal cycles when $\epsilon_m = 2.4 \times 10^{-2}$. (b) The details for the variation of displacement for the formation of MZ.

TABLE 2: Research protocols used in this paper.

Analysis	Element	Lateral growth strain, ϵ_m	Mixed zone growth rate, v (mm/h)
1			0.2
2		0.024	0.4
3			0.6
4			0.8
5			0.2
6	CPEG4	0.048	0.4
7			0.6
8			0.8
9			0.2
10		0.072	0.4
11			0.6
12			0.8

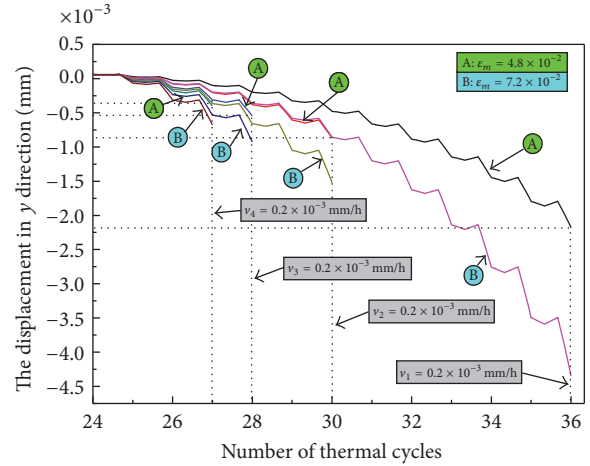


FIGURE 5: The plot of displacement in y direction for node number 517 at the base of the surface groove against the number of thermal cycles when $\epsilon_m = 4.8 \times 10^{-2}$, $\epsilon_m = 7.2 \times 10^{-2}$.

the purpose of studying the influences of MZ growth rate on the displacement instability of TGO.

Figure 4(a) shows the effects of MZ on TGO displacement for the node number 517 in the y direction under various growth rates. In both cases the TGO undergoes the same lateral growth strain ($\epsilon_m = 2.4 \times 10^{-2}$), and it may therefore be concluded that the displacement instability of TGO occurs in two stages. Firstly, displacement gradually changes during the first 24 thermal cycles, with the TGO phase being mainly alumina, in agreement with experimental observations. Secondly, the displacement drops rapidly at the beginning of the 25th thermal cycle, thus caused by MZ formation. It is obvious that the formation of the MZ played a greater role in the displacement instability as compared to the alumina. When the MZ was investigated separately (Figure 4(b)) to

study the effects of MZ growth rate, TGO displacement increased with an increase in MZ growth rate. As MZ thickness remained constant, the cyclic numbers decreased with the increasing MZ growth rate. Therefore, for the FE model, when $v_1 = 0.2 \times 10^{-3}$ mm/h, it had the largest cyclic numbers and the displacement was nearly $0.8 \mu\text{m}$ which was close match with the previous experiments observations [14, 15]. Furthermore, it also had the largest displacement at the end of the thermal cycles, since the lowest MZ growth rate had the longest oxide time, and eventually accumulated the largest displacement. The smallest displacement occurred when the growth rate was $v_4 = 0.8 \times 10^{-3}$ mm/h.

However, it can also be confidently concluded that the larger the MZ growth rate, the larger the change in TGO displacement rate. Indeed, Figure 5 shows that when the

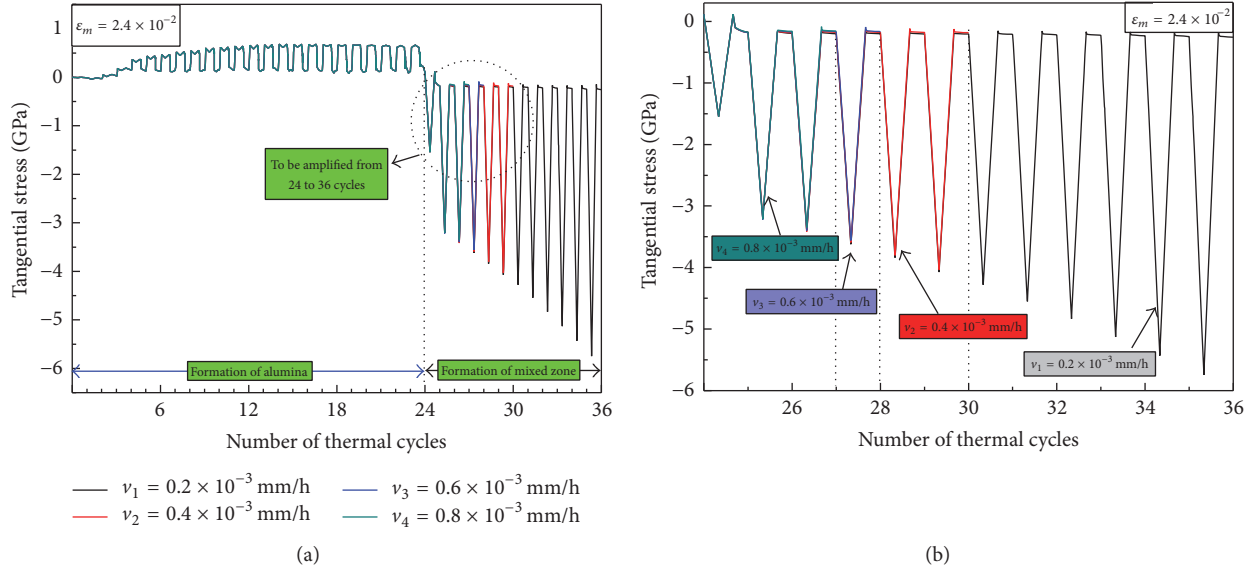


FIGURE 6: (a) The variation of the tangential stress at element number 20857 at the base of the surface groove against the number of thermal cycles when $\epsilon_m = 2.4 \times 10^{-2}$. (b) The details for the variation of tangential stress during the formation of MZ.

lateral growth strain $\epsilon_m = 4.8 \times 10^{-2}$, then $\epsilon_m = 7.2 \times 10^{-2}$. Further, Figure 5 also shows that the displacement fell rapidly when MZ formation began and the max displacement even reaches to more than $4 \mu\text{m}$ which agrees well with the previous works finished by Braue et al. [14, 15]. The rate of displacement increased with increasing MZ growth rate, while the final displacement decreased with increases in the MZ growth rate. Additionally, using the same growth rate but different lateral growth strain values ($\epsilon_m = 4.8 \times 10^{-2}$ and 7.2×10^{-2} , resp.), the larger the lateral growth strain the larger the displacement. Furthermore, when the displacement instabilities were compared (Figures 4(b) and 5), the larger the MZ growth strain, the sharper the change in displacement instability. Above all, an increase in MZ growth rate led to an increase in displacement of TGO. The higher the MZ growth rate, the higher the TGO rate in TGO displacement change but the lower the displacement at the end of the thermal cycles.

Stress plays an important role in the displacement instability of TGO. It is widely accepted that the growth of TGO will induce a huge residual stress in TBCs, which leads to the majority of TBC failures. Additionally, MZ formation can result in a severe change of stress in TGO due to its porous and nonuniform features. In other words, the TGO will suffer from higher tensile or compressive stress due to the presence of MZ. As shown in Figure 6(a), the evolution of tangential stress also followed a two-stage process, with a relatively smooth stage during alumina layer formation and a severe change stage during MZ formation. When considering the effects of MZ on stress evolution in TGO (Figure 6(b)), the largest stress of each thermal cycle is in the range of 0–6 GPa, which is in well agreement with the studies of Karlsson and Evans [7] and Evans et al. [4]. And the higher the growth rate is, the faster the stress reached its maximum value. Conversely, the lower the growth rate is (e.g., $v_1 =$

0.2×10^{-3} mm/h), the slower the stress reached its maximum. However, we could not deny that the stress in TGO reaches to the largest value when $v_1 = 0.2 \times 10^{-3}$ mm/h compared with the last three growth rates. Since MZ thickness remained at a constant value, the increase in MZ growth rate would induce a decrease in oxidation time, allowing for the stress to accumulate and to finally reach its maximum value. Therefore, at constant MZ thickness conditions, the slower the growth rate, the higher the tangential stress. The stress increased with a decrease in MZ growth rate.

With regard to tangential stress (Figure 7 with $\epsilon_m = 2.4 \times 10^{-2}$, 4.8×10^{-2} , and 7.2×10^{-2}), this started to increase rapidly during MZ formation. The faster the growth rate is, the faster the tangential stress reached its maximum value. The stress of each thermal cycle is quite different and the largest stress even reaches to more than 15 GPa which seems not to agree with the works of Karlsson and Evans. The reason is that we adopted an idealized research method to study the instabilities caused by TGO growth. And in order to study the difference caused by the parameters such as lateral growth strain, we set $\epsilon_m = 2.4 \times 10^{-2}$, $\epsilon_m = 4.8 \times 10^{-2}$, and $\epsilon_m = 7.2 \times 10^{-2}$. From Figure 6(b) we know that when $\epsilon_m = 2.4 \times 10^{-2}$ the stress is less than 6 GPa, which fits well with Karlsson's work. In other words, that means the parameters we used are suitable for the research work. Furthermore, the larger the MZ growth strain, the sharper the change in displacement instability. Stress increased with an increase in growth strain, as will be discussed in Section 3.2. Overall, the higher the MZ growth rate, the higher the TGO displacement change rate, and therefore displacement instability increased with increasing MZ growth rate.

3.2. Effects of Mixed Zone Lateral Growth Strain. As shown in Figure 8, we studied the displacement instability induced by the different growth with the same growth rate

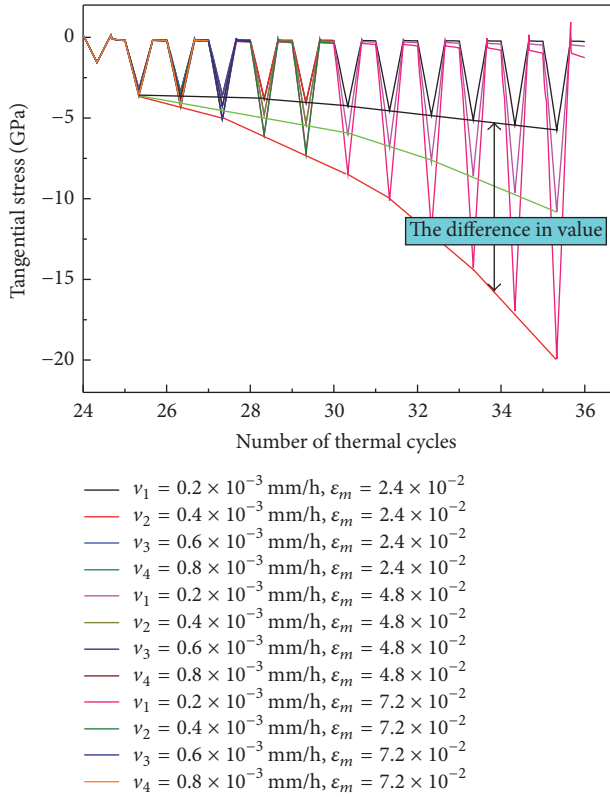


FIGURE 7: The variation of the tangential stress at element number 20857 at the base of the surface groove against the number of thermal cycles when $\epsilon_m = 2.4 \times 10^{-2}$, $\epsilon_m = 4.8 \times 10^{-2}$, and $\epsilon_m = 7.2 \times 10^{-2}$.

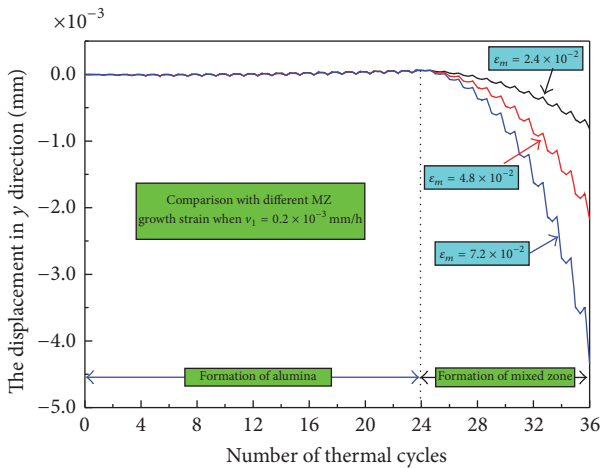


FIGURE 8: The plot of displacement in y direction for node number 517 at the base of the surface groove against the number of thermal cycles when $v_1 = 0.2 \times 10^{-3}$ mm/h.

($v_1 = 0.2 \times 10^{-3}$ mm/h). The same two-stage process applies herein, with a slow change during the first 24 thermal cycles followed by a sharp change from the beginning of the 25th thermal cycle until the end, at which stage MZ growth began. The larger the growth strain is, the faster the displacement changed, and the larger the final displacement

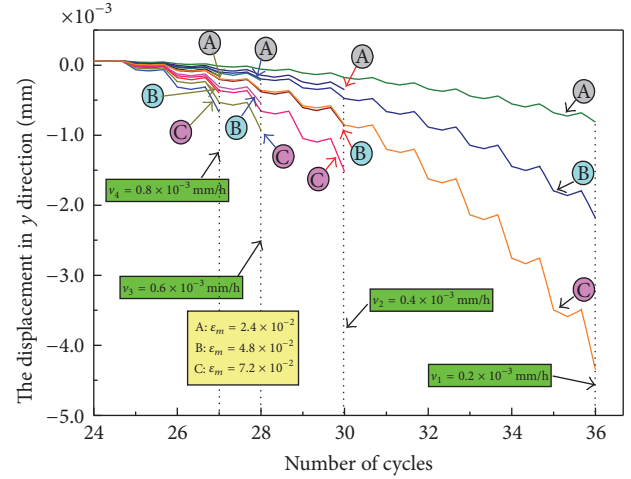


FIGURE 9: The plot of displacement in y direction for node number 517 at the base of the surface groove against the number of thermal cycles with all conditions of MZ growth strain.

is. Therefore, the MZ had a greater effect on displacement instability compared to the alumina layer. Furthermore, when comparing displacement instability (Figure 9) with the MZ growth rates were $v_1 = 0.2 \times 10^{-3}$ mm/h, $v_2 = 0.4 \times 10^{-3}$ mm/h, $v_3 = 0.6 \times 10^{-3}$ mm/h, and $v_4 = 0.8 \times 10^{-3}$ mm/h, respectively. In general, the higher the growth strain, the faster the change in displacement and, finally, the larger the displacement.

Stress exhibited a rapid change during MZ formation (Figure 10(a)). Furthermore, the larger the growth strain, the larger the tangential stress. Additionally, the MZ layer had a significant influence on the evolution of stress compared to the alumina layer. In order to assess the difference between the different growth strains, we separately assessed the last 12 thermal cycles during which MZ conversion began (Figure 10(b)). The results showed that the largest stress also reaches to more than 15 GPa, which is the same reason as the explanation given for Figure 7. The larger the lateral growth strain, the higher the tangential stress for each thermal cycle, and a maximum tangential stress is reached at the end of the thermal cycle. This effect was also observed at $v_2 = 0.4 \times 10^{-3}$, 0.6×10^{-3} , and 0.8×10^{-3} mm/h (Figure 11), showing that the tangential stress increases significantly during MZ formation. Furthermore, the larger the growth strain, the larger the tangential stress under the same growth rate.

3.3. *Effects of Mixed Zone Thickness.* The stress and displacement instability induced by the thickness of MZ in TGO were analyzed. From the results in Sections 3.1 and 3.2, the displacement instability would increase with the increase in TGO thickness. However, the thickening of the alumina layer did not induce a considerable increase in stress compared with the MZ layer. In other words, the MZ thickness had a significant influence on the displacement instability compared to that of alumina (Figure 12). The total MZ thickness was $2 \mu\text{m}$. The displacement changed slowly during alumina layer thickening, but when the MZ thickness increased from 0 to $2 \mu\text{m}$, as shown in Figure 12,

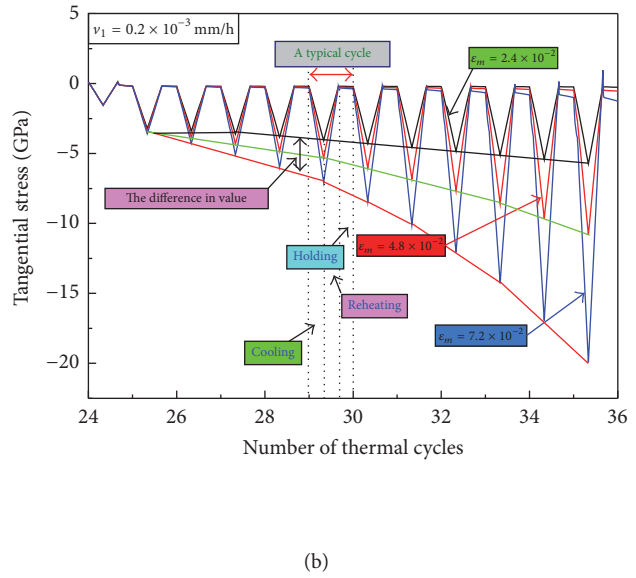
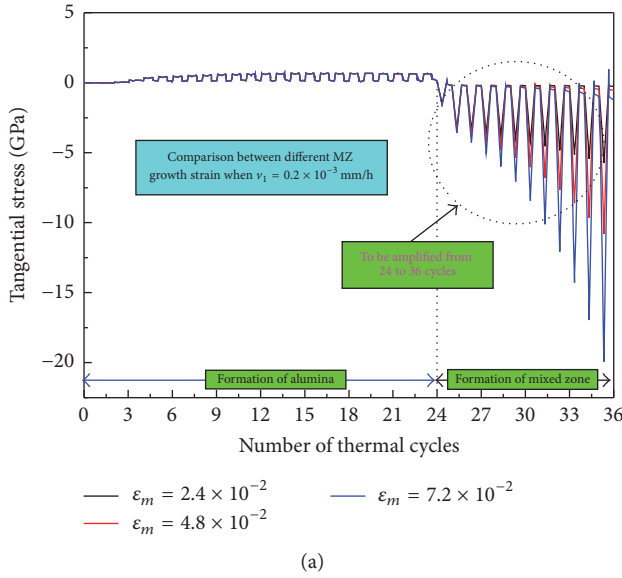


FIGURE 10: (a) The variation of the tangential stress at element number 20857 at the base of the surface groove against the number of thermal cycles when $v_1 = 0.2 \times 10^{-3}$ mm/h. (b) The details for the variation of tangential stress for the first two thermal cycles.

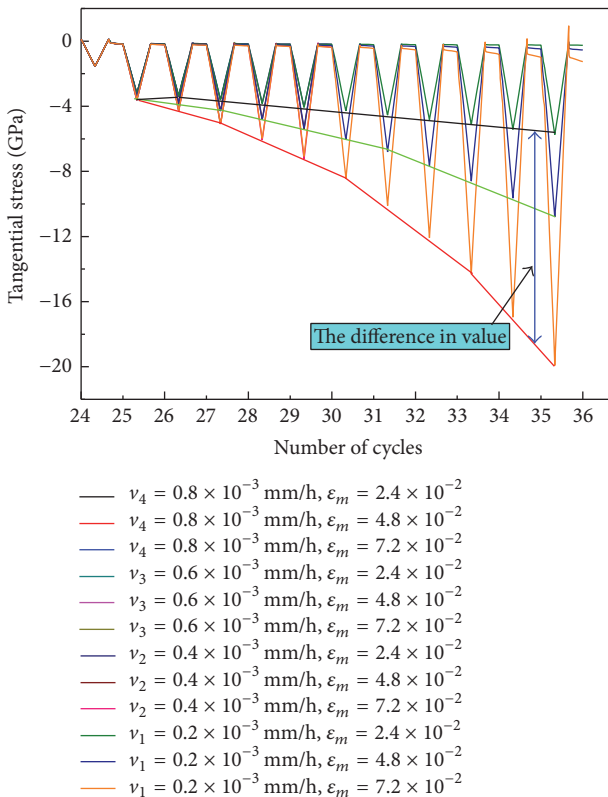


FIGURE 11: The variation of the tangential stress at element number 20857 at the base of the surface groove against the number of thermal cycles for all conditions of MZ growth rate.

the displacement began to change rapidly. When the MZ thickness was increased further, the trend in increasing displacement was almost linear. Therefore, the thicker the MZ layer, the larger the displacement instability. Furthermore,

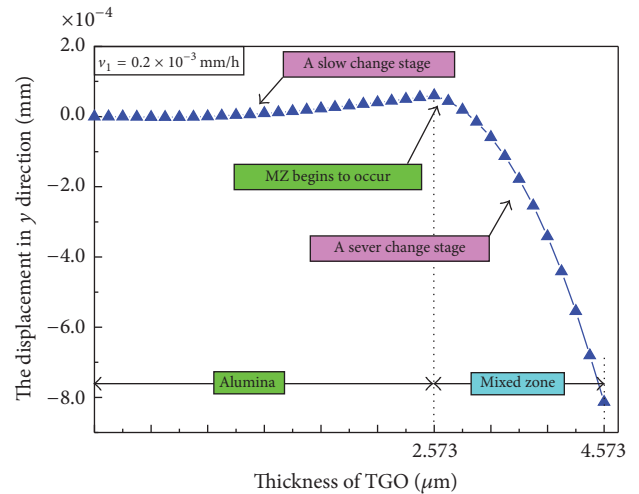


FIGURE 12: The plot of displacement in y direction for node number 517 at the base of the surface groove against the number of thermal cycles.

this trend was observed when the growth rates were $v_2 = 0.4 \times 10^{-3}$ mm/h, $v_3 = 0.6 \times 10^{-3}$ mm/h, and $v_4 = 0.8 \times 10^{-3}$ mm/h (data not shown).

It is generally accepted that the thickening of TGO will lead to large stresses; this can be observed in Figure 13. The stress increased with the increase in TGO thickness. However, during MZ formation, the stress seemed to accelerate increasing. Stress also followed the two-stage process, with a slowly changing stage caused by the formation of the alumina layer, at which stage there was no MZ layer, followed by a sharply changing stage induced by MZ formation. The effects of MZ thickness on stress evolution were more significant than those of the alumina layer thickness. Indeed, the stress increased with increasing MZ thickness. Furthermore, this

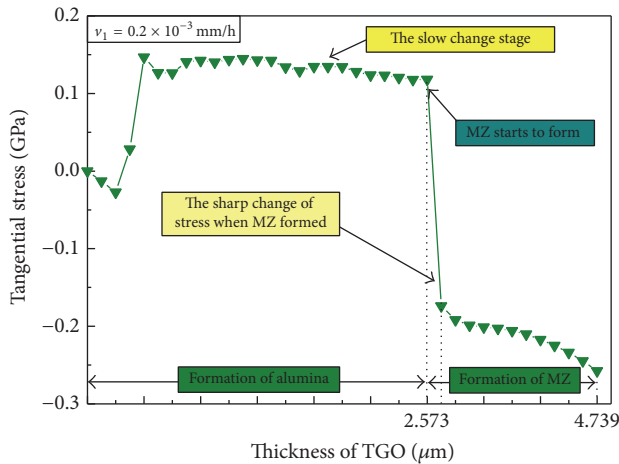


FIGURE 13: Variation of tangential stress at element number 20857 at the base of the surface groove against the number of thermal cycles when $v_1 = 0.2 \times 10^{-3}$ mm/h.

can also be observed in the other three conditions, when the growth rates were $v_2 = 0.4 \times 10^{-3}$ mm/h, $v_3 = 0.6 \times 10^{-3}$ mm/h, and $v_4 = 0.8 \times 10^{-3}$ mm/h (data not shown).

4. Conclusions

The effects of MZ on the displacement instability of TGO were assessed in this paper. The results show that the formation of MZ exerts a significant influence on displacement instability and stress in TGO, leading to an acceleration of TBC failure, which agrees well with the previous works [14, 15]. Based on the simulation results presented in this work, the following conclusions can be drawn:

- (1) The MZ growth rate induces a rapid change of displacement instability and stress in TGO. The displacement instability and stress in TGO increase with the increase in MZ growth rate. The higher the growth rate, the larger the displacement instability and stress.
- (2) The growth strain of MZ can result in fast change of displacement instability and stress change in TGO. The increase of MZ growth strain will result in an increase of displacement instability and a huge increasing of stress in TGO. The higher the growth strain is, the higher the displacement instability is and the higher the stress in TGO is.
- (3) The thickening of MZ will also lead to a sharp increase in TGO displacement instability and stress. The thicker the MZ layer, the larger the TGO displacement instability and stress.

Nomenclature

TBC: Thermal barrier coating
 TGO: Thermally grown oxide
 MZ: Mixed zone
 BC: Bond coat

E : Young's modulus
 ν : Poisson ratio
 ε_t : TGO normal growth strain
 ε_g : TGO lateral growth strain
 ε_{Al} : Alumina lateral growth strain
 ε_m : MZ lateral growth strain.

Competing Interests

The authors declare no conflict of interests.

Acknowledgments

This work is financially supported by the Natural Science Foundation of China (11302272) and by NSAF (Grant no. U1530140).

References

- [1] S. Grape, S. Jacobsson Svård, C. Hellesen, P. Jansson, and M. Åberg Lindell, "New perspectives on nuclear power-generation IV nuclear energy systems to strengthen nuclear non-proliferation and support nuclear disarmament," *Energy Policy*, vol. 73, pp. 815–819, 2014.
- [2] A Technology Roadmap for Generation IV Nuclear Energy Systems, US DOE Nuclear Energy Research Advisory Committee and the Generation IV International Forum.
- [3] L. Wang, D. C. Li, J. S. Yang et al., "Modeling of thermal properties and failure of thermal barrier coatings with the use of finite element methods: a review," *Journal of the European Ceramic Society*, vol. 36, no. 6, pp. 1313–1331, 2016.
- [4] A. G. Evans, D. R. Mumm, J. W. Hutchinson, G. H. Meier, and F. S. Pettit, "Mechanisms controlling the durability of thermal barrier coatings," *Progress in Materials Science*, vol. 46, no. 5, pp. 505–553, 2001.
- [5] S.-W. Myoung, S.-S. Lee, H.-S. Kim et al., "Effect of post heat treatment on thermal durability of thermal barrier coatings in thermal fatigue tests," *Surface & Coatings Technology*, vol. 215, pp. 46–51, 2013.
- [6] V. Kumar and K. Balasubramanian, "Progress update on failure mechanisms of advanced thermal barrier coatings: a review," *Progress in Organic Coatings*, vol. 90, pp. 54–82, 2016.
- [7] A. M. Karlsson and A. G. Evans, "A numerical model for the cyclic instability of thermally grown oxides in thermal barrier systems," *Acta Materialia*, vol. 49, no. 10, pp. 1793–1804, 2001.
- [8] C. H. Hsueh and E. R. Fuller, "Analytical modeling of oxide thickness effects on residual stresses in thermal barrier coatings," *Scripta Materialia*, vol. 42, no. 8, pp. 781–787, 2000.
- [9] J. Ding, F.-X. Li, and K.-J. Kang, "Effects of material creep on displacement instability in a surface groove under thermo-mechanical cycling," *Surface and Coatings Technology*, vol. 204, no. 1-2, pp. 157–164, 2009.
- [10] Y. Z. Liu, S. J. Zheng, Y. L. Zhu, H. Wei, and X. L. Ma, "Microstructural evolution at interfaces of thermal barrier coatings during isothermal oxidation," *Journal of the European Ceramic Society*, vol. 36, no. 7, pp. 1765–1774, 2016.
- [11] M. T. Hernandez, A. M. Karlsson, and M. Bartsch, "On TGO creep and the initiation of a class of fatigue cracks in thermal barrier coatings," *Surface and Coatings Technology*, vol. 203, no. 23, pp. 3549–3558, 2009.

- [12] B. Lv, H. Xie, R. Xu, X. Fan, W. Zhang, and T. J. Wang, "Effects of sintering and mixed oxide growth on the interface cracking of air-plasma-sprayed thermal barrier coating system at high temperature," *Applied Surface Science*, vol. 360, pp. 461–469, 2016.
- [13] R. Xu, X. L. Fan, W. X. Zhang, and T. J. Wang, "Interfacial fracture mechanism associated with mixed oxides growth in thermal barrier coating system," *Surface and Coatings Technology*, vol. 253, pp. 139–147, 2014.
- [14] W. Braue, P. Mechnich, K. Fritscher, and L. Niewolak, "Compatibility of mixed zone constituents (YAG, YAP, YCrO_3) with a chromia-enriched TGO phase during the late stage of TBC lifetime," *Surface and Coatings Technology*, vol. 202, no. 4–7, pp. 670–675, 2007.
- [15] W. Braue, U. Schulz, K. Fritscher, C. Leyens, and R. Wirth, "Analytical electron microscopy of the mixed zone in NiCoCrAlY-based EB-PVD thermal barrier coatings: as-coated condition versus late stages of TBC lifetime," *Materials at High Temperatures*, vol. 22, no. 3–4, pp. 393–401, 2005.
- [16] Y. Li, C.-J. Li, Q. Zhang, G.-J. Yang, and C.-X. Li, "Influence of TGO composition on the thermal shock lifetime of thermal barrier coatings with cold-sprayed MCrAlY bond coat," *Journal of Thermal Spray Technology*, vol. 19, no. 1–2, pp. 168–177, 2010.
- [17] Y. Bai, C. Ding, H. Li et al., "Isothermal oxidation behavior of supersonic atmospheric plasma-sprayed thermal barrier coating system," *Journal of Thermal Spray Technology*, vol. 22, no. 7, pp. 1201–1209, 2013.
- [18] R. D. Maier, C. M. Scheuermann, and C. W. Andrews, "Degradation of a two-layer thermal barrier coating under thermal cycling," *American Ceramic Society Bulletin Journal*, vol. 60, pp. 555–560, 1981.

Research Article

Nondestructive Evaluation of Functionally Graded Subsurface Damage on Cylinders in Nuclear Installations Based on Circumferential SH Waves

Zhen Qu,^{1,2} Xiaoqin Shen,² and Xiaoshan Cao^{1,3}

¹*School of Civil Engineering and Architecture, Xi'an University of Technology, Xi'an 710048, China*

²*School of Sciences, Xi'an University of Technology, Xi'an 710054, China*

³*State Key Laboratory of Transducer Technology, Chinese Academy of Sciences, Shanghai 200050, China*

Correspondence should be addressed to Xiaoqin Shen; xqshen@xaut.edu.cn

Received 30 June 2016; Accepted 7 September 2016

Academic Editor: Xing Chen

Copyright © 2016 Zhen Qu et al. This is an open access article distributed under the Creative Commons Attribution License, which permits unrestricted use, distribution, and reproduction in any medium, provided the original work is properly cited.

Subsurface damage could affect the service life of structures. In nuclear engineering, nondestructive evaluation and detection of the evaluation of the subsurface damage region are of great importance to ensure the safety of nuclear installations. In this paper, we propose the use of circumferential horizontal shear (SH) waves to detect mechanical properties of subsurface regions of damage on cylindrical structures. The regions of surface damage are considered to be functionally graded material (FGM) and the cylinder is considered to be a layered structure. The Bessel functions and the power series technique are employed to solve the governing equations. By analyzing the SH waves in the 12Cr-ODS ferritic steel cylinder, which is frequently applied in the nuclear installations, we discuss the relationship between the phase velocities of SH waves in the cylinder with subsurface layers of damage and the mechanical properties of the subsurface damaged regions. The results show that the subsurface damage could lead to decrease of the SH waves' phase velocity. The gradient parameters, which represent the degree of subsurface damage, can be evaluated by the variation of the SH waves' phase velocity. Research results of this study can provide theoretical guidance in nondestructive evaluation for use in the analysis of the reliability and durability of nuclear installations.

1. Introduction

In many engineering fields, such as the nuclear and aerospace industries, nondestructive evaluation of damage is important for enhancing the lifetime and ensuring the reliability of devices, and this is especially pertinent for nuclear equipment. Generally speaking, the corrosive environments, fatigue under periodic mechanical or thermal loading during operations, and nuclear radiation exposure might lead to the material's subsurface damage [1–6]. Acoustic waves are typically good tools for detecting the properties of subsurface damaged regions in structures [7]. The influence of subsurface damage on surface waves should also be investigated.

Paehler et al. [8] found that the elastic coefficient in the subsurface regions of silicon wafers with subsurface damage is a variable dependent upon depth based on the Rayleigh waves dispersion relation obtained experimentally. However,

in that experiment, the subsurface region was corroded step by step. Therefore, despite the use of acoustic waves by the researchers, that technique is not a truly nondestructive evaluation. Cao et al. [9] proposed that regions of subsurface damage should be treated as functionally graded material (FGM) layers of the material. Then guide waves in the FGM model could be applied to detect subsurface damage in structures.

Some researchers have attempted to simplify the problem by theoretically assuming that FGM material with multilayered structures has homogeneous but discontinuous properties. Daros [10] used the boundary element method to explain SH wave propagation in inhomogeneous media. Potel et al. [11] described SH waves along two isotropic solid plates with integral formulation.

In other articles, many researchers use the special functions method or transfer matrix method to describe the

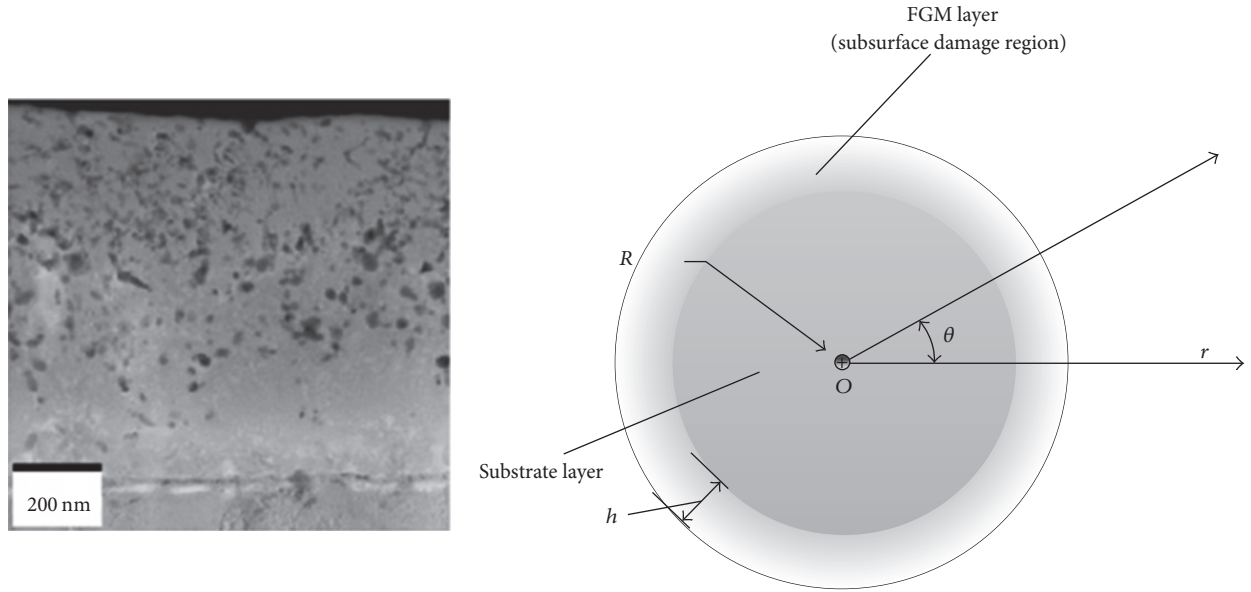


FIGURE 1: Structure of the cylinder with surface damage (see [23]).

problem of SH wave propagation in the layered structure [12–15]. Some reports have been published on the analysis of the propagation properties of Love waves in FGM layered structures with the Wentzel-Kramers-Brillouin (WKB) method [16–18]. The analytic solutions with the special functions method to describe the Love wave, B-G wave, and horizontal shear waves in FGM structures have been reported by other researchers. In these reports, the WKB and special functions methods can only be used at high frequencies and are only good in certain cases. The power series technique has been used by Cao et al. [19] to resolve the difficulty of the variable coefficient differential equation and fit for general cases. There is a substantial body of research concerning wave propagation in FGM or layered structures focusing on half-space or layered films, but studies which focused on cylindrical structures are less common. Zhu et al. [20] used the reverberation-ray matrix formulation for cylindrical coordinates to discuss the ways in which material inhomogeneity primarily affects wave propagation for high modes. Legendre polynomial series method was used by Yu et al. [21] to solve coupled wave equations with variable coefficients.

Most studies on subsurface damage are focused on flat structures, but the curvature of the structure also influences wave propagation [22]. In our study, we consider the propagation of the circumferential SH wave in cylindrical structures with surface damage and analyze the surface damage layer as an FGM layer. In this layer, the material properties are a function of the cylinder thickness. In the FGM layer, the power series technique is used to solve the governing equations as a variable coefficient differential with cylindrical coordinates. In the rest of the cylinder, the special functions method is applied. Based on a numerical example, we discuss the dispersion relation of the circumferential SH wave and the influence of gradient parameters on SH wave propagation.

2. Statement of the Problem

As shown in Figure 1, the surface damage layer is an FGM layer with thickness h , while R is the thickness of substrate layer. This is based upon the assumption that SH surface waves propagate along the circumferential direction, and the surface stress is free. Considering that the thickness of the substrate is greater than that of the FGM layer, it is assumed that the substrate is a half-space. According to generalized Hooke's law, the constitutive equations can be expressed as follows:

$$\sigma_{ij} = c_{ijkl}\varepsilon_{kl}, \quad (1)$$

where σ_{ij} and ε_{kl} are the stress and strain tensors and c_{ijkl} is the elastic coefficient. In the FGM layer, c_{ijkl} are a function of layer thickness, and in the substrate c_{ijkl} are constants.

The motion equation is then given as follows:

$$\sigma_{ij,j} = \rho\ddot{u}_i, \quad (2)$$

where ρ is the material density, the subscript i denotes the i th direction in the corresponding coordinates, u_i is the displacement of i th direction, the dot (\cdot) denotes the differential of time, and j preceded by a comma means that there is space differentiation of the relevant coordinate x_j . In this paper, we choose the cylindrical coordinates, so i or j can be denoted by r , θ , and z .

The displacement and the strain tensors are expressed as follows:

$$\varepsilon_{ij} = \frac{1}{2}(u_{i,j} + u_{j,i}). \quad (3)$$

For the SH surface waves propagating along the circumferential direction, let the displacement component be described

as $u_r = u$, $u_\theta = v$, and $u_z = w$, and u , v , and w can be expressed as

$$\begin{aligned} u &= v = 0, \\ w &= w(r, \theta, t). \end{aligned} \quad (4)$$

Equation (1) can be simplified as

$$\begin{aligned} \tau_{rz} &= c_{44}\varepsilon_{rz}, \\ \tau_{\theta z} &= c_{44}\varepsilon_{\theta z}. \end{aligned} \quad (5)$$

Using (2), (3), (4), and (5), we can induce the governing equation of displacement for corresponding material layers.

In the substrate layer, $w^{(1)}$ is defined as the mechanical displacement component. The governing equation for SH waves in the substrate layer $r \in (0, R]$ can be obtained:

$$c_{440} \frac{\partial^2 w^{(1)}}{\partial r^2} + c_{440} \frac{1}{r} \frac{\partial w^{(1)}}{\partial r} + \frac{1}{r^2} \frac{\partial^2 w^{(1)}}{\partial \theta^2} = \rho \frac{\partial^2 w^{(1)}}{\partial t^2}, \quad (6)$$

where c_{440} is the constant material elastic coefficient and ρ is the material density of the substrate layer.

In the FGM layer, we can define the mechanical displacement component as $w^{(2)}$. Therefore, the governing equation for SH waves in the FGM layer can be described as $r \in [R, R+h]$. Consider

$$\begin{aligned} c_{44}(r) \frac{\partial^2 w^{(2)}}{\partial r^2} + c'_{44}(r) \frac{\partial w^{(2)}}{\partial r} + c_{44}(r) \frac{1}{r} \frac{\partial w^{(2)}}{\partial r} \\ + \frac{1}{r^2} \frac{\partial^2 w^{(2)}}{\partial \theta^2} = \rho(r) \frac{\partial^2 w^{(2)}}{\partial t^2}. \end{aligned} \quad (7)$$

Because the material parameters are functions of layer thickness in the FGM layer, $c_{44}(r)$ is used to denote the function of elastic coefficients, $\rho(r)$ is the function of material density, and $c'_{44}(r)$ is the differentiation with coordinate r .

Additionally, for the problem of SH waves propagating in the cylindrical structure with subsurface damage, the following boundary conditions and continuity conditions should be satisfied:

- (1) Traction-free boundary conditions at $r = R+h$:

$$\tau_{rz}^{(2)}(R+h, \theta) = 0. \quad (8)$$

- (2) The continuity conditions at $r = R$:

$$\begin{aligned} w^{(1)}(R, \theta, t) &= w^{(2)}(R, \theta, t), \\ \tau_{rz}^{(1)}(R, \theta, t) &= \tau_{rz}^{(2)}(R, \theta, t). \end{aligned} \quad (9)$$

The superscripts “(1) and (2)” in the above-mentioned boundary conditions and continuity conditions denote the mechanical quantities in the substrate layer and the FGM layer, respectively.

3. Solution to the Problem

For the mentioned SH waves in the substrate layer of the cylinder, the solution to the governing equations can be assumed in the following form:

$$w^{(1)}(r, \theta, t) = W^{(1)}(r) \exp[i(kh\theta + kR\theta - \omega t)], \quad (10)$$

where $i = \sqrt{-1}$, $\omega = kc$ is the circular frequency, and k , c , and $W^{(1)}(r)$ are the wave number, the phase velocity, and the unknown amplitudes function of the displacement, respectively.

Substituting (10) into (6), we obtain Bessel's equation of order l as follows:

$$\frac{d^2 W^{(1)}}{dr^2} + \frac{1}{r} \frac{dW^{(1)}}{dr} + \left(u - \frac{l^2}{r^2}\right) W^{(1)} = 0, \quad (11)$$

where $u = \rho^{(1)}\omega^2/c_{440}$ and $l = kR + kh$. By using the special functions method, the solution of the equation can be expressed as follows:

$$W^{(1)} = C_1 J_l(ur) + C_2 Y_l(ur), \quad (12)$$

where C_1 and C_2 are the undetermined constants and $J_l(x)$ and $Y_l(x)$ are first-class and second-class Bessel's functions with order l . When $r \rightarrow 0$, $W^{(1)}(r)$ must have a finite value, so $C_2 = 0$ can be deduced. Therefore, (12) can be simplified as

$$W^{(1)} = C_1 J_l(ur). \quad (13)$$

Similarly, we can arrive at the solution of the governing equations in the FGM layer with the following formula:

$$w^{(2)}(r, \theta, t) = W^{(2)}(r) \exp[i(kR\theta + kh\theta - \omega t)], \quad (14)$$

where $W^{(2)}(r)$ is the unknown amplitudes function of the displacement. Substituting (14) into (7), we obtain

$$\begin{aligned} c_{44}(r) \frac{d^2 W}{dr^2} + c'_{44}(r) \frac{dW}{dr} + \frac{1}{r} c_{44}(r) \frac{dW}{dr} \\ - \frac{l^2}{r^2} c_{44}(r) W + \rho \omega^2 W = 0. \end{aligned} \quad (15)$$

By letting $\hat{r} = (r - R)/h$, (15) can be rewritten as an ordinary differential equation with respect to \hat{r} :

$$\begin{aligned} \left(\hat{r} + \frac{R}{h}\right)^2 c_{44}(\hat{r}) \frac{d^2 W}{d\hat{r}^2} + \left(\hat{r} + \frac{R}{h}\right)^2 \frac{dc_{44}(\hat{r})}{d\hat{r}} \\ + \left(\hat{r} + \frac{R}{h}\right) c_{44}(\hat{r}) \frac{dW}{d\hat{r}} - l^2 c_{44}(\hat{r}^2) W \\ + (h\hat{r} + R)^2 \rho(\hat{r}^2) \omega^2 W = 0. \end{aligned} \quad (16)$$

To solve this ordinary differential equation with the variable coefficient, we assume that the material parameters

functions can be expanded as the power series with respect to \hat{r}^n by using the power series technique as follows:

$$\begin{aligned} c_{44}(\hat{r}) &= \sum_{n=0}^{\infty} m_n^1 \hat{r}^n, \\ \rho(\hat{r}) &= \sum_{n=0}^{\infty} m_n^2 \hat{r}^n. \end{aligned} \quad (17)$$

Hence, with the material parameters subjected to the power series technique, the amplitude function should have the same form as

$$W^{(2)}(\hat{r}) = \sum_{n=0}^{\infty} a_n \hat{r}^n, \quad (18)$$

where $m_n^k = (1/n!)(d^n f_k / dr^n)$, $k = 1, 2$, and a_n are the coefficients of the power series. f_k is the function which describes the variation of material parameters with layer thickness, and m_n^k can be determined by the relationships between the function and its Taylor expansion. Substituting (17) and (18) into (16), we get the following equation:

$$\begin{aligned} &\left(\hat{r} + \frac{R}{h}\right)^2 \left(\sum_{n=0}^{\infty} m_n^1 \hat{r}^n\right) \left(\sum_{n=0}^{\infty} n(n-1) a_n \hat{r}^{n-2}\right) \\ &+ \left(\hat{r} + \frac{R}{h}\right)^2 \left(\sum_{n=0}^{\infty} n m_n^1 \hat{r}^{n-1}\right) \left(\sum_{n=0}^{\infty} n a_n \hat{r}^{n-1}\right) \\ &+ \left(\hat{r} + \frac{R}{h}\right) \left(\sum_{n=0}^{\infty} m_n^1 \hat{r}^n\right) \left(\sum_{n=0}^{\infty} n a_n \hat{r}^{n-1}\right) \\ &- l^2 \left(\sum_{n=0}^{\infty} m_n^1 \hat{r}^n\right) \left(\sum_{n=0}^{\infty} a_n \hat{r}^n\right) \\ &+ (h\hat{r} + R)^2 \omega^2 \left(\sum_{n=0}^{\infty} m_n^2 \hat{r}^n\right) \left(\sum_{n=0}^{\infty} a_n \hat{r}^n\right) = 0; \end{aligned} \quad (19)$$

the coefficients of \hat{r}^n on the two sides of (19) must equal each other. Therefore, the relation of a_n can be obtained:

$$\begin{aligned} &\sum_{j=0}^n [n(n-j) - l^2] m_j^1 a_{n-j} + \left(\frac{R}{h}\right) \\ &\cdot \sum_{j=0}^n [(n-j+1)(2n+1)] m_j^1 a_{n-j+1} + \left(\frac{R}{h}\right)^2 \\ &\cdot \sum_{j=0}^n [(n-j+2)(n+1)] m_j^1 a_{n-j+2} \\ &+ \sum_{j=0}^n (h^2 \omega^2 m_j^2 a_{n-j-2} + 2hR\omega^2 m_j^2 a_{n-j-1} \\ &+ R^2 \omega^2 m_j^2 a_{n-j}) = 0. \end{aligned} \quad (20)$$

Let $a_{-2} = a_{-1} = 0$; when $n \geq 2$, (15) is a recurrence equation of a_n and can be solved through a specific value of a_0, a_1 . Then the amplitudes function is redescribed as

$$W^{(2)}(\hat{r}) = \sum_{j=2}^3 C_j \left(\sum_{n=0}^{\infty} a_{nj} \hat{r}^n \right), \quad (21)$$

where $(a_{0j}, a_{1j}) = I$ and I is a 2×2 unit matrix. Then, substituting (13) and (21) into the boundary and continuity conditions, the linear equation with C_i , $i = 1, 2, 3$, can be obtained, and this equation must have a nontrivial solution. From the sufficient and necessary condition of homogeneous linear equation, we know that the determinant of the coefficient matrix is equal to zero, which expresses the dispersion relation for SH waves.

$$|T_{ij}| = 0, \quad (22)$$

where T_{ij} , $i, j = 1, 2, 3$, can be written as follows:

$$\begin{aligned} T_{11} &= 0, \\ T_{1j} &= \frac{1}{h} c_{44} (R+h) \left(\sum_{n=0}^{\infty} n a_{nj} \right), \quad j = 2, 3, \\ T_{21} &= J_l(uR), \\ T_{22} &= -a_{02}, \\ T_{23} &= -a_{03}, \\ T_{31} &= c_{44}^{(1)} J_l'(uR), \\ T_{3j} &= -c_{44} (R) a_{1j}, \quad j = 2, 3. \end{aligned} \quad (23)$$

4. Numerical Examples

Next, the numerical examples are given to study the propagation behavior of SH waves in cylindrical structures and to graphically show the dispersion relation. Suppose that the cylinder with surface damage is a composite of an FGM layer and a homogeneous substrate with the same material. This is a simplified model of the nuclear detector equipment used in nuclear engineering. In the substrate layer, the material parameters c_{440} and ρ are constant, and in the FGM layer these parameters become functions with the layer thickness. Therefore, in order to describe the surface damage, we describe the two types of the gradient functions as follows:

Type A:

$$f(\hat{r}) = \exp(-p\hat{r}), \quad (24)$$

Type B:

$$f(\hat{r}) = 1 - p\hat{r}, \quad (25)$$

where p is the gradient parameter. Then the parameter functions with thickness can be denoted as

$$c_{44}(\hat{r}) = c_{440} f(\hat{r}). \quad (26)$$

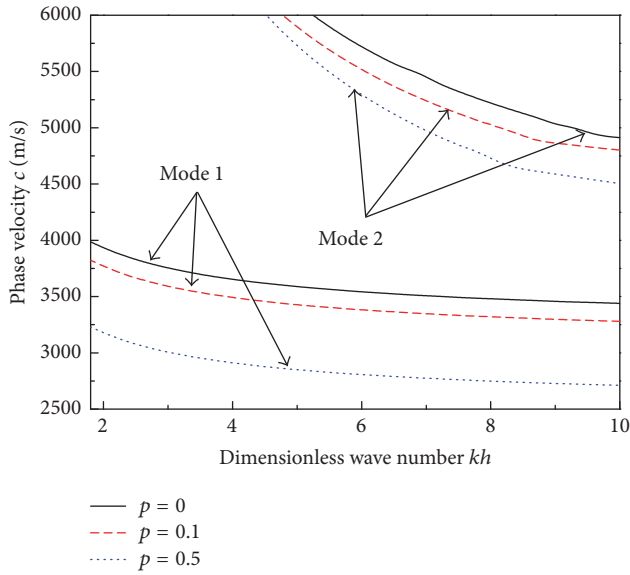


FIGURE 2: Comparing the dispersion relation of the SH waves with the different gradient parameter p for Type A.

Within the equipment of nuclear applications, $^{12}\text{Cr-ODS}$ has great applicability because of its good mechanical properties under irradiation and high temperatures [1]. In this paper, $^{12}\text{Cr-ODS}$ ferritic steel is selected as the cylinder's material and its material parameters are given as $c_{440} = 80 \text{ GPa}$ and $\rho = 7.85 \times 10^3 \text{ kg/m}^3$. The thickness of the FGM layer and substrate is $h = 0.003 \text{ m}$, and the radius of the cylinder is $R = 1 \text{ m}$. Generally, subsurface damage has great influence on the material's mechanic parameters, so we assume that $c_{44}(\hat{r})$ is a function with the layer thickness and the density ρ is constant in the FGM layer. Next the dispersion relation of the SH waves in the cylindrical structure with surface damage is discussed.

Figure 2 shows the dispersion curves of the SH wave that propagates in the cylinder with different gradient parameter p ; $p = 0$ indicates that the material is homogeneous without surface damage and describes the different modes of the wave propagation when the mechanical parameters function as Type A in the surface damage layer. Obviously, with the increase in the gradient parameter p , the phase velocity of the wave is decreased. Figure 3 shows how the mechanical parameters function as Type B influencing the surface damage. The change tendency of the phase velocity is similar to that seen in Figure 2. For both of these types of surface damage, the gradient parameter influences the dispersion relation of the SH wave to a greater extent in mode 2. For every gradient parameter, with the increase of wave number k , the phase velocity is decreased.

We also have investigated the influence of the gradient parameter on the phase velocity. For given kh , such as $kh = 2\pi$, the relationship between the gradient parameter p and the absolute value of the increment of phase velocity $|\Delta c|$ has been discussed, where $|\Delta c| = \bar{c} - c$, \bar{c} is the phase velocity in cylinder without subsurface damage, and c is the phase velocity in

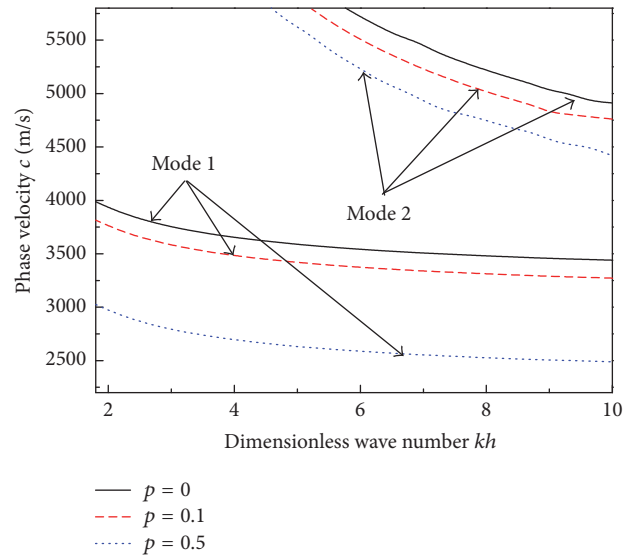


FIGURE 3: Comparing the dispersion relation of the SH waves with the different gradient parameter p for Type B.

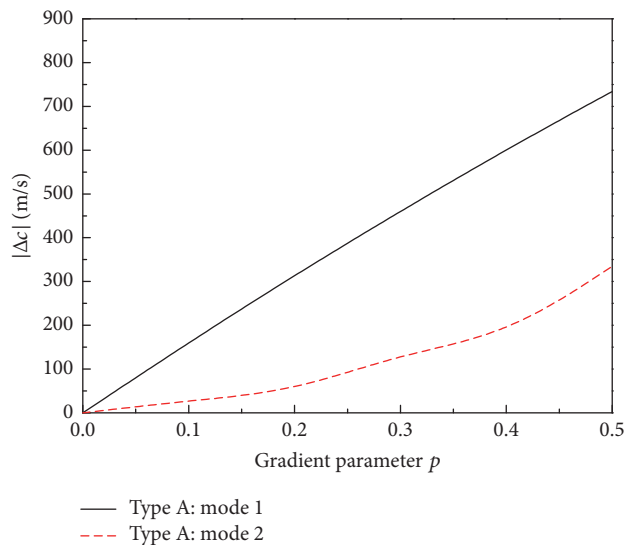


FIGURE 4: The influence of gradient parameter on the increment of phase velocity with subsurface damage Type A.

different gradient parameter. As shown in Figures 4 and 5, with the increase of gradient parameter p , $|\Delta c|$ is increased for both subsurface damage Type A and subsurface damage Type B. It means that the larger gradient parameter could cause the significant change tendency of phase velocity of SH wave. In Type A, the changing in the phase velocity is more stable and notable in mode 1 than in mode 2. In Type B, although the changing tendency of the phase velocity holds steady in mode 1, the increasing of $|\Delta c|$ is more obvious in mode 2. These results indicate that it is possible to detect subsurface damage on cylindrical structure through the change of the phase velocity in specific circumstances. Therefore, these properties of SH waves can be applied for nondestructive evaluation of subsurface damage on nuclear installations.

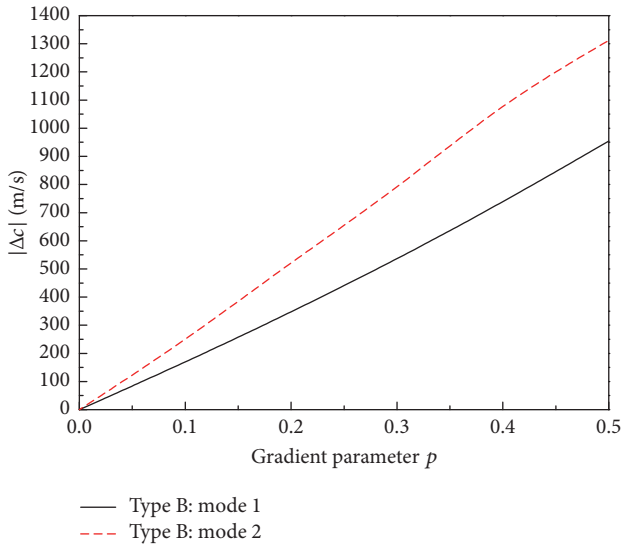


FIGURE 5: The influence of gradient parameter on the increment of phase velocity with subsurface damage Type B.

5. Conclusions

Using the series technique, the circumferential SH waves in cylinders with surface damage were analyzed. The results showed that the gradient parameters affect the propagation of the waves, and the rate of change of the phase velocity is more stable in mode 1 than in mode 2. With the change in the subsurface damage type, the propagation of SH waves is significantly different. We found that it is possible to check the equipment for surface damage using the change value of the phase velocity of SH waves, and this provides us with a method for identifying the type of damage we encountered. These results could also be used as theoretical guidance in the nondestructive evaluation of the reliability and durability of nuclear installations.

Competing Interests

The authors declare that they have no competing interests.

Acknowledgments

The authors gratefully acknowledge the support by the National Natural Science Foundation of China (nos. 11572244, 11571275, and U1630144), the Natural Science Foundation of Shaanxi Province (nos. 2015JQ1001 and 2015GY021), and the Open State Key Laboratories of Transducer Technology (no. SKT1506).

References

- [1] Z. B. Yang, B. F. Hu, H. Kinoshita, H. Takahashi, and S. Watanabe, "Effect of hydrogen ion/electron dual-beam irradiation on micro structural damage of a 12Cr-ODS ferrite steel," *Journal of Nuclear Materials*, vol. 398, no. 1–3, pp. 81–86, 2010.
- [2] M. A. Rana, "Swelling and structure of radiation induced near-surface damage in CR-39 and its chemical etching," *Radiation Measurements*, vol. 47, no. 1, pp. 50–56, 2012.
- [3] H. Sako, H. Matsuhata, M. Sasaki et al., "Micro-structural analysis of local damage introduced in subsurface regions of 4H-SiC wafers during chemo-mechanical polishing," *Journal of Applied Physics*, vol. 119, no. 13, Article ID 135702, 2016.
- [4] H. N. Li, T. B. Yu, L. D. Zhu, and W. S. Wang, "Evaluation of grinding-induced subsurface damage in optical glass BK7," *Journal of Materials Processing Technology*, vol. 229, pp. 785–794, 2016.
- [5] X. He, G. Wang, H. Zhao, and P. Ma, "Subsurface defect characterization and laser-induced damage performance of fused silica optics polished with colloidal silica and ceria," *Chinese Physics B*, vol. 25, no. 4, Article ID 048104, 2016.
- [6] Z. Jia, Y. Su, B. Niu, B. Zhang, and F. Wang, "The interaction between the cutting force and induced sub-surface damage in machining of carbon fiber-reinforced plastics," *Journal of Reinforced Plastics and Composites*, vol. 35, no. 9, pp. 712–726, 2016.
- [7] J. L. Rose, *Ultrasonic Waves in Solid Media*, Cambridge University Press, New York, NY, USA, 1999.
- [8] D. Paehler, D. Schneider, and M. Herben, "Nondestructive characterization of sub-surface damage in rotational ground silicon wafers by laser acoustics," *Microelectronic Engineering*, vol. 84, no. 2, pp. 340–354, 2007.
- [9] X. Cao, F. Jin, and I. Jeon, "Rayleigh surface wave in a piezoelectric wafer with subsurface damage," *Applied Physics Letters*, vol. 95, no. 26, Article ID 261906, 2009.
- [10] C. H. Daros, "On modelling SH-waves in a class of inhomogeneous anisotropic media via the boundary element method," *ZAMM—Zeitschrift für Angewandte Mathematik und Mechanik*, vol. 90, no. 2, pp. 113–121, 2010.
- [11] C. Potel, M. Bruneau, L. C. Foze N'Djomo, D. Leduc, M. Echcherif Elkettani, and J.-L. Izbicki, "Shear horizontal acoustic waves propagating along two isotropic solid plates bonded with a non-dissipative adhesive layer: effects of the rough interfaces," *Journal of Applied Physics*, vol. 118, no. 22, Article ID 224904, 2015.
- [12] A. M. Gaur and D. S. Rana, "Dispersion relations for SH waves propagation in a porous piezoelectric (PZT–PVDF) composite structure," *Acta Mechanica*, vol. 226, no. 12, pp. 4017–4029, 2015.
- [13] Y. Kong, J. Liu, and G. Nie, "Propagation characteristics of SH wave in an mm² piezoelectric layer on an elastic substrate," *AIP Advances*, vol. 5, no. 9, Article ID 097135, 2015.
- [14] Y. Pang, Y. Liu, J. Liu, and W. Feng, "Propagation of SH waves in an infinite/semi-infinite piezoelectric/piezomagnetic periodically layered structure," *Ultrasonics*, vol. 67, pp. 120–128, 2016.
- [15] Y.-D. Li, T. Xiong, and Y. Guan, "Effects of coupled interfacial imperfections on SH wave propagation in a layered multiferroic cylinder," *Ultrasonics*, vol. 66, pp. 11–17, 2016.
- [16] X. Y. Li, Z. K. Wang, and S. H. Huang, "Love waves in functionally graded piezoelectric materials," *International Journal of Solids and Structures*, vol. 41, no. 26, pp. 7309–7328, 2004.
- [17] J. Liu, X. S. Cao, and Z. K. Wang, "Propagation of Love waves in a smart functionally graded piezoelectric composite structure," *Smart Materials and Structures*, vol. 16, no. 1, pp. 13–24, 2007.
- [18] Z. Qian, F. Jin, Z. Wang, and K. Kishimoto, "Transverse surface waves on a piezoelectric material carrying a functionally graded layer of finite thickness," *International Journal of Engineering Science*, vol. 45, no. 2–8, pp. 455–466, 2007.

- [19] X. S. Cao, F. Jin, I. Jeon, and T. J. Lu, "Propagation of Love waves in a functionally graded piezoelectric material (FGPM) layered composite system," *International Journal of Solids and Structures*, vol. 46, no. 22-23, pp. 4123–4132, 2009.
- [20] J. Zhu, W. Q. Chen, G. R. Ye, and J. Z. Fu, "Waves in fluid-filled functionally graded piezoelectric hollow cylinders: a restudy based on the reverberation-ray matrix formulation," *Wave Motion*, vol. 50, no. 3, pp. 415–427, 2013.
- [21] J. G. Yu, B. Wu, and G. Q. Chen, "Wave characteristics in functionally graded piezoelectric hollow cylinders," *Archive of Applied Mechanics*, vol. 79, no. 9, pp. 807–824, 2009.
- [22] Z. K. Wang and F. Jin, "Influence of curvature on the propagation properties of Rayleigh waves on curved surfaces of arbitrary form," *Acta Mechanica Sinica*, vol. 34, no. 6, pp. 895–903, 2002.
- [23] North Carolina State University, <http://nanopatentsandinnovations.blogspot.com/2010/02/smart-nano-coating-opens-door-to-safer.html>.

Research Article

Development of a Composite Technique for Preconditioning of 41Cr4 Steel Used as Gear Material: Examination of Its Microstructural Characteristics and Properties

Jianjun Hu,^{1,2} Chaoping Ma,¹ Hongbin Xu,² Ning Guo,³ and Tianfeng Hou¹

¹College of Material Science and Engineering, Chongqing University of Technology, Chongqing 400054, China

²Chongqing Municipal Key Laboratory of Institutions of Higher Education for Mould Technology, Chongqing 400054, China

³Faculty of Materials and Energy, Southwest University, Chongqing 400715, China

Correspondence should be addressed to Hongbin Xu; kbe@vip.cqut.edu.cn and Ning Guo; guoning_1000@163.com

Received 22 May 2016; Revised 23 July 2016; Accepted 10 August 2016

Academic Editor: Parashuram Sahoo

Copyright © 2016 Jianjun Hu et al. This is an open access article distributed under the Creative Commons Attribution License, which permits unrestricted use, distribution, and reproduction in any medium, provided the original work is properly cited.

Commercial 41Cr4 (ISO standard) steel was treated by a composite technique. An intermediate layer was introduced firstly at the 41Cr4 steel surface by traditional carburizing and nitriding. Then a hard Cr coating was brush-plated on the intermediate layer. Finally, the coating layer was modified by high current pulsed electron beam (HCPEB), followed by quenching and subsequent tempering treatment. The microstructure, mechanical properties, and fracture behavior were characterized. The results show that a nanocrystalline Cr coating is formed at the 41Cr4 steel surface by the treatment of the new composite technique. Such nanocrystalline Cr coating has acceptable hardness and high corrosion resistance performance, which satisfies the demands of the gears working under high speed and corrosive environment. The composite process proposed in this study is considered as a new prospect method due to the multifunction layer design on the gear surface.

1. Introduction

Gear is a vital device in the gear transmission system which can transmit power, change the direction and speed of movements, and influence the performance of the whole equipment [1]. With the progress of technology and the development of gear transmission, the gear is developed towards high speed, heavy load, complex service environment, and high reliability. Moreover, more strict requirements such as large gear ratio, efficiency transmission, and lightweight are necessities for the gears used in aviation, aerospace, and navigation fields [2–4]. However, it is difficult to achieve those goals through increasing modulus or thickness of the gears. Instead, the applications and developments of surface treatment techniques for improving the strength of the gear tooth face are considered as a potentially effective approach.

Traditionally, tooth face strengthening methods, such as carburizing, nitriding, surface and quenching, have been

applied singly to harden the gears. It has been reported that both surface hardness and wear resistance can be improved by the application of single traditional method [5–9]. Modern gears often work under complex circumstance, such as high speed, high temperature, and highly corrosive environment, which results in a multifunction of the gear surface. However, such multifunction gear cannot be obtained by singly using traditional methods. It has been reported that coating with Cr layers on the materials is an important engineering practice to improve the corrosion resistance. High current pulsed electron beam (HCPEB) treatment has been reported as an effective way for strengthening the bonding force between coating layer and substrate [10]. Thus, in this work, a composite process has been developed to treat 41Cr4 steel which is widely used as gear materials. Microstructures, mechanical properties, and fracture behavior of the 41Cr4 steel treated by the new composite process have been characterized and discussed.

2. Experimental Section

Commercial 41Cr4 steel (0.40% C, 0.8% Cr, Ni \leq 0.30%, 0.23% Si, and 0.7% Mn in wt.) was chosen as the original materials in this study. Conventional carburizing and nitriding treatments have been carried out firstly in order to introduce an intermediate layer on the surface of the original materials. Brush-plating was performed on the intermediate layer to obtain Cr coating after carburizing and nitriding processes. A direct current power pack (MBPK-50A) was performed with a voltage of 10 V. HCPEB (RITM-2M type) treatment with a voltage of 27 KV and a pulse number of 35 was carried out followed by subsequent quenching at 850°C and tempering at 250°C for 25 minutes, respectively.

Microstructures were observed with a metallographic microscope (Carl Zeiss A10), a super depth filed microscopy (Kean VR-3000), and a field emission gun scanning electron microscope (FEG-SEM, Zeiss Sigma HD). Both secondary electron imaging (SEI) and back-scattered electron imaging (BSEI) techniques were carried out for the characterization of the microstructure. The composition distribution along the depth direction of the gear surface was analyzed by the energy dispersive spectrometer (EDS) equipped in the FEG-SEM. Microhardness along the depth direction was tested by a hardness tester (HVS-1000) with a load of 0.5 N and a loading time of 10 s. The reciprocating dry sliding was carried out on a ball-on-flat tribometer (HSR-2M). The friction pair was Si₃N₄ ceramic ball (hardness 1800 HV) with a diameter of 6 mm. The corrosion resistance performance was carried out on a PAR273A constant potential instrument. Potentiodynamic polarization potential ranged from -0.1 to 0.5 V.

3. Results and Discussion

3.1. Microstructure. Surface microstructures of Cr coating prepared by brush-plating before and after HCPEB treatment are illustrated in Figures 1(a) and 1(b), respectively. It can be seen that, before HCPEB, the Cr coating shows morphology of nonuniform equiaxed nodular units (the average size is 26 μm in diameter), rather than polycrystalline structures. Such morphology resulted by the combined action of continuous supply of plating solution, contact pressure, and speed between anode and cathode [11–14]. In contrast, after HCPEB treatment, the surface of the Cr coating is more smooth, and all the small equiaxed nodular units almost disappear, which results in a uniform distribution of equiaxed nodular units (the average size is 46 μm in diameter,) within the Cr coating (see Figure 1(b)). However, as shown in Figure 1(b), there are some small cracks and erupted craters existing within the Cr coating, suggesting that rapid melting and cooling have taken place during the HCPEB treatment. Cracks within the coating are considered as the results of residual thermal stress which are formed due to the rapid cooling rates of HCPEB. It has been reported that internal tensile stress is existing in deposited nickel-tungsten alloy coating, which results in some small cracks within the coating [15]. When the brush-plated Cr is irradiated with HCPEB, high energy electron beam is deposited on the Cr coating. Figure 1(b) indicates that

the equiaxed nodular units form during brush-plating and regrow into nodular shape again during HCPEB treatment. It is more important that the uniform microstructure has been obtained by the effect of such melting and regrowth of Cr coating during HCPEB treatment.

Figure 2 shows the sectional view images of the sample surface after quenching and tempering. From Figure 2(a), it can be seen that the thickness of the Cr coating is about 112 μm and there are some cracks existing in the Cr coating. Both Cr and Fe distributions along the depth direction are determined by EDS line scanning, as shown in Figure 2(b). It shows clearly that a Cr layer has been coated on the 41Cr4 matrix. More Fe has been diffused into the Cr coating, while only a few of Cr exist in the 41Cr4 matrix. It indicates that Fe has a faster diffusion rate than Cr during the diffusion process. The sectional view images of the sample surface are also characterized by BSEI technique, as shown in Figure 3. It is well known that BSEI can display topography contrast, Z-contrast, and electron channeling contrast (ECC) information [16]. It can be seen that the 41Cr4 matrix has a pearlite microstructure (topography contrast), while the Cr coating has polycrystalline characteristics (ECC). The average grain size is determined as 260 nm (see Figure 2(d)). It is reported that, with quenching at 850°C followed by tempering at 250°C, the material surface is heated to cause recrystallization of Cr coating particles [11, 17]. It indicates that the crystallization behavior of the nodular shape particles of the Cr coating formed during HCPEB treatment has taken place during the subsequent quenching and tempering process.

Overall, a Cr coating composed by inhomogeneous nodular Cr particles is formed firstly after brush-plating. Then, such inhomogeneous structure is improved by the HCPEB treatment. Finally, the uniform nodular Cr particles are changed into polycrystalline structure with average grain size in nanoscale. That is, a nanocrystalline Cr coating is generated on the intermediate layer.

3.2. Microhardness. Figure 3 shows the sectional hardness plotted versus depth of the 41Cr4 steel treated by the new composite method. It can be seen that the microhardness of the 41Cr4 matrix is about 335 HV_{0.5}. And the microhardness of the sample after brush-plated Cr coating is about 932 HV_{0.5}. The section hardness of the sample after brush-plated Cr coating gradually decreased from the surface of 932 HV_{0.5} to about 648 HV_{0.5} at 880 μm and then eventually slightly increases to about 700 HV. In addition, no acute fluctuation is witnessed in the process of change. Moreover, it can be roughly estimated that the thickness of hard layer, the hardness of which is higher than 720 HV_{0.5}, is up to 280 μm . Therefore, it can be concluded that this process makes the hardness increase gradually from the core to material surface. And it also further illustrates that this process makes the performance of the gear section realize gradient change [18, 19].

3.3. Fracture Behavior. Artificial broken sample is used in the experimental process to further study the comprehensive

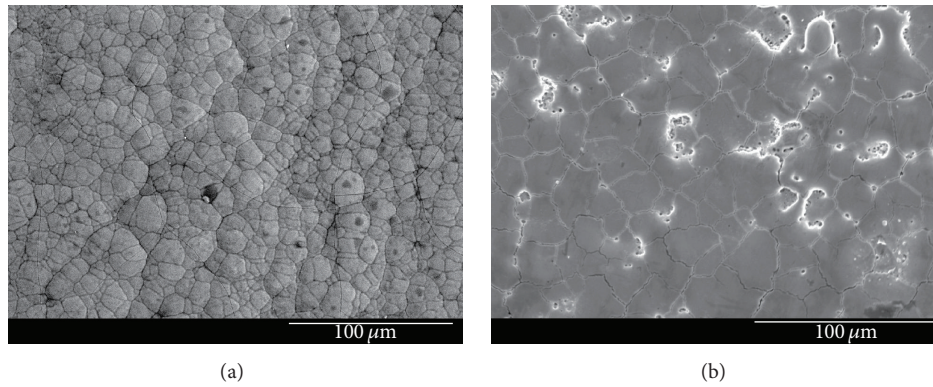


FIGURE 1: View of the surface morphology of Cr coating before (a) and after (b) HCPEB treatment. The images are obtained by SEI technique.

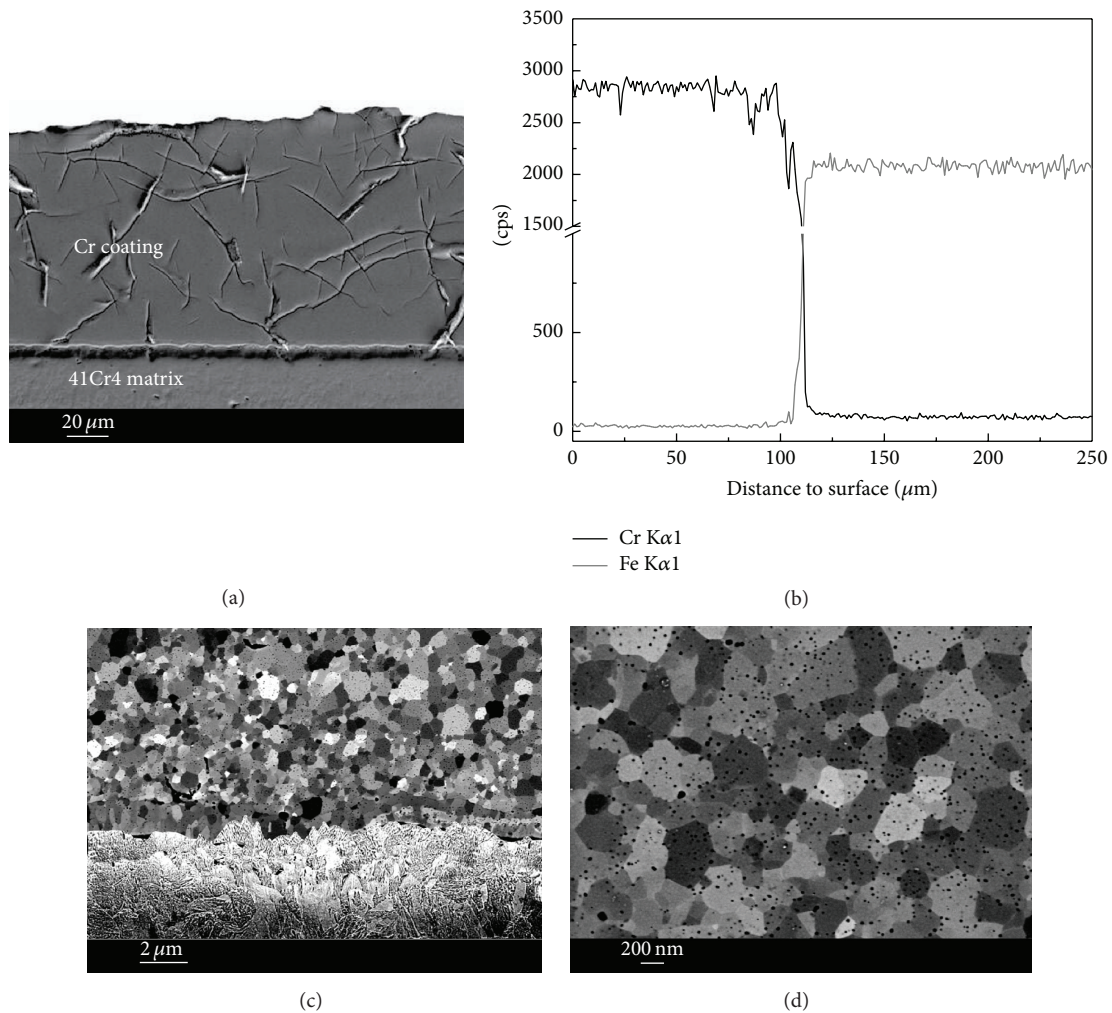


FIGURE 2: Sectional view of microstructure of the sample surface: (a) SEI image, (b) line scanning of EDS, (c) BSEI image, and (d) high magnification BSEI showing nanocrystalline Cr.

performance of the 41Cr4 steel treated by the composite process. The SEI technique is used to observe the fracture morphology from macro and micro perspectives, respectively, as shown in Figure 4.

The outer surface of the Cr coating is very flat in macro view, where a series of cleavage fracture appearances is

observed (marked as Zone 1 in Figure 4(a)). Small stepped cleavage plane almost parallel to the direction of crack propagation can be seen in micro view, which is known as the river pattern fracture. Adjacent to the Cr coating, the fracture feature of the pearlite matrix (Zone 2 in Figure 4(a)) is revealed in Figure 4(c) and amplified in Figure 4(d). Clearly,

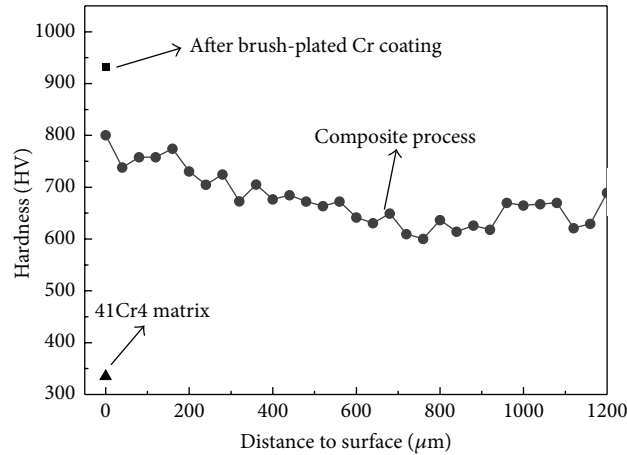


FIGURE 3: Microhardness plotted as a function of depth to the sample surface.

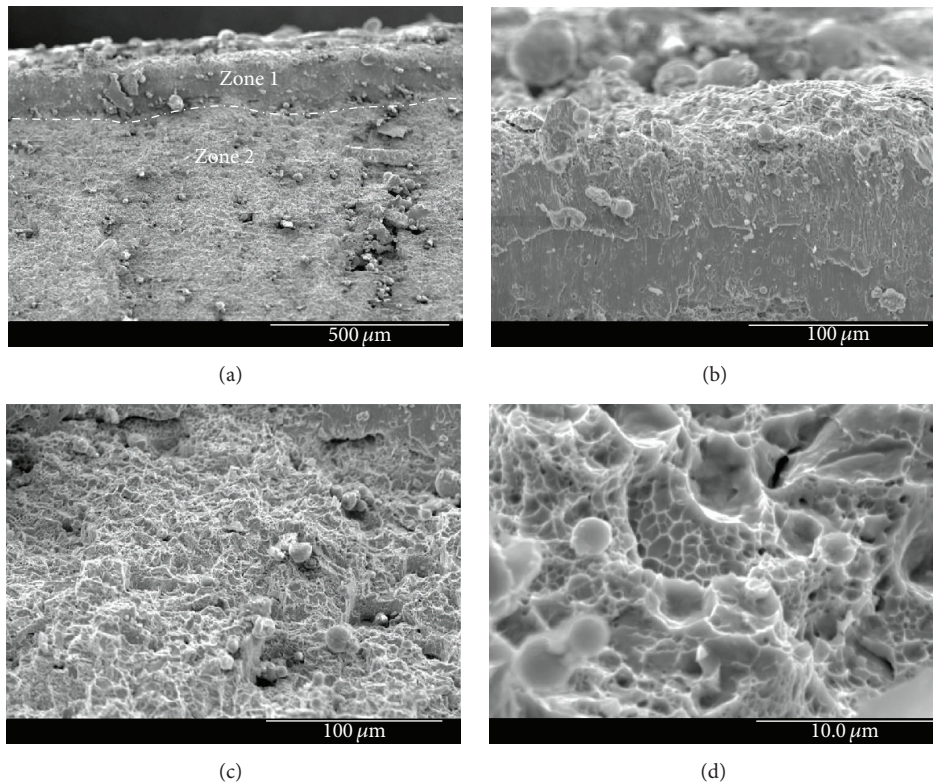


FIGURE 4: Fracture morphology of (a) the overall feature in (b) Zone 1 and in (c) Zone 2 and (d) high magnification of Zone 2.

many typical ductile dimples are observed in Zone 2, which indicates that the matrix has good plasticity. That is, the fracture morphology of the sample is gradually transformed from cleavage pattern in the coating to ductile dimple in the matrix. According to the micro mechanism of fracture, dimples are the results of microporous growth and often include inclusion or a second phase, which proves that the microvoids form at the interface between the inclusions or second phase and the substrate. The diameter and depth of dimples depend on the quantity distribution of the second

phase and the plastic deformation ability of 41Cr4 matrix. Dimples are large and deep when the second phase is less and has uniform distribution, and the plastic deformation ability of substrate is strong as well. The dimples are large and shallow when the work hardening ability of substrate is very strong. Besides, the formation of the microvoids has two ways in this study: one is the fracture of interface which is between the substrate and the second phase particles and the other is the fracture induced by stress action between the two neighbor second phase particles. Under the internal

stress, the microvoids grow up gradually, which results in the final fracture during tensile test. Therefore, the fracture of the 41Cr4 matrix is ductile in this study.

For the samples treated by the composite technique, from surface to core, the fracture morphology shows a gradient change which evolves continuously from cleavages into ductile dimples. The river pattern fracture is observed in the sample surface because the crack grows along two adjacent paralleling cleavage planes with narrow spacing in the surface layer. Although the appearance of cleavage morphology generally implies brittle characteristics, it maintains relatively high hardness (see Figure 3) which is very important for high wear resistance. When moving towards the core of the sample, the tempered pearlite shows excellent toughness, and small microvoids gradually form in these places and grow into dimple during tensile test. It is concluded that high wear resistance and good toughness of 41Cr4 gear material have been realized via the new composite technique.

3.4. Friction Coefficient. Figure 5 shows the coefficient of friction of the 41Cr4 matrix and the sample with composite process. It can be seen that the friction coefficient of 41Cr4 matrix increases sharply into the maximum value of 0.22 during 0–0.7 min and then decreases gradually (0.7–2.3 min). However, after 2.3 min, it comes into a stable state with a mean friction coefficient of 0.17. For the sample with composite process, originally, the coefficient of friction has a rather higher value (about 1.55), and then it decreases into about 0.73 at 0.47 min. During 0.5–4.0 min, it suffers an increasing-decreasing-increasing change. After 4.0 min, it decreases into 0.78 gradually. This suggests that the coefficient of friction is very high at the beginning of contact due to the rough and hard material surface. However, it is still relatively low because the friction is still at the running stage and wears lightly. With increasing time, the friction coefficient starts to go up due to the micro convex body on the friction pair surface at the initial stage. With friction further developing, the ceramic ball is ground into a continually smoother surface, while the Cr coating is gradually oxidized and even generates wear debris. Thus, the original two-body friction converts into the three-body friction which greatly increases the wear rate. The friction coefficient decreases gradually with increasing time. Finally, the friction was developed into the stable wear stage.

3.5. Corrosion Resistance. The potentiodynamic polarization curves of the 41Cr4 matrix and sample with composite process are shown in Figure 6. Clear differences in the corrosion behavior of the two samples can be depicted. The sample of the 41Cr4 matrix has slightly larger corrosion current density (i_{cor}) and lower corrosion potential (E_{cor}) than the sample with composite process. So, the corrosion resistance of 41Cr4 treated by carburizing and nitriding and then brush-plating Cr after treatment with electron beam was significantly improved compared with the 41Cr4 matrix [14, 20].

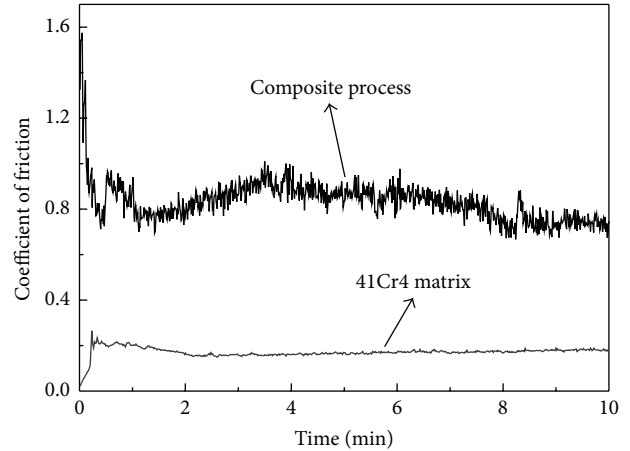


FIGURE 5: The friction coefficient plotted as a function of loading time.

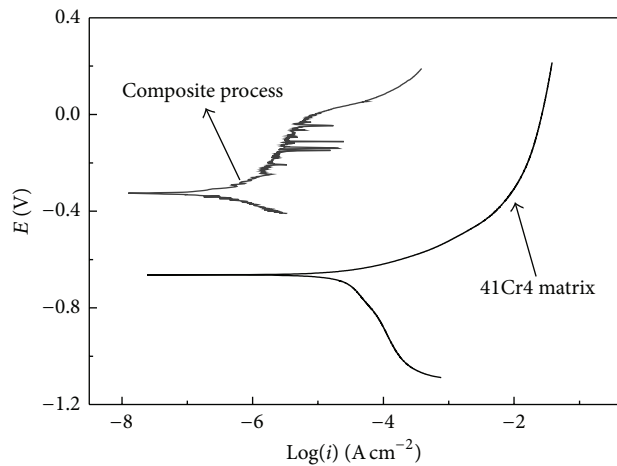


FIGURE 6: Polarization curve of 41Cr4 steel treated by the composite process.

4. Conclusions

Commercial 41Cr4 steel has been processed by a new composite process method in this study. Microstructure feature, mechanical properties, and fracture feature have also been characterized. Some conclusions can be drawn as follows:

- (i) A nanocrystalline Cr coating layer is formed on the 41Cr4 steel surface after the treatment of the composite process.
- (ii) The nonuniform microstructure of brush-plated Cr coating could be improved by remelting and regrowth behavior of Cr coating during HCPEB treatment.
- (iii) The hardness increases gradually from core to surface of the 41Cr4 sample. The nanocrystalline Cr coating has acceptable hardness and is considered to have high corrosion resistance performance.

Competing Interests

The authors declare that they have no competing interests.

Acknowledgments

This study was supported by the National Natural Science Foundation of China (51275548 and 51575073), International Cooperation Special Project in Science and Technology of China (2015DFR70480), and Scientific and Technological Research Program of Chongqing (KJ1400902 and cstc2014gjh70003).

References

- [1] R. K. Pandey, "Failure analysis of coal pulveriser gear box," *Engineering Failure Analysis*, vol. 14, no. 4, pp. 541–547, 2007.
- [2] H. C. Kim, "Sector gear and gas-insulated switchgear having the same," Patent US20130167675, 2013.
- [3] G. Meschut, O. Hahn, D. Teutenberg, and L. Ernstberger, "Influence of the dosing and mixing technology on the property profile of two-component adhesives," *Welding in the World*, vol. 59, no. 1, pp. 91–96, 2015.
- [4] V. Ngo, T. Hofman, M. Steinbuch, and A. Serrarens, "Effect of gear shift and engine start losses on energy management strategies for hybrid electric vehicles," *International Journal of Powertrains*, vol. 4, no. 2, pp. 141–162, 2015.
- [5] X. Nie, "Study of the rapid surface modification technology," *Heat Treatment of Metals*, no. 3, pp. 19–22, 1997.
- [6] M. Tarakci, K. Korkmaz, Y. Gencer, and M. Usta, "Plasma electrolytic surface carburizing and hardening of pure iron," *Surface & Coatings Technology*, vol. 199, no. 2–3, pp. 205–212, 2005.
- [7] Z. J. Tian, L. I. Jie, D. J. Shen, and Y. L. Wang, "Liquid phase plasma electrolytic carburizing, nitriding, carbonitriding technique," *Electroplating & Finishing*, vol. 25, no. 2, pp. 53–56, 2006.
- [8] C. Tsotsos, A. L. Yerokhin, A. D. Wilson, A. Leyland, and A. Matthews, "Tribological evaluation of AISI 304 stainless steel duplex treated by plasma electrolytic nitrocarburising and diamond-like carbon coating," *Wear*, vol. 253, no. 9–10, pp. 986–993, 2002.
- [9] A. L. Yerokhin, A. Leyland, C. Tsotsos, A. D. Wilson, X. Nie, and A. Matthews, "Duplex surface treatments combining plasma electrolytic nitrocarburising and plasma-immersion ion-assisted deposition," *Surface & Coatings Technology*, vol. 142–144, no. 7, pp. 1129–1136, 2001.
- [10] D. Wu, J. Zhang, J. C. Huang, H. Bei, and T. G. Nieh, "Grain-boundary strengthening in nanocrystalline chromium and the Hall-Petch coefficient of body-centered cubic metals," *Scripta Materialia*, vol. 68, no. 2, pp. 118–121, 2013.
- [11] D. B. Bober, M. Kumar, and T. J. Rupert, "Nanocrystalline grain boundary engineering: increasing $\Sigma 3$ boundary fraction in pure Ni with thermomechanical treatments," *Acta Materialia*, vol. 86, pp. 43–54, 2015.
- [12] X. Bin-Shi, W. Hai-Dou, D. Shi-Yun, and J. Bin, "Fretting wear-resistance of Ni-base electro-brush plating coating reinforced by nano-alumina grains," *Materials Letters*, vol. 60, no. 5, pp. 710–713, 2006.
- [13] B. Wu, B.-S. Xu, B. Zhang, X.-D. Jing, and C.-L. Liu, "Automatic brush plating: an update on brush plating," *Materials Letters*, vol. 60, no. 13–14, pp. 1673–1677, 2006.
- [14] B. Subramanian, S. Mohan, and S. Jayakrishnan, "Structural, microstructural and corrosion properties of brush plated copper-tin alloy coatings," *Surface and Coatings Technology*, vol. 201, no. 3–4, pp. 1145–1151, 2006.
- [15] Y. D. Gamburg and G. Zangari, *Theory and Practice of Metal Electrodeposition*, Springer, New York, NY, USA, 2011.
- [16] N. Guo, Q. Liu, Y. C. Xin, B. F. Luan, and Z. Zhou, "The application of back-scattered electron imaging for characterization of pearlitic steels," *Science China Technological Sciences*, vol. 54, no. 9, pp. 2368–2372, 2011.
- [17] J. Zou, T. Grosdidier, K. Zhang, and C. Dong, "Mechanisms of nanostructure and metastable phase formations in the surface melted layers of a HCPEB-treated D2 steel," *Acta Materialia*, vol. 54, no. 20, pp. 5409–5419, 2006.
- [18] J. J. Hu, G. B. Zhang, H. B. Xu, and Y. F. Chen, "Microstructure characteristics and properties of 40Cr steel treated by high current pulsed electron beam," *Materials Technology*, vol. 27, no. 4, pp. 300–303, 2012.
- [19] J. Cheol Oh, D.-K. Choo, and S. Lee, "Microstructural modification and hardness improvement of titanium-base surface-alloyed materials fabricated by high-energy electron beam irradiation," *Surface and Coatings Technology*, vol. 127, no. 1, pp. 76–85, 2000.
- [20] Z. Zhong and S. J. Clouser, "Nickel-tungsten alloy brush plating for engineering applications," *Surface and Coatings Technology*, vol. 240, pp. 380–386, 2014.

Research Article

The Definition Method and Optimization of Atomic Strain Tensors for Nuclear Power Engineering Materials

Xiangguo Zeng, Ying Sheng, Huayan Chen, and Tixin Han

College of Architecture and Environment, Sichuan University, Chengdu 610065, China

Correspondence should be addressed to Ying Sheng; shengying_2008@163.com

Received 5 June 2016; Accepted 11 July 2016

Academic Editor: Yan Yang

Copyright © 2016 Xiangguo Zeng et al. This is an open access article distributed under the Creative Commons Attribution License, which permits unrestricted use, distribution, and reproduction in any medium, provided the original work is properly cited.

A common measure of deformation between atomic scale simulations and the continuum framework is provided and the strain tensors for multiscale simulations are defined in this paper. In order to compute the deformation gradient of any atom m , the weight function is proposed to eliminate the different contributions within the neighbor atoms which have different distances to atom m , and the weighted least squares error optimization model is established to seek the optimal coefficients of the weight function and the optimal local deformation gradient of each atom. The optimization model involves more than 9 parameters. To guarantee the reliability of subsequent parameters identification result and lighten the calculation workload of parameters identification, an overall analysis method of parameter sensitivity and an advanced genetic algorithm are also developed.

1. Introduction

Titanium alloys have been largely used as nuclear power engineering materials [1], and it is important and significant to analyze the atomic-level strain distribution of these materials. The strain tensors are commonly defined by the local deformation of the continuum. Unlike displacement, strain is not a physical quantity that can be measured directly, and it is calculated from a definition that relies on the gradient of the continuous displacement field. At the microscale, it is difficult to define the local deformation according to the position of each atom which is obtained from the adjacent discrete time interval, so there is no universally accepted definition of strain tensors of atomic scale so far.

Many engineering problems involving physical phenomena need to calculate strain tensors at atomic scale. Wang et al. [2] pointed that it was important to analyze the atomic-level strain distribution and get the atomic stress-strain curve while studying the mechanical behavior of Zr-based metallic glass under indentation. Hirth et al. [3] considered that the computation of the deformation gradient and strain tensors made the approach useful for evaluation of continuum models, development of microstructure and mechanical property relationships, and identification of dislocations and

disclinations, as well as for quantification of plastic spin and strain gradients.

In recent years, many researchers are challenging to provide a common measure of deformation between atomic scale simulations and the continuum framework and define the strain tensors for multiscale simulations. Zimmerman et al. [4] defined the slip vector according to the positions of atoms and successfully identified the lattice distortion and the formation of dislocation structures, but these measures could not be utilized in the continuum framework. Mott et al. [5] presented a definition of the local atomic strain increments in three dimensions and an algorithm for computing them. First, an arbitrary arrangement of atoms was tessellated into Delaunay tetrahedra, and then the deformation gradient increment tensor for interstitial space was obtained from the displacement increments of the corner atoms of Delaunay tetrahedra. However, it was complicated to establish the tetrahedral elements of atoms. Gullett et al. [6] proposed an atomic strain tensor that is based on the definition of a discrete equivalent to the continuum deformation gradient that accounts for the relative motion of an atom and its neighbors in a nonlocal fashion. This method was computationally efficient, because the deformation gradient arose from an optimization procedure that did not rely on a geometric decomposition,

and the strain tensors were computed directly from the deformation gradient and were appropriate for general finite, multiaxial deformation states. When the deformation gradient at an atom was formed, a weight function should be built to eliminate the different contributions within the neighbor atoms which had different distances to the atom. However, Gullett et al. [6] did not study the establishment and optimization method of the weight function which played an important role in the formulation of the discrete deformation but just used the invariant weight function of the artificial assumption to calculate the discrete deformation gradient at the atom.

By summarizing the shortcomings of the existing methods mentioned above, the work done by this paper can be categorized into three parts: first, the strain tensors for multi-scale simulations are defined, and the weighted least squares error optimization model involving more than 9 parameters is established to seek the optimal coefficients of the weight function and the optimal local deformation gradient of each atom; next, to guarantee the reliability of subsequent parameters identification result and also to lighten the calculation workload of parameters identification, an overall analysis method of parameter sensitivity, based on Latin Hypercube Sampling method and Spearman rank correlation method, is proposed; furthermore, on the fundamentals of the result of parameter sensitivity and basic genetic algorithm (GA), an advanced genetic algorithm based on the advanced niche genetic algorithm, global peak value determination strategy, and local accurate searching techniques is developed. Finally, taking alpha titanium as an example, the strain tensors of atoms are computed by means of the method proposed in this paper, and the method is proved to be correct and feasible by comparing with the results got by other methods from the existing reference.

2. Modeling Approach

2.1. Deformation Gradient and Strain Tensors. In order to describe the positions of atoms at the initial time t_0 and at the current time t , we assume a fixed Cartesian coordinate system as shown in Figure 1.

In Figure 1, \mathbf{X} and \mathbf{x} are, respectively, the coordinate vectors of atoms in the reference configuration Ω_0 at the initial time t_0 and in the current configuration Ω_1 at the current time t , and χ maps the atoms from \mathbf{X} to \mathbf{x} . Consider

$$\begin{aligned} \mathbf{X} &= X_i \mathbf{E}_i, \\ \mathbf{x} &= x_i \mathbf{e}_i, \\ \mathbf{x} &= \chi(\mathbf{X}). \end{aligned} \quad (1)$$

Assuming sufficient continuity, the local deformation at \mathbf{X} is characterized as the gradient of the motion and can be defined as

$$\mathbf{F} \equiv \frac{\partial \chi}{\partial \mathbf{X}} = \frac{\partial \mathbf{x}}{\partial \mathbf{X}}. \quad (2)$$

The deformation of an infinitesimal segment $d\mathbf{x}$ at one point in the reference configuration can be expanded in

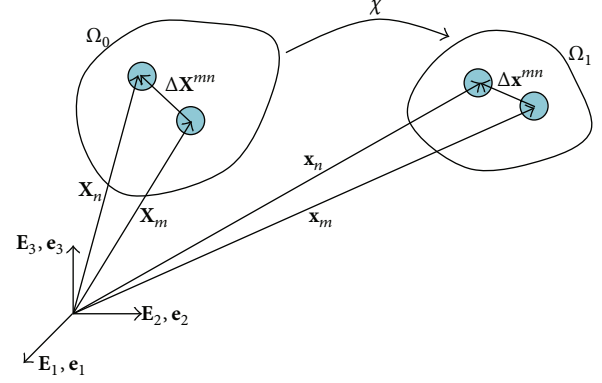


FIGURE 1: General motion in the neighborhood of a discrete atomic particle.

a Taylor series. If the higher-order terms are omitted, $d\mathbf{x}$ can be written as

$$\begin{aligned} d\mathbf{x} &= \chi(\mathbf{X} + d\mathbf{X}) - \chi(\mathbf{X}) \\ &= \chi(\mathbf{X}) + \nabla \chi(\mathbf{X}) \cdot d\mathbf{X} + o(d\mathbf{X}) - \chi(\mathbf{X}) \\ &\approx \nabla \chi(\mathbf{X}) \cdot d\mathbf{X} \approx \mathbf{F} \cdot d\mathbf{X}. \end{aligned} \quad (3)$$

Then the deformation gradient \mathbf{F} can be got by (3) which is not only applicable to atomic scale but also available for the continuum framework. Consider an atomic system shown in Figure 1. The deformation in the neighborhood of atom m is characterized by the changes in the relative position of its neighbors. Atom m is located at the position \mathbf{X}^m in the reference configuration Ω_0 and position \mathbf{x}^m in the current configuration Ω_1 . Then the relative position of neighboring atom n and the deformation gradient \mathbf{F}^m at atom m are given as

$$\begin{aligned} \Delta \mathbf{X}^{mn} &= \mathbf{X}^n - \mathbf{X}^m \\ \Delta \mathbf{x}^{mn} &= \mathbf{x}^n - \mathbf{x}^m \\ \Delta \mathbf{x}^{mn} &= \mathbf{F}^m \cdot \Delta \mathbf{X}^{mn}. \end{aligned} \quad (4)$$

The deformation gradient of atom m is related to its neighboring atoms, and the deformation gradient of each neighboring atom with respect to atom m is different, so the deformation gradient \mathbf{F}^m of atom m cannot generally be got by a single atom n . Therefore, we should seek an optimal local deformation gradient $\hat{\mathbf{F}}^m$, which can make the weighted squares error W^m shown in the following equation minimized:

$$W^m = \sum_{n=1}^N (\Delta \mathbf{x}^{mn} - \hat{\mathbf{F}}^m \Delta \mathbf{X}^{mn})^T (\Delta \mathbf{x}^{mn} - \hat{\mathbf{F}}^m \Delta \mathbf{X}^{mn}) \omega_n, \quad (5)$$

where N is the number of neighboring atoms and ω_n is a weight factor.

The optimal deformation gradient $\hat{\mathbf{F}}^m$ of the atom m is determined by the deformation gradients of all the neighboring atoms with respect to atom m , but the contribution of each atom n to $\hat{\mathbf{F}}^m$ is different and related to the distance between atom n and atom m . Therefore, the weight function used

to eliminate the different contributions within the neighbor atoms which had different distances to the atom. In the cutoff radius r_{cut} that specifies the domain around atom m , ω_n of the nearest neighbor atom is equal to 1.0 and gradually reduced to 0.0 with the increase of the distance between atom n and atom m . The weight function ω_n plays an important role on calculating the atomic strain. For each material, the weight function curve must be uniquely determined, but it is difficult to get the exact analytic expression of the weight function corresponding to the weight function curve, so many forms of ω_n can be assumed and the coefficients of the function should be optimized to fit the weight function curve. The S-curve model of biological population growth is proved to be one of the appropriate forms to fit the weight function curve [7], so the appropriate weight function ω_n can be assumed as

$$\omega_n = \frac{2 + k_1}{1 + k_1} - \frac{1}{1 + k_1 e^{-k_2 r}} \quad (6)$$

$$r = \frac{R_{mn} - r_{g1}}{r_{\text{cut}}},$$

where k_1 and k_2 are undetermined coefficients, R_{mn} is the distance between atom n and atom m , and r_{g1} is the distance between the closest neighbor atom and atom m .

The purpose of parameters identification is to find a set of solutions of discrete design variables \mathbf{X} to satisfy the objective function $W^m(\mathbf{X})$ as shown in

$$\begin{aligned} \text{obj: min } & W^m(\mathbf{X}) \\ & = \sum_{n=1}^N (\Delta \mathbf{x}^{mn} - \hat{\mathbf{F}}^m \Delta \mathbf{X}^{mn})^T (\Delta \mathbf{x}^{mn} - \hat{\mathbf{F}}^m \Delta \mathbf{X}^{mn}) \omega_n \\ \mathbf{X} & \\ & = [\hat{F}_{11}^m, \hat{F}_{12}^m, \hat{F}_{13}^m, \hat{F}_{21}^m, \hat{F}_{22}^m, \hat{F}_{23}^m, \hat{F}_{31}^m, \hat{F}_{32}^m, \hat{F}_{33}^m, k_1, k_2]^T \\ \text{s.t.: } & \bar{X}_{i\min} \leq X_i \leq \bar{X}_{i\max}. \end{aligned} \quad (7)$$

When the objective function $W^m(\mathbf{X})$ reaches the minimum, the parameters \hat{F}_{ij}^m ($i, j = 1, 2, 3$) are the optimal components of the optimal deformation gradient matrix $\hat{\mathbf{F}}^m$.

When $\hat{\mathbf{F}}^m$ is determined by the optimization model as shown in (7), the Lagrangian Green strain tensor \mathbf{E} is defined with respect to reference coordinates in terms of this quantity as

$$\mathbf{E} = \frac{1}{2} (\mathbf{F}^T \mathbf{F} - \mathbf{I}). \quad (8)$$

The strain tensor \mathbf{E} is a 3×3 matrix, and the effective strain of a point ε_{eff} can be described by the second invariants of \mathbf{E} , shown as

$$\begin{aligned} \varepsilon_{\text{eff}} & = \sqrt{3J_2} \\ & = \sqrt{3 \left(\begin{vmatrix} E_{11} & E_{12} \\ E_{21} & E_{22} \end{vmatrix} + \begin{vmatrix} E_{22} & E_{23} \\ E_{32} & E_{33} \end{vmatrix} + \begin{vmatrix} E_{11} & E_{13} \\ E_{31} & E_{33} \end{vmatrix} \right)}. \end{aligned} \quad (9)$$

2.2. Parameter Sensitivity Analysis. The optimization model (see (7)) involves 11 parameters. To guarantee the reliability of subsequent parameters identification result and also to lighten the calculation workload of parameters identification, an overall analysis method of parameter sensitivity, based on Latin Hypercube Sampling method and Spearman rank correlation method, is proposed.

Sensitivity analysis means picking out those sensitive parameters, which could significantly affect the reliability of result, among wide range of uncertain factors. A traditional analysis method is called single factor analysis method. And the basic procedures are as follows [8].

- (1) Build systematic model, meaning function relation between system feature and factors, $P = W(x_1, x_2, \dots, x_m)$, and get the benchmark sets of parameters.
- (2) When analyzing the effect of one particular parameter x_i on feature P , keep the rest of parameters constant in basic value, and only allow parameter x_i to vary within the proper range. If minor change of x_i leads to drastic changes of P , that means P is very sensitive to x_i , and the sensitivity value of x_i is large; if x_i varies within a rather wide range, while the change in P is not obvious, that means P is not sensitive to x_i , and the sensitivity value of x_i is small.

The optimization model (see (7)) obtained in this paper is nonlinear, and parameters are related to each other. All the parameters collectively affect the fitting accuracy of the objective function $W^m(\mathbf{X})$ as shown in (7). Hence, overall analysis of parameter sensitivity is required, which means allowing every parameter simultaneously to change within assigned ranges, to observe the effect of each parameter on objective function.

To thoroughly analyze all the changing parameters, first, we need to pick up samples from the whole parameters space. Latin Hypercube Sampling (LHS) is a uniformed space sampling method, proposed earliest by McKay et al. in 1979 [9], which possesses advantages of fewer sampling times and effectively avoiding repeat sampling, and applies to complicated multidimensional parameters space sampling. The basic procedures of LHS are as follows.

- (1) Set a parameter set consisting of m parameters, and set the value range of each parameter as n nonoverlap zones with equal probability.
- (2) Randomly pick a sample of every parameter x_i within its range, meaning each parameter x_i consists of n sample values.
- (3) Randomly arrange the n sample values of each x_i , to form m random arrangements.
- (4) Pick up one sample value for each parameter from the m arrangements, which could form a sample parameter set \mathbf{X}_k and pick n times in sequence, and then one will get n sample parameter sets $\{\mathbf{X}_1, \mathbf{X}_2, \dots, \mathbf{X}_n\}$.

The realization process schematic drawing of LHS method is shown in Figure 2.

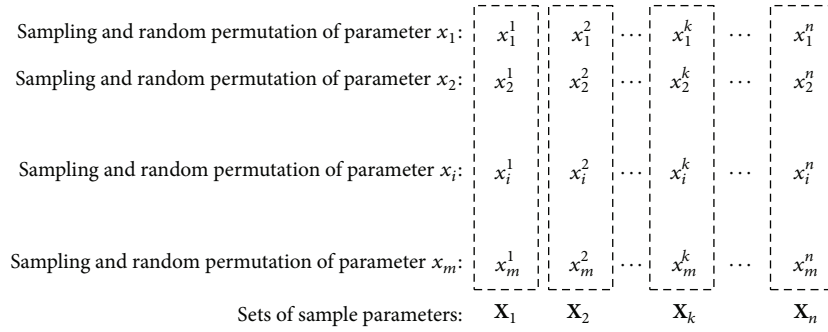


FIGURE 2: The realization process schematic drawing of LHS method.

Since the optimization model (see (7)) obtained in this paper is nonlinear, the output result of random sampling sample sets is uncertain. Therefore, it is necessary to adopt nonparameter statistical method to carry out the relativity analysis among random parameters. Spearman rank correlation method is a nonparameter statistical analysis method, proposed by Spearman in 1904 [10]. This method applies to relativity analysis among multiple parameters, to analyze the effect of input parameters on the output result. This is a very practical method [11]. The basic procedures of Spearman rank correlation method are as follows.

- (1) Definition of rank: by arranging the sample sets $\{A_1, A_2, \dots, A_n\}$ from large to small, an ordered sequence A is formed. Supposing A_i is at the order of R_i in the sequence A , then R_i is the rank of A_i in $\{A_1, A_2, \dots, A_n\}$.
- (2) By substitution of n sets of sample parameters $\{\mathbf{X}_1, \mathbf{X}_2, \dots, \mathbf{X}_n\}$ into (7), the solution sets of objective function $\{W_1, W_2, \dots, W_n\}$ can be obtained.
- (3) Supposing the rank of the parameter x_i^k in $\{x_i^1, x_i^2, \dots, x_i^n\}$ is α_k and the rank of the parameter W_k in $\{W_1, W_2, \dots, W_n\}$ is β_k , then the sensitivity of parameter x_i equals the absolute value of Spearman rank correlation coefficient, as shown in

$$r_i = \left| \frac{n \sum_{k=1}^n a_k b_k - \sum_{k=1}^n a_k \sum_{k=1}^n b_k}{\sqrt{n \sum_{k=1}^n (a_k)^2 - (\sum_{k=1}^n a_k)^2} \sqrt{n \sum_{k=1}^n (b_k)^2 - (\sum_{k=1}^n b_k)^2}} \right|. \quad (10)$$

Arrange the sensitivity degree r_i of all the parameters from large to small, the larger sensitivity degree means greater impact on output result, which requires close attention in subsequent parameter identification analysis.

The result of parameter sensitivity analysis obtained through this method forms the basic theory for the purpose of determining the density of optimization model parameter discrete zone. This method not only reduces calculation workload of subsequent parameter identification but also guarantees the reliability of the result of parameter identification.

2.3. Parameter Identification Method. Based on the result of parameter sensitivity analysis, in order to achieve identification of the undetermined parameters in the optimization model (see (7)), one possible method is genetic algorithm (GA). GA is a self-adapting overall optimization probability searching algorithm based on biological genetic and evolution process in the nature. Compared to traditional optimization algorithms, GA has better overall searching ability. The basic feature of GA is using overall evolution, which means to find the best solution through constant evolution of species.

The controlling condition of basic GA includes individual coding method, fitness evaluation function, initial group, group size, the selection operator, the crossover operator, the mutation operator, and termination condition of genetic algorithm.

However, there are many drawbacks in basic GA; for example, the accuracy, reliability, and calculating time cannot be satisfied simultaneously, and it is likely to encounter disadvantages such as earliness and poor local searching ability, so basic GA requires further update.

This paper made a lot of effective update to basic GA, adopting the advanced niche genetic algorithm, suspicious peak value determination strategy, and local accurate searching techniques, so that the overall searching ability of genetic algorithm is improved, which can be shown as follows.

(1) Improvement to Traditional Niche Genetic Algorithm. First, build optimal individual preservation strategy. Each niche evolves individually and saves the current optimal individual after evolution is done for each generation. When evolution of this generation is done before the evolution of each generation starts, if the optimal individual is within the group, then leave it as it is; otherwise, use the copy of current optimal individual to replace the worst individual in current generation. This method guarantees that the optimal individual will not be eliminated during the process of evolution and will speed up the converge process.

Otherwise, build data exchange mechanism among niches. Perform optimal individual exchange when each evolution is completed, meaning use the optimal individual of the first niche to replace the worst individual in the second niche. Under the premise of ensuring the diversity of the

population, this method can improve the proportion of the good individuals and speed up the convergence.

(2) *Building Suspicious Peak Value Determination Strategy.* When independent evolution of each niche is done, it will converge to a peak value. When the amount of niche is large, then all the peak values must contain all the global optimization and local optimization points. Before the final global optimization point is determined, all the obtained peak values are considered as “suspicious peak value.” The optimization point of A amount of all the suspicious peak value point must be the global optimization point, which is referred to as objective function F^* , and the corresponding variables are $\{x_1^*, x_2^*, \dots, x_m^*\}$. Set the objective function of a suspicious peak value point B as F , and the corresponding variables are $\{x_1, x_2, \dots, x_m\}$. The condition that point B is another global optimization point different from A is

$$\left| \frac{F - F^*}{F^*} \right| < \alpha \quad (11a)$$

$$d_i = \sqrt{\sum_{k=1}^n (x_k - x_k^*)^2} > \beta_i \quad (i = 1, 2, \dots, m), \quad (11b)$$

where α ($0 < \alpha < 1$) is a constant, meaning the relative searching range around the global optimization value; β_i is a constant, which is used to judge whether two points are neighboring; and d_i is the Hamming distance between two points. If $d_i \leq \beta_i$, it means that points A and B are neighboring, and they are essentially the same global optimization point with different accuracy. Equation (11a) is used to determine that B is also a global optimization point, and (11b) is used to determine that B is another global optimization point different from A .

(3) *Local Accurate Searching for All the Different Global Minimum.* Supposing the variable sets of one global optimization point are $\{x_1^*, x_2^*, \dots, x_m^*\}$ and the range of each variable is $x_{il} \leq x_i \leq x_{iu}$, the new searching range of each variable will be changed to

$$x_i \in [x_{il}, x_{iu}] \cap [x_i^* - \gamma_i, x_i^* + \gamma_i] \quad (i = 1, 2, \dots, m), \quad (12)$$

where γ_i is the searching range around the variable x_i .

Finally, the genetic evolution operation will be performed to the variables within the new searching range. Until the termination condition is satisfied, the new solution got must have higher accuracy.

The program flow diagram of advanced GA is shown in Figure 3.

3. Results and Discussion

3.1. *Example Strain Calculation.* In order to compute the strain tensors of atoms and provide evidence to confirm the method proposed in this paper to be correct and feasible by comparing with the result got by another method from the existing reference [6], the atomic mechanics model of alpha titanium material is built first. The length, width, and

thickness of the model are separately 250 Å, 100 Å, and 3 Å, and the tensile displacement load on both upper and lower surface of the model is 0.025 Å/ps, as shown in Figure 4.

The coordinate vectors of atoms in the reference configuration and in the current configuration are separately got at the time of $t = 0$ and $t = 10$ ps. Taking the center atom numbered 175 with a cutoff radius of 2 nm as an example, the number of atoms within the cutoff radius around the center atom is 146.

The weight function in [6] was assumed as

$$\omega(r) = \begin{cases} 1 - 6r^2 + 6r^3 & (r \leq 0.5) \\ 2 - 6r + 6r^2 - 2r^3 & (0.5 < r < 1.0) \\ 0 & (r \geq 1.0). \end{cases} \quad (13)$$

Then the optimal deformation gradient matrix $\hat{\mathbf{F}}$ could be got by

$$\hat{\mathbf{F}} = \mathbf{A}\mathbf{D}^{-1} \quad \mathbf{D} = \sum_n \Delta \mathbf{X}^{mn} (\Delta \mathbf{x}^{mn})^T \omega_n \quad (14)$$

$$\mathbf{A} = \sum_n \Delta \mathbf{x}^{mn} (\Delta \mathbf{x}^{mn})^T \omega_n.$$

According to (14) and (8), the optimal deformation gradient matrix and strain tensor of atom 146 at the time $t = 10$ ps got by the method in [6] were

$$\hat{\mathbf{F}}^{175} = \begin{bmatrix} 0.9972 & 0.0107 & -0.1062 \\ 0.0042 & 1.0027 & -0.0255 \\ -0.0183 & -0.0096 & 1.0671 \end{bmatrix}, \quad \mathbf{E}^{175} \quad (15)$$

$$= \begin{bmatrix} 1.1102e - 016 & -5.4210e - 020 & 0 \\ -8.1315e - 020 & 1.1102e - 016 & 0 \\ -1.7347e - 018 & -8.6736e - 019 & 1.1102e - 016 \end{bmatrix}.$$

Then the effective strain of atom 175 was $\varepsilon_{\text{eff}}^{175} = 3.3 \times 10^{-16}$.

The overall analysis method of parameter sensitivity based on the Latin Hypercube Sampling (LHS) method and Spearman rank correlation method proposed in this paper is useful to determine the range of parameters. According to the study in [8], the sensitivity of each parameter is related to its range and sampling times. Therefore, in order to balance the accuracy of each parameter, we should adjust the range of each parameter and the sampling times of all parameters to make all the parameter sensitivity values be close to each other and be less than 0.2. If a parameter sensitivity is much smaller than the sensitivities of other parameters, which means that the parameter accuracy is too high and not coordinated with the accuracy of the other parameters, then the computation quantity will be unnecessarily increased; if a parameter sensitivity is greater than 0.2, the accuracy of this parameter is insufficient.

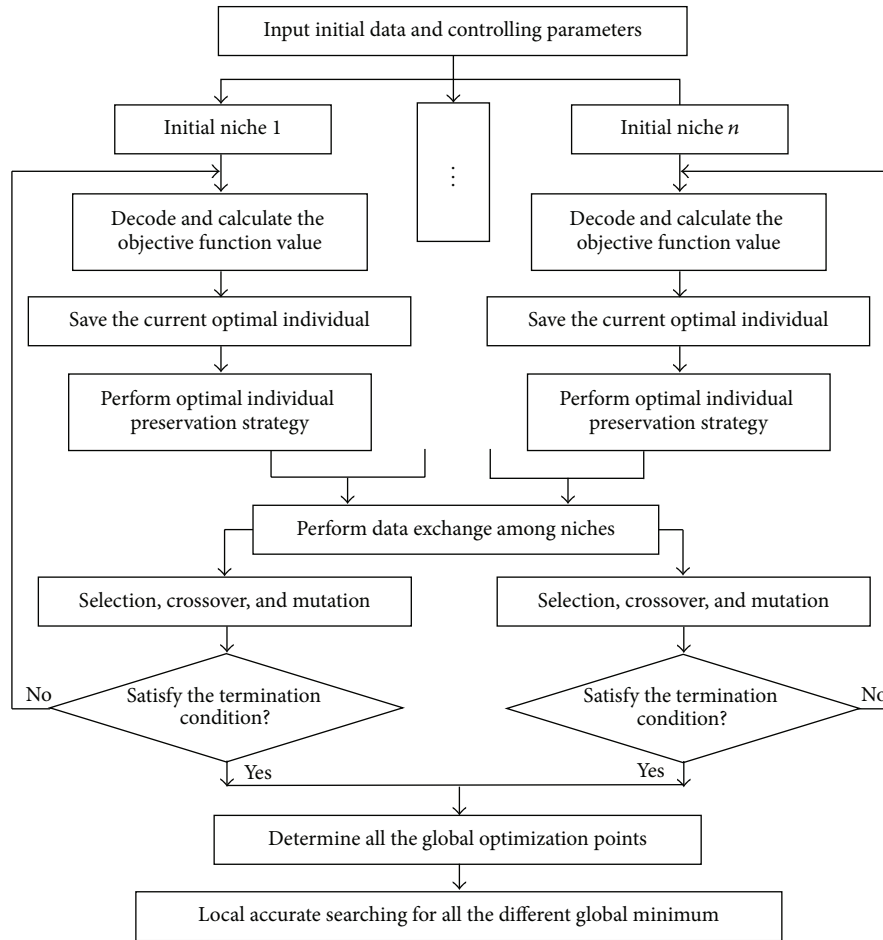


FIGURE 3: The program flow diagram of advanced GA.

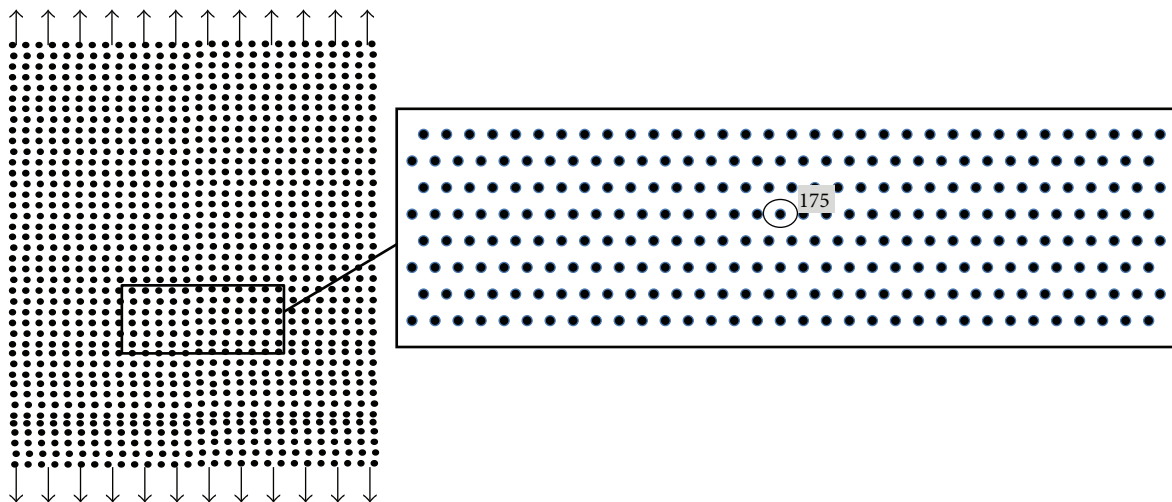


FIGURE 4: The atomic mechanics model.

Considering the parameter sensitivity of each parameter in (7), the initial searching range of each parameter is set separately as $F_{ij} \in [-10, 10]$, $k_1 \in [1.01, 100]$, and $k_2 \in [0.01, 20]$. By using the optimization method proposed in this paper with the weight function of (6), the atomic strain

nephograms at the time of $t = 10$ ps, $t = 100$ ps, and $t = 200$ ps are shown in Figure 5. In Figure 5, the red dots and blue dots separately represent the largest and smallest strain of atoms.

Figure 5 can lead to the following conclusions.

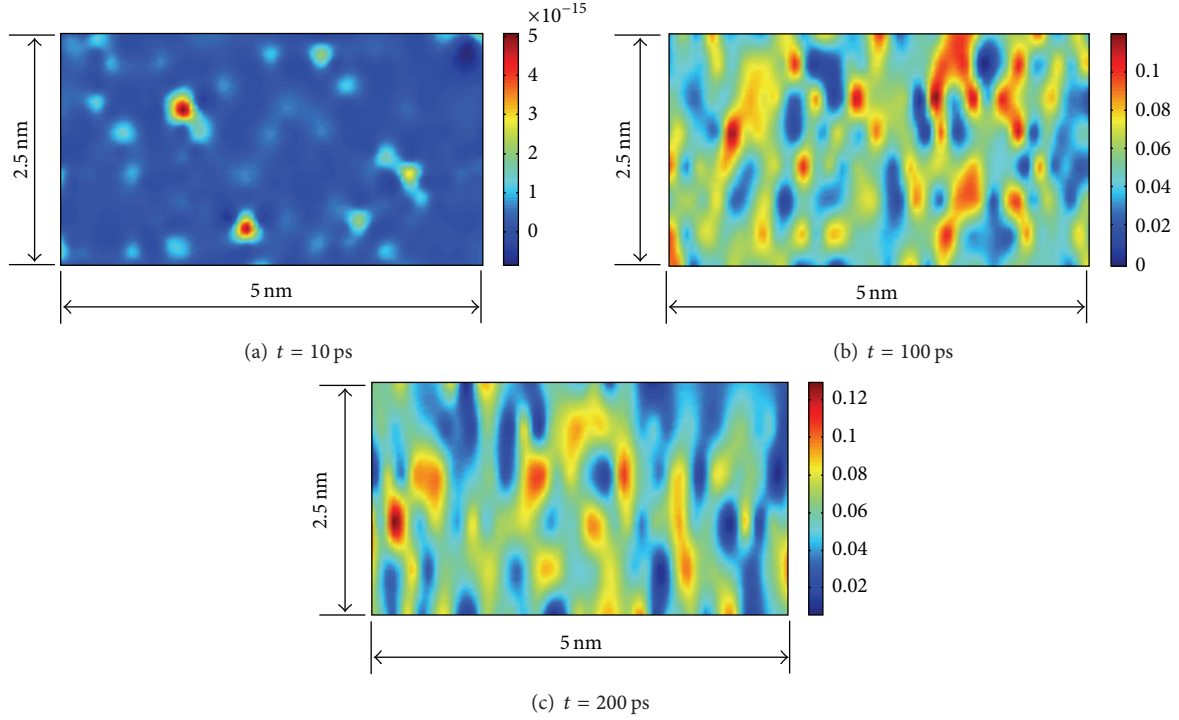


FIGURE 5: The atomic strain nephrograms.

- (1) With the increase of time, the tensile displacement load grows linearly, and the maximum strain of atoms increases. These results are in accord with the theoretical situation.
- (2) When the load is very small, only a small part of the atomic strains are relatively large, as shown in a small amount of red dots in Figure 5(a). With the increase of the load, plenty of metallic bonds break, and more and more atoms become disordered. The strains of these disordered atoms are relatively large, as shown in many red dots in Figures 5(b) and 5(c).

At the time $t = 10$ ps, the optimal deformation gradient matrix and strain tensor of atom 146 are

$$\hat{\mathbf{F}}^{175} = \begin{bmatrix} -0.9101 & -0.5269 & -0.1619 \\ 1.1913 & 1.1619 & -0.3205 \\ 0.3983 & 0.7830 & 1.9959 \end{bmatrix},$$

$$\mathbf{E}^{175} \quad (16)$$

$$= \begin{bmatrix} 0 & -5.5511e-017 & -5.5511e-017 \\ -1.6653e-016 & -5.5511e-017 & -1.1102e-016 \\ -6.9389e-017 & -2.7756e-017 & 0 \end{bmatrix}.$$

Then the effective strain of atom 175 is $\varepsilon_{\text{eff}}^{175} = 2.2 \times 10^{-16}$, and the weight function is

$$\omega_n = \frac{2 + 44.5593}{1 + 44.5593} - \frac{1}{1 + 44.5593e^{-17.9041r}}. \quad (17)$$

According to (17), the graph of weight function ω_n about the nondimensional parameter r can be got, as shown in Figure 6(a). Considering $r_{g1} \approx 0$, then the change relation of the weight function ω_n with respect to the distance R_{mn} between atom n and the center atom m can be got by (6), as shown in Figure 6(b).

According to Figure 6(b), it can be found that the values of ω_n decrease from 1.0 to 0.0 with the increase of R_{mn} . When $R_{mn} \rightarrow r_{\text{cut}}$, $\omega_n \rightarrow 0$; when $R_{mn} > r_{\text{cut}}$, $\omega_n \approx 0$. Therefore, it is very convenient to calculate the objective function $W^m(\mathbf{X})$ shown in (5) by programming without judging whether the neighbor atom n is within the cutoff radius.

3.2. Weight Function Effects on Computed Strain. The comparison of ω_n - r curves ($r_{\text{cut}} = 2$ nm) of this paper and [6] is shown in Figure 7. The form and coefficients of the weight function ω_n play a key role on the atomic strain calculation. The coefficients of the weight function should be determined by (7) and cannot be arbitrarily assumed, so it is inappropriate for [6] to use the invariant weight function (see (13)) of the artificial assumption to calculate the discrete deformation gradient at the atom. According to Figure 7, it can be found that the optimized weight function curve is almost under the artificially assumed curve, so the effective atom strain got by the optimization method proposed in this paper is smaller and more reasonable than the results got in [6].

Then the effect of cutoff radius r_{cut} on the computed atom strain will be analyzed. When the cutoff radius is changed, the effective strain of atom 175 is shown in Table 1, and

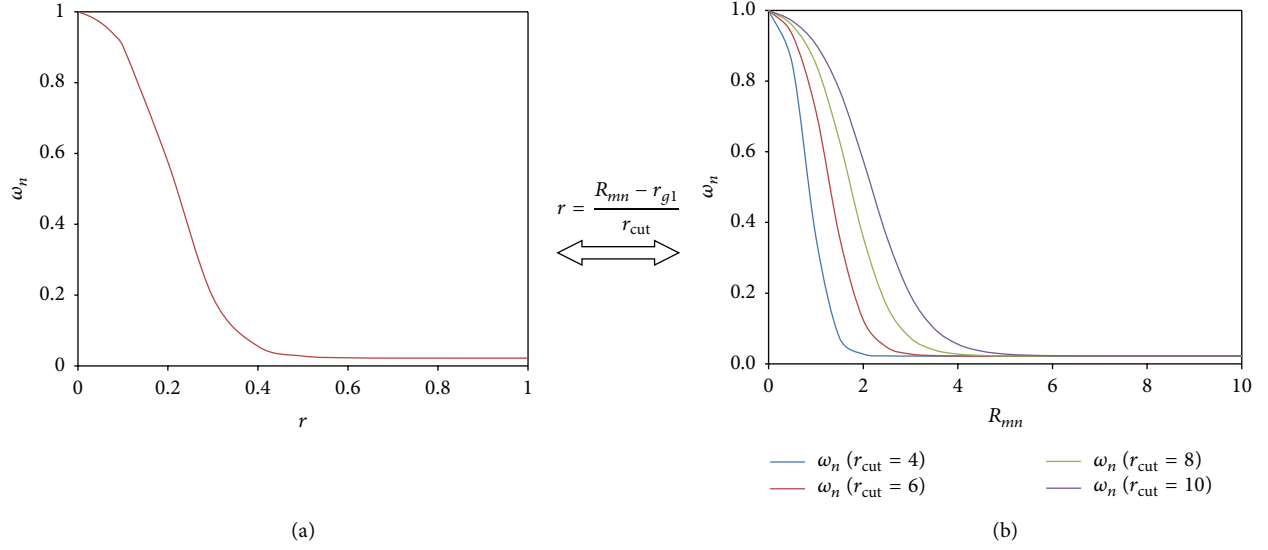
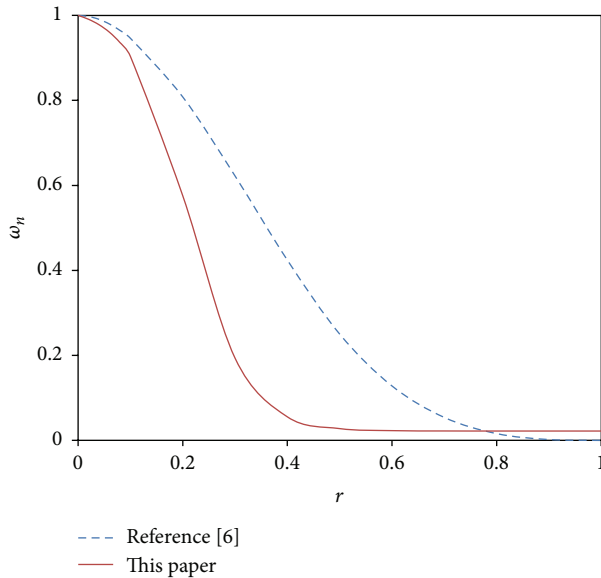
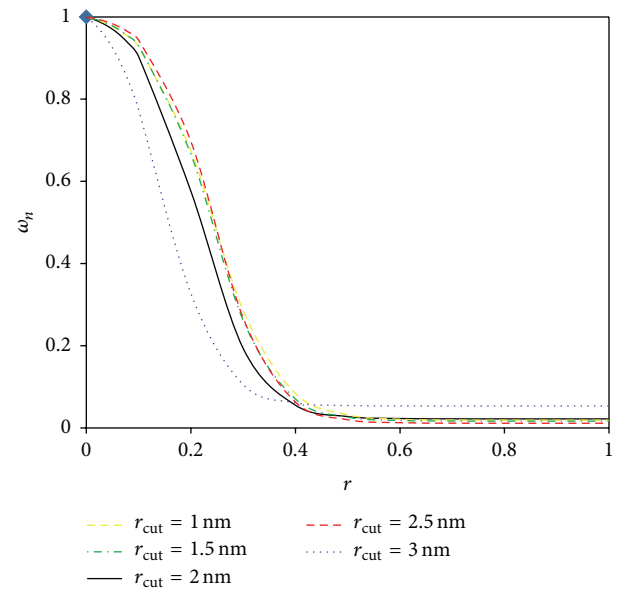
FIGURE 6: The ω_n - r and ω_n - R_{mn} curves.

TABLE 1: The effect of cutoff radius on the effective strain of atom 175 in Figure 4.

Cutoff radius	Atoms included	Effective strain of atom 175	k_1	k_2
1 nm	37	1.47×10^{-16}	51.8432	16.5200
1.5 nm	84	3.33×10^{-16}	59.9867	17.3910
2 nm	146	2.20×10^{-16}	44.5593	17.9041
2.5 nm	223	3.40×10^{-16}	87.0598	18.4370
3 nm	265	2.72×10^{-16}	17.7613	19.2712

FIGURE 7: Comparison of ω_n - r curves ($r_{\text{cut}} = 2$ nm) of this paper and [6].FIGURE 8: Comparison of ω_n - r curves for different cutoff radii r_{cut} by optimization method.

comparison of ω_n - r curves for different cutoff radii is shown in Figure 8.

According to Table 1 and Figure 8, it can be found that when the cutoff radius varies from 1 nm to 3 nm, the

optimized ω_n - r curves and effective strain of atom 175 are close to each other. When the nondimensional parameter r shown in (6) is more than 0.5, the effect of cutoff radius on the computed ω_n , or atom strain, can be almost neglected.

The cutoff radius r_{cut} was recommended to adopt the one of the potential functions.

4. Conclusions

- (1) A common measure of deformation between atomic scale simulations and the continuum framework is provided and the strain tensors for multiscale simulations are defined in this paper. In order to compute the deformation gradient of any atom m , the weight function (see (6)) is proposed to eliminate the different contributions within the neighbor atoms which have different distances to atom m , and the weighted least squares error optimization model (see (7)) is established to seek the optimal coefficients of the weight function and the optimal local deformation gradient of each atom.
- (2) This paper proposed an overall analysis method of parameter sensitivity based on the Latin Hypercube Sampling (LHS) method and Spearman rank correlation method. The sensitivity of each parameter is related to its range and sampling times. In order to balance the accuracy of each parameter, we should adjust the range of each parameter and the sampling times of all parameters to make all the parameter sensitivity values be close to each other and be less than 0.2.
- (3) The advanced genetic algorithm proposed by this paper, based on the advanced niche genetic algorithm, suspicious peak value determination strategy, and local accurate searching techniques, effectively overcomes the drawbacks of basic genetic algorithm such as earliness and poor local searching ability, significantly improves global searching ability of genetic algorithm, and makes the solving process of the optimization model (see (7)) fast, accurate, and reliable.
- (4) The form and coefficients of the weight function ω_n play a key role in the atomic strain calculation, so the coefficients of the weight function should be determined for different materials by (7) and cannot be arbitrarily assumed.
- (5) When the nondimensional parameter r shown in (6) is more than 0.5, the effect of cutoff radius on the computed ω_n , or atom strain, can be almost neglected. The cutoff radius r_{cut} was recommended to adopt the one of the potential functions.
- (6) The definition and optimization method of the atomic strain tensors for multiscale simulations proposed in this paper can be used for other nuclear power engineering materials.

Competing Interests

The authors declare that they have no competing interests.

Acknowledgments

This work was supported by the National Defense Basic Scientific Research Program of China through the Contract of B1520132013-1.

References

- [1] A. S. Oryshchenko, A. S. Kudryavtsev, V. I. Mikhailov, and V. P. Leonov, "Titanium alloys for shipbuilding and nuclear power engineering," *Inorganic Materials: Applied Research*, vol. 3, no. 6, pp. 497–506, 2012.
- [2] Y.-C. Wang, C.-Y. Wu, J. P. Chu, and P. K. Liaw, "Indentation behavior of Zr-based metallic-glass films via molecular-dynamics simulations," *Metallurgical & Materials Transactions A*, vol. 41, no. 11, pp. 3010–3017, 2010.
- [3] J. P. Hirth, J. Lothe, and T. Mura, "Theory of dislocations," *Journal of Applied Mechanics*, vol. 50, no. 2, pp. 476–477, 1983.
- [4] J. A. Zimmerman, C. L. Kelchner, P. A. Klein, J. C. Hamilton, and S. M. Foiles, "Surface step effects on nanoindentation," *Physical Review Letters*, vol. 87, no. 16, Article ID 165507, 2001.
- [5] P. H. Mott, A. S. Argon, and U. W. Suter, "The atomic strain tensor," *Journal of Computational Physics*, vol. 101, no. 1, pp. 140–150, 1992.
- [6] P. M. Gullett, M. F. Horstemeyer, M. I. Baskes, and H. Fang, "A deformation gradient tensor and strain tensors for atomistic simulations," *Modelling & Simulation in Materials Science & Engineering*, vol. 16, no. 1, Article ID 015001, pp. 599–621, 2008.
- [7] H. L. Yan and G. N. Xiao, "S-curve analysis from autoregressive regression," *Journal of Higher Correspondence Education (Natural Science)*, vol. 23, no. 5, pp. 95–96, 2010.
- [8] Y. Sheng, X. Zeng, H. Chen, and T. Han, "Identification of target parameters and experimental verification for dislocation-mechanics-based constitutive relations of titanium alloy," *Journal of Sichuan University (Engineering Science Edition)*, vol. 47, no. 6, pp. 69–76, 2015.
- [9] M. D. McKay, R. J. Beckman, and W. J. Conover, "A comparison of three methods for selecting values of input variables in the analysis of output from a computer code," *Technometrics*, vol. 21, no. 2, pp. 239–245, 1979.
- [10] C. Spearman, "The first German congress for experimental psychology," *American Journal of Psychology*, vol. 15, no. 3, pp. 447–448, 1904.
- [11] S. P. Jia, W. Z. Chen, and X. L. Li, "Parameter sensitivity analysis for seepage-stress coupling model of clay based on non-parameter statistics," *Chinese Journal of Underground Space and Engineering*, vol. 4, no. 5, pp. 830–834, 2008.

Research Article

A Comparative Study for Modeling Displacement Instabilities due to TGO Formation in TBCs of High-Temperature Components in Nuclear Power Plant

Xia Huang,¹ Jian Wang,¹ Kun Song,¹ Feng Zhang,¹ Tong Yi,¹ and Jun Ding^{1,2}

¹College of Mechanical Engineering, Chongqing University of Technology, Chongqing 400054, China

²Key Laboratory of Manufacture and Test Techniques for Automobile Parts, Ministry of Education, Chongqing 400054, China

Correspondence should be addressed to Jun Ding; dingjunawen@126.com

Received 23 March 2016; Accepted 8 May 2016

Academic Editor: Xing Chen

Copyright © 2016 Xia Huang et al. This is an open access article distributed under the Creative Commons Attribution License, which permits unrestricted use, distribution, and reproduction in any medium, provided the original work is properly cited.

This paper reports two numerical simulation methods for modeling displacement instabilities around a surface groove in a metal substrate used in nuclear power plant. The amplitude change in the groove, the downward displacement at the base node, and the groove displacement at the periphery were simulated using ABAQUS to compare the results from two methods, as well as the tangential stress in the elements at the groove base and periphery. The comparison showed that for the tangential stress two methods were in close agreement for all thermal cycles. For the amplitude change, the downward displacement, the groove displacement, and the stress distribution, the two methods were in close agreement for the first 3 to 6 thermal cycles. After that, inconsistency increased with the number of thermal cycles. It is interesting that the thermal cycle at which the discrepancy between the two methods began to occur corresponded to a thermally grown oxide (TGO) thickness of $1\ \mu\text{m}$, which showed the accuracy of the present work over the classic method. It is concluded that the present work's numerical simulation scheme worked better with a thinner TGO layer than the classic method and could overcome the limitation of TGO thickness by simulating any thickness.

1. Introduction

To advance the rapid development in nuclear energy and to meet the requirements for the future energy, ten countries across the world including Canada, France, and Japan have agreed on a framework to significantly enhance international cooperation in research for a future generation of nuclear energy systems, known as Generation IV. The Generation IV systems are intended to offer significant advances in the sustainability, safety and reliability, economics, proliferation resistance, and physical protection. The expected time for its wide application around the world sets about the year 2030 and its technology goal mainly involves sustainable energy generation with extension of nuclear fuel supply, the minimization and management of nuclear waste, the safe and reliable operation with improved accident management, competitive costs and financial risks of nuclear energy systems, and control and security of nuclear material and facilities [1]. The gas-cooled fast reactor (GFR)

system, classed as a Generation IV reactor, maximizes the usefulness of uranium resources by breeding plutonium and can contribute to minimizing both the quantity and the radiotoxicity of nuclear waste by actinide transmutation in a closed fuel cycle. The helium cooled reactor operates at an outlet temperature of 850°C and uses a direct-cycle, helium turbine for electricity (42% efficiency at 850°C) and processes heat for thermochemical production of hydrogen. Protective coatings are visualized to protect various parts of the system and also protect the system in extreme cases where the functional temperature can increase up to 1250°C and there is depressurization from 70 bar to atmospheric pressure. Such coatings must withstand high temperature, depressurization, and specific conditions of wear linked to erosion by high-speed (about 280 m/s) helium gas flow. As an alternative solution, thermal barrier coatings (TBCs) are widely employed at ultra-high-temperature metallic components of gas turbines and high-temperature gas-cooled reactors (HTGRs) in nuclear power plants. Their purpose is to

protect the metallic components from high temperatures and to significantly extend the life of the engines [2, 3] by their superior temperature, oxidation, and corrosion resistance.

Typically, a TBC system consists of four layers: a top coating (TC), thermally grown oxide (TGO), a bond coating (BC), and a metal substrate [4]. The coatings insulate components from large and prolonged heat loads by using thermally insulating materials that can sustain a large temperature difference between the load-bearing substrate alloys and the coating surface. However, three-layer TBCs without a TC [5], double-layer TBCs containing only TGO and a metal substrate [6], and double-TC layer TBCs [7] have also often been investigated to find the optimum high-temperature protection for an entire TBC system. The durability of any type of TBC is significantly influenced by the mechanical performance of the TGO layer. That layer forms as a result of a chemical reaction at high temperature between metal cations and oxygen anions located at the interface between the TC and BC layers. The TGO layer helps protect the underlying substrates from high-temperature corrosion. The main reason is that the formation of TGO (mainly of α - Al_2O_3) at elevated temperature always develops a large stress that can cause the TGO layer to be unstable against out-of-plane displacements and even induce this layer to break down, especially upon thermal cycling. This phenomenon is described as displacement instability due to TGO formation and has attracted much attention in gas turbine engine TBCs and in HTGRs, since it is often associated with spallation, buckling, and even debonding of the TC layer from the TGO interface, all common failure mechanisms for TBC systems.

The principal cause of displacement instability is TGO formation, which results in a large compressive stress (commonly 3 to 5 GPa) in the TGO layer at dwell time. Another cause is the thermal expansion misfit among constituent materials, which often develops plastic deformation in the metal substrate in the cooling and reheating phase. Such irrecoverable deformation makes tension stress at the surface groove base, finally bringing about TBC failure from spallation or buckling. Consequently, displacement instability in TGO is of great importance for investigating TBC system thermal performance because it can significantly exacerbate the compression already occurring in the TGO layer. Extensive investigations have been performed to broaden basic understanding of the displacement instabilities of TGO. A variety of research methods, including theoretical derivation, experimental observation, and numerical schemas, have been used.

Our review of the literature found that much work has been done on modeling displacement instability of nonplanar surfaces. Also researched was thermal residual stress distribution that directly results in displacement instability or failure between interfaces occurring in TBCs from multiple thermal cycles or from thermal-mechanical load cycles. Busso et al. [8] undertook a finite element study to investigate stress development within a TBC system in which particular attention was paid to the role of variables such as elastic anisotropy within the TC, interface roughness, variation in creep strength of the BC, and the volumetric strains associated with the formation of TGO. They concluded that another

important factor determining TBC stress levels was the level of elastic anisotropy of the topcoat. Han et al. [9] employed 13 finite element models to simulate the influences of different TGO thicknesses on residual stress based on unified interface morphology. In their work, TGO dynamic oxidation and the relationship between TGO thickness and thermal cycling times were taken into account, and simulation results were close to the actual situation. Yang et al. [10] developed a finite element model for a turbine blade with TBCs to investigate its failure behavior under cyclic thermal loading and found dangerous regions in the ceramic coating, as determined by the maximum principal stress criterion. Ranjbar-Far et al. [11] used a viscoelastic model in their simulation to investigate the influence of the ceramic layer and high-temperature creep characteristics of the BC layer on coating stress. They found that ceramic layer and bond layer high-temperature creep constituted a relief mechanism for coating stress. Białas [12] investigated crack development induced by residual thermal stress in TBCs using a numerical simulation scheme in which cohesive zone elements at the oxide/ceramic interface were used to model the development of interfacial microcracks. TGO layer thickening and the creep deformation of all system constituents were also modeled. They concluded that the development of the interfacial crack allows for microcrack formation within air plasma spray TBCs. Subsequent TGO growth results in a tensional zone within the oxide layer. Freborg et al. [13] developed a finite element model to evaluate the stresses induced by thermal cycling and found that the oxidation of the BC had a strong effect on ceramic layer stresses and that oxidation-induced stresses were influenced by other factors such as BC creep, TC creep, and BC roughness. Sfar et al. [14] proposed a finite element model incorporating interface cracks to simulate residual stress fields to understand the failure mechanisms. They found that the modified crack closure integral method was found to be a very efficient tool to determine the mode-dependent energy release rates for modeling TBC failure. It is worth mentioning that Karlsson and her colleagues [15–18] have performed a large amount of original work in simulating displacement instability near a surface groove on an alumina forming alloy substrate. Their research results are widely accepted by worldwide peer researchers and can be considered as classic in the field. (Their work is referred to as the classic method in this paper to distinguish it from the present work.) In their work, to explore cyclic morphological instability incurred by TBCs, they proposed a spherically symmetric fundamental model that can be solved analytically. At the same time, they developed a novel numerical method to investigate displacement instabilities for a sinusoidal undulation embedded into the BC. They also investigated distortion occurring near a single groove subjected to thermal cycling using the numerical method. They performed a series of finite element simulations revealing that TGO displacement was reduced by increasing the high-temperature strength of the underlying BC, but displacement increased with the strength of the TGO and the curvature of the groove edge.

However, their numerical simulation works well only for thinner (usually less than $1\ \mu\text{m}$) TGO layers formed at dwell

times between multiple thermal cycles. For thicker TGO layers of several microns, the simulation needs to apply a larger strain at the innermost layer of TGO elements to model TGO formation. This can result in an extremely severe deformation at the periphery of a groove, leading to a divergence solution problem in ABAQUS. Ding et al. [6, 19] developed their own procedure to simulate displacement instability in the TGO layer at the interface. They were able to model TGO growth at high temperature without the limitation of TGO thickness. Their procedure worked well even when TGO thickness attained $5\ \mu\text{m}$. However, when simulating TGO crack propagation, the procedure encountered problems due to the need to incorporate many more crack parameters. Consequently, it is necessary to develop another numerical scheme to model displacement instability for greater TGO thicknesses.

In this work, another numerical simulation procedure based on the ABAQUS UMAT (User-defined Material) subroutine was proposed to simulate TGO growth at high temperatures. This procedure would be used to investigate displacement instabilities at the periphery of a surface groove embedded in a metal substrate. To determine the correctness and effectiveness of this method in the present work, we compared two methods (the classic method and the present work). We used a series of finite element analyses for simulating the final amplitude change in the surface groove, the downward displacement at the base node of the groove, the groove displacement at the periphery, and the tangential stress distribution in the elements at the base and the periphery of the groove. The comparison showed that for tangential stress in the base elements the two methods were in close agreement for all thermal cycles. For the amplitude change, the downward displacement at the base node, the groove displacement, and the stress distribution in the elements near the groove, the two methods were more in agreement for the first 3 to 6 thermal cycles. After that, inconsistency increased with the number of thermal cycles. It is interesting that the thermal cycle at which the discrepancy between the two methods occurred corresponded to a thermally grown oxide (TGO) thickness of $1\ \mu\text{m}$, which showed the accuracy of the present work over the classic method. It is concluded that the present work's numerical simulation scheme worked better with a thinner TGO layer than the classic method and could overcome the limitation of TGO thickness by simulating any thickness.

2. Materials and Methods

2.1. Specimen Description. The specimens were rectangles of commercially available heat-resistant alloy approximately $5\ \text{mm} \times 50\ \text{mm}$ with a nominal composition of Fe 72.8%, Cr 22%, and Al 5%. The previous studies [5] stated that nonplanar interfaces (due to imperfections, voids, and material heterogeneity) more easily incur displacement instability than planar interfaces. To aid in-depth exploration of the deformation mechanism, two groups of grooves, one horizontal and the other vertical, were carved in the metal substrate surface to highlight displacement instability in experimental measurements. Each group consisted of two

parallel grooves $20 \pm 5\ \mu\text{m}$ deep and $160\ \mu\text{m}$ wide. The specimens were mounted on a microcreep tester for thermal cycling, as shown in Figure 1(a and b).

2.2. Experiment Observations. The specimens were held in equilibrium between upper and lower friction grips and surrounded by a quartz tube to shield them from turbulence. They experienced 24 thermal cycles and one typical cycle consisting of 600 sec cooling from $1,200^\circ\text{C}$ to the ambient, 600 sec reheating, and 1,800 sec holding at high temperature. Each specimen was cut into foils to expose the cross sections of the vertical and horizontal grooves and then polished again and examined by scanning electron microscopy. In Figure 1(c), the dotted line is the shape of the groove prior to the experiment. It is evident that the larger upward deformation occurred at the periphery of the groove, while the smaller deformation occurred at the base. At the same time, notice that the specimens also expanded in length during the experiment. For the purpose of description, the outward deformation at the groove periphery is called groove displacement, δ_0 , which is defined as the distance from the point at the curved section with the larger curvature of the final TGO deformation, as seen in Figure 1(d) [20].

2.3. The Classic Method to Simulate TGO Growth

2.3.1. TGO Growth Mechanism. Since the main objective in this work is to compare two different numerical simulation strategies for modeling TGO growth at high temperature, it is necessary to first understand TGO growth mechanism in this subsection. When oxidation occurs at high temperature in TBCs, Al ions coming from the substrate react chemically with O anions from air to form alumina upon thermal cycles. It follows $4\text{Al} + 3\text{O}_2 \rightarrow 2\text{Al}_2\text{O}_3$. As illustrated in Figure 2, due to the peroxidation in air, alumina has already formed first at the interface between top ceramic layer and metal substrate while it typically exists as a columnar microstructural domain (shown in Figure 2). When TBCs were dwelled at the elevated temperature, due to the thermal expansion between grain boundaries for columnar TGO, the O anions come across the gap between grain boundaries and chemically react with the Al ions resided in metal substrate. This newly generated TGO forms at the interface between preexisted TGO and metal substrate which makes TBC system thicken upon thermal cycles. At the same time, another part of O anion meets Al ion at the gaps between the internal grain boundaries to form alumina which results in an increase in TGO length. Consequently, the TGO formation at elevated temperature was simulated by the two components, namely, lateral growth strain (increasing TGO length) and thickening growth strain (increasing TGO thickness). The subsequent sections focus on how to simulate such two growth strains in numerical simulation to better reproduce the actual TGO formation at high temperature.

2.3.2. The Numerical Simulation Procedure. This section summarizes the numerical scheme to simulate TGO growth at high temperatures for TBCs experiencing multiple thermal cycles, as appeared in [6, 15–18]. We call such a numerical

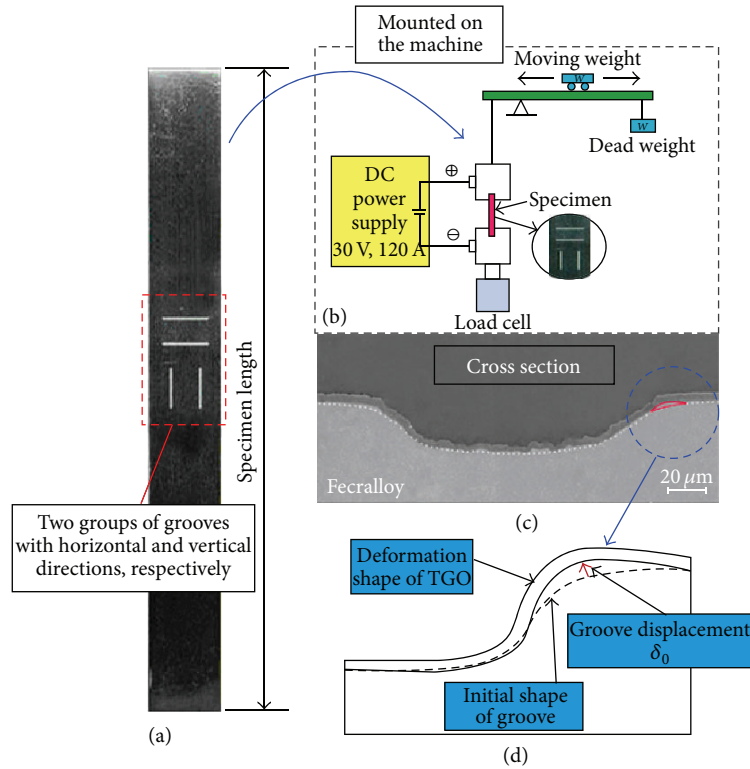


FIGURE 1: The experiment specimen geometry, test machine, and SEM for cross section showing deformation shape near groove. (a) Specimen geometry, (b) sketch for test machine, (c) SEM image for cross section, and (d) definition for the groove deformation.

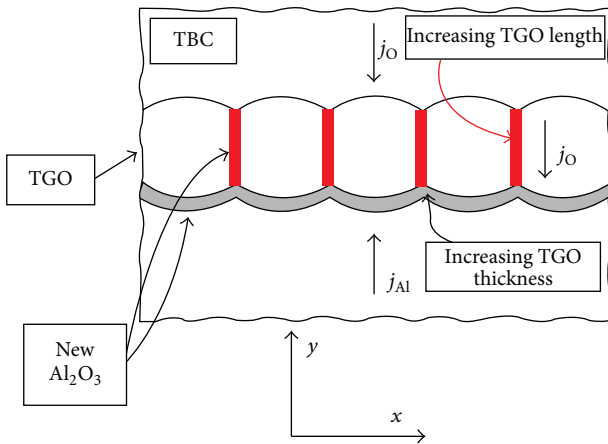


FIGURE 2: TGO growth mechanism at high temperature.

simulation method the classic method. Figure 3 illustrates the numerical simulation scheme described in those studies. A surface groove in the BC layer was employed to model a flaw or imperfection at the interface between the TGO and the BC. Three layers, including the TGO, the BC, and the metal substrate, were arranged in top-down order in constructing the finite element method (FEM) model. Considering the geometric symmetry, a symmetric boundary condition was imposed at the central axis of the specimen configuration. A periodic boundary condition was imposed to model the

random existence of imperfections in the TBC system. To keep the same displacement in x direction for the nodes located at the right side, the keyword “*Equation*” was used in the ABAQUS software to impose an x displacement on the horizontal axis, and the y displacements at the nodes at the bottom side of the metal substrate were constrained. Figure 3(b and c) show enlarged representations of the mesh configurations near the surface grooves. The initial TGO that was formed in air was first meshed into six layers of rectangular elements, with each layer having the same thickness. Consequently, the thickness of each element layer was $1/6$ that of the initial TGO thickness. For simulating TGO growth at high temperatures, a lateral growth strain and a thickening strain, were used to represent TGO formation along the lengthwise direction and along the thickness direction, respectively, with the aid of user subroutine UEXPAN in the ABAQUS software. TGO growth in the thickness direction was simulated by applying a thickening strain at the sixth layer of TGO elements. (Those were closest to the BC layer and marked as green in Figure 3(c) at each thermal cycle, not related to the other five layers of TGO elements.)

2.3.3. *TGO Growth Thickness in Simulation.* The final TGO thickness after N thermal cycles in the classic method is as follows [6]:

$$h = h_0 + h_0^e [(N - 1) \varepsilon_t], \quad (1)$$

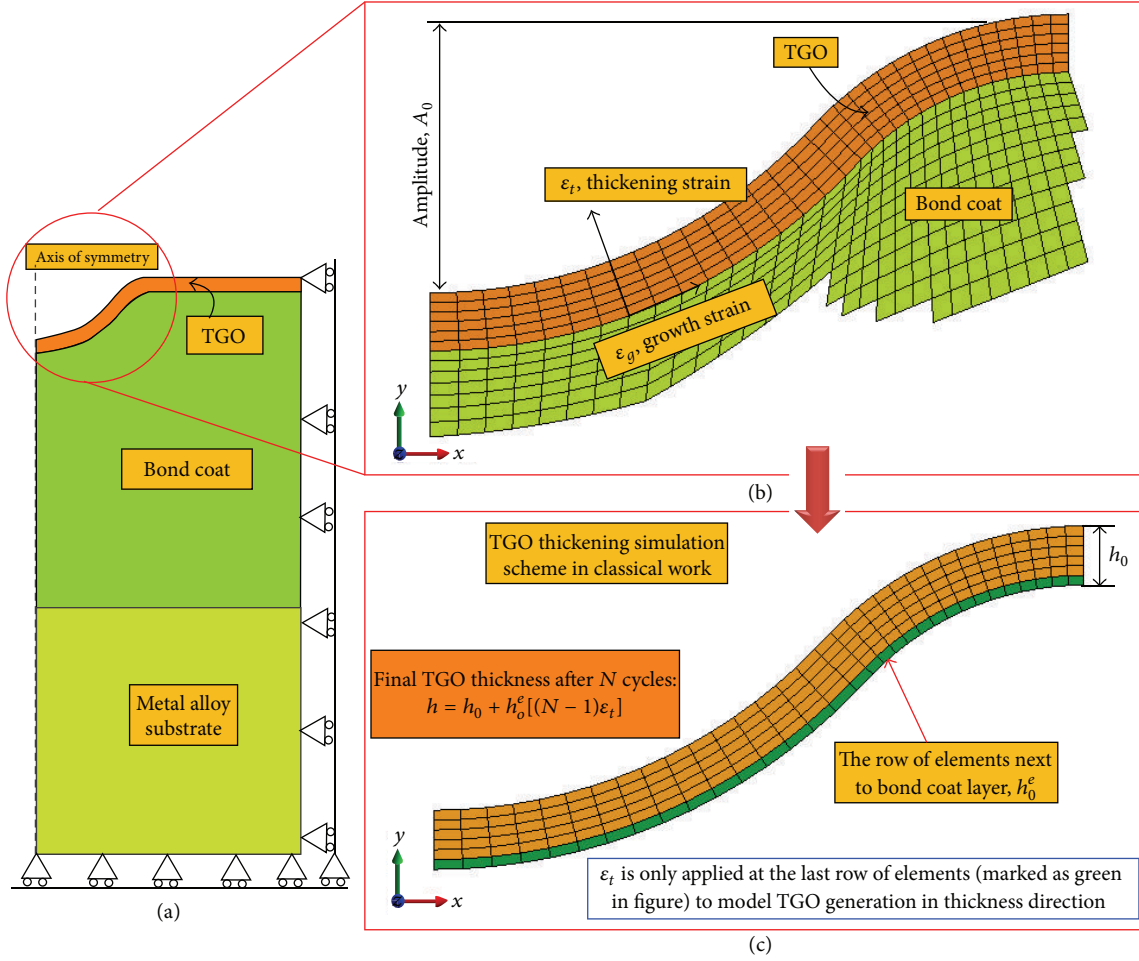


FIGURE 3: The FEM model used in the classical method. (a) The multilayer geometry model. (b) The mesh detailed in TGO layer. (c) The simulation strategy modeling TGO formation.

where h_0 is the initial TGO thickness, taken as $0.5 \mu\text{m}$ in accordance with that observed in the TBC deposition, and thus h_0^ϵ equals $1/12 \mu\text{m}$ of TGO thickness. The value for the TGO thickening strain is obtained by the following equations:

$$\beta = \frac{\epsilon_g}{\epsilon_t}, \quad 10^{-4} < \epsilon_g < 5 \times 10^{-3}, \quad (2)$$

$$\beta = 10.$$

So the final TGO thickness after 24 thermal cycles follows within the limitation

$$(0.5 + 2 \times 10^{-5}) \mu\text{m} < h < (0.5 + 1 \times 10^{-3}) \mu\text{m}. \quad (3)$$

After a simple calculation, (3) shows that the final TGO after 24 thermal cycles is very thin. The newly increased TGO thickness seems far less than the initial TGO thickness of $0.5 \mu\text{m}$. As a result, the final TGO thickness that can be simulated in the classic method cannot exceed $1 \mu\text{m}$. However, previous work [20, 21] shows that the TGO thickness observed in experiments often attains approximately 4 to $5 \mu\text{m}$. According to the theory of classic mechanics, when

simulating TGO growth with a thickness of 4 to $5 \mu\text{m}$, that is, if TGO begins from an initial thickness of $0.5 \mu\text{m}$ to 4 or $5 \mu\text{m}$, it must undergo a very large strain at a value of 7 to 9. Such a severe large deformation occurring in the TGO layer cannot be smoothly simulated in the classic method. Figure 4 shows a finite element simulation result for TGO deformation using the classic method, in which a TGO thickness of approximately $4 \mu\text{m}$ that forms during 24 thermal cycles is what we want to simulate in a finite element analysis (FEA). Figure 4(b) shows the deformation shape for only the first four thermal cycles. It was observed that the layer of thickening elements was sharply deformed. Note that the thickening layer is also the sixth layer of the TGO element, exactly the same as that in the classic FEM. The thickening layer must experience a very large deformation in only the first four thermal cycles, many times as thick as that of the undeformed layer. Because of the large deformation, the deformed layer of TGO elements after four thermal cycles was extracted, and because of the deformed configuration of TBCs we remeshed again on the sixth layer of deformed TGO elements for the simulation for the upcoming 5 to 24 thermal cycles, as shown in Figure 4(a). Under the same boundary conditions as

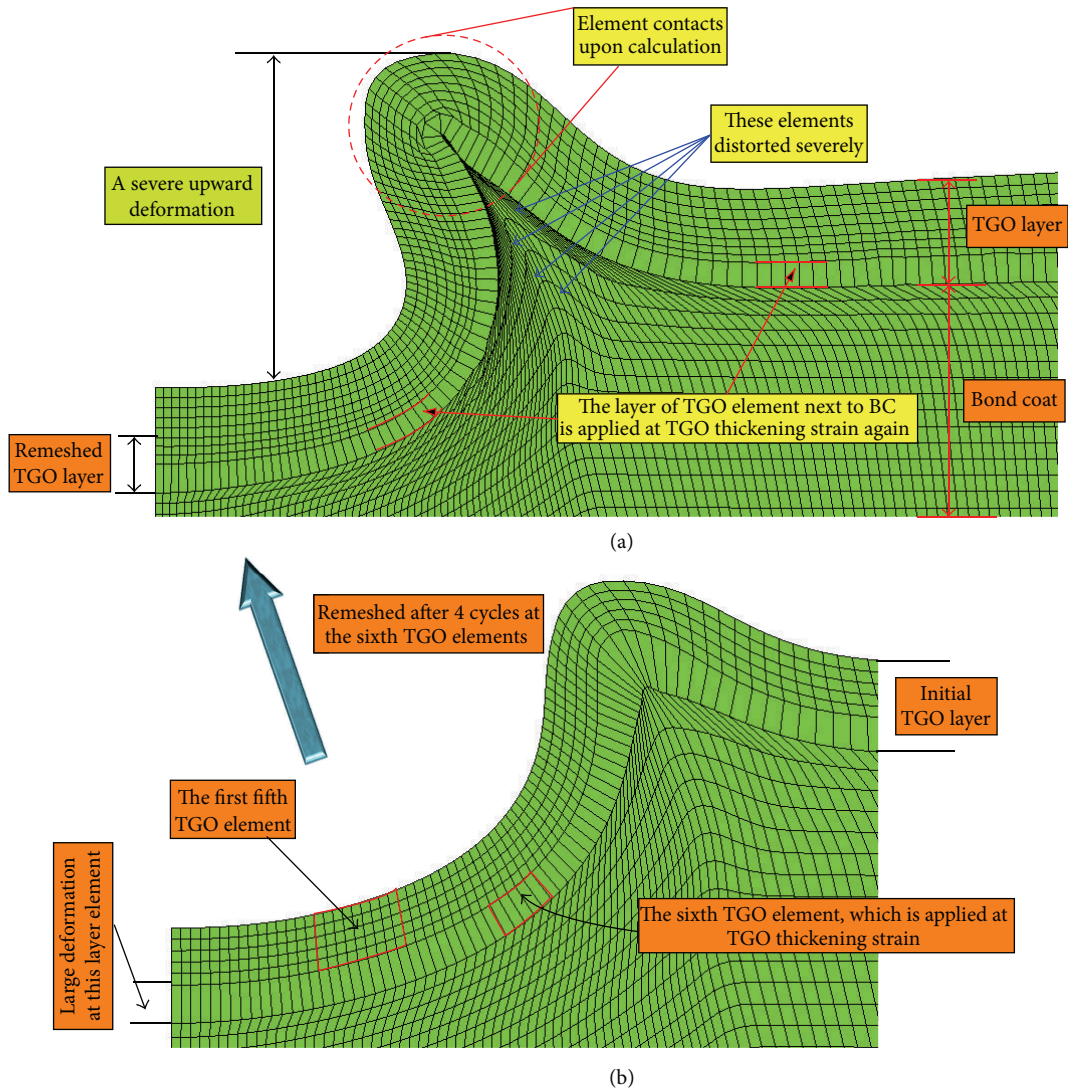


FIGURE 4: The deformation profile for the simulated FEM model. (a) The remeshed mesh configuration and (b) the deformation profile after the first four thermal cycles.

before, the remeshed FEM ran again in ABAQUS for another four thermal cycles, five to eight thermal cycles, where the TGO thickening strain was again applied at only the layer of TGO elements closest to the metal substrate layer. However, when ABAQUS ran the sixth thermal cycle, it stopped due to a very severe deformation at the periphery of the groove. The accumulated large deformation finally developed a mesh contact and even mesh penetration at that site (Figure 4(a)). Furthermore, the elements in the metal substrate next to the groove periphery were also distorted drastically. The trial and error procedure in the classic FEM was unavailable to model TGO thickening during thermal cycles for large final TGO thicknesses, although it worked very well for lesser thicknesses.

2.4. Numerical Simulation Procedure Based on UMAT

2.4.1. *Implementation Based on UMAT.* The ABAQUS UMAT software provides a robust simulation capability

to model specified material constitutive relations [22]. As an effective and flexible tool for FEA, UMAT allows the implementation of particular functions to be typically written as FORTRAN code and must be included in a model when executing an analysis. UMAT relates directly to the constitutive stress response of a material, given prescribed conditions of deformation. The user specifies a range of information to the material module relating to both the beginning and end of a time increment. In particular, stress, strain, and a deformation gradient are provided at the beginning of the time increment. Strain and the deformation gradient are also provided at the end of the increment.

Figure 5 is a flowchart for programming FORTRAN code to simulate TGO formation and material property with a high-temperature substrate metal, using UMAT. First, the TGO material properties and the metal substrate, including the elastic modulus, Poisson's ratio, and the yielding stress, are all incorporated into a UMAT subroutine. An initial calculation for strain increment $\Delta\varepsilon$ and stress increment $\Delta\sigma$

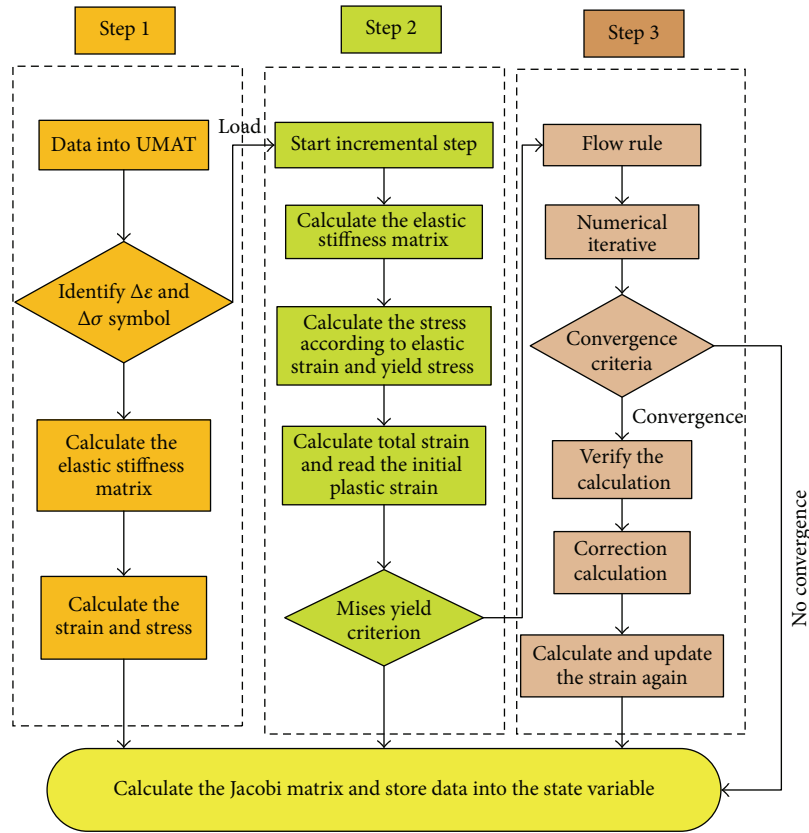


FIGURE 5: The flow chart for UMAT.

determines the sign of the two increments. Combined with the applied load condition, if the TBC is without load, UMAT directly calculates the stiffness matrix and then evaluates magnitudes of stress and strain in order to calculate the Jacobi matrix and store data into the solution state variable. However, once the load exists (in this case the thermal cycling load is considered as the applied load), it will automatically divide the load step into multiple increments and calculate the stiffness matrix, stress, and strain within each increment according to the input of constitutive relations for TGO and the substrate material. Generally, elastic deformation first develops when the material is under initial loading. As the load increases, once the stress generated in elastic deformation exceeds the yielding stress, plastic deformation occurs. Consequently, the user should prescribe the suitable yield criterion for the material. Since a TBC consists of metallic materials, the von Mises yield criterion supports the yielding behavior during multiple thermal cycles. An incorporated flow rule in the UMAT subroutine quantitatively describes the elastic-plastic deformation of the relationship. The solver can determine whether the results in each increment converge within the allowable tolerance. If so, verification and correction for the results can be validated and then used to update the strain increment iteratively over the cycle. Finally, ABAQUS calculates the Jacobi matrix and stores the data into the state variable for subsequent reads of the thermal cycling history.

2.4.2. Verification of Implementation. Based on the above-described procedures, the user subroutine for simulating TGO growth at high temperatures only at the dwell time of each thermal cycle is implemented using FORTRAN language based on the UMAT subroutine interface. Since numerical simulation for displacement instability near a surface groove for 24 thermal cycles was a difficult and complicated solving process, it was necessary for us to verify the correctness and validity of the programmed user subroutine before it was incorporated into ABAQUS for a full analysis. In this section, we focus on the verification for a single-element and a three-element simple FEA model and for elastic and elastic-plastic material properties, respectively.

Case 1 (a single element for three different material behaviors under three load steps). This case was directed at one single CAX4 element for an implicit static elastic deformation analysis using Complete ABAQUS Environment (ABAQUS/CAE) and using UMAT based on the procedure described in Section 2.4.1. Table 1 describes the material properties and the load boundary conditions used in the FEA. For the analysis using ABAQUS/CAE, the element was assigned three different material properties under a load of 100N in three running analyses. For the analysis using UMAT, the elements were assigned the same material properties and load condition as those for ABAQUS/CAE.

TABLE 1: The material property configuration and load condition for the element.

Analysis	Element	Material properties		Load (N)
		Modulus of elasticity E (Mpa)	Poisson's ratio	
1	CAX4	380E3	0.2	100
2		190E3	0.3	100
3		250E3	0.25	100

TABLE 2: The comparison between the results from ABAQUS/CAE and UMAT.

ABAQUS/CAE		UMAT		The error analysis (%)	
Displacement (mm)	Stress (MPa)	Displacement (mm)	Stress (MPa)	Displacement (mm)	Stress (MPa)
6.987E - 04	3.449E + 02	6.987E - 04	3.449E + 02	0.0000	0.000
1.324E - 03	3.584E + 02	1.314E - 03	3.580E + 02	0.7553	0.1116
1.029E - 03	3.517E + 02	1.028E - 03	3.521E + 02	0.09718	0.1137

TABLE 3: The material property definition for elements.

Analysis	Element	Element number	Material parameters		Load (N)
			Modulus of elasticity E (MPa)	Poisson's ratio	
ABAQUS/CAE and calling UMAT	CAX4	1	380E3	0.2	100
		2	190E3	0.3	
		3	250E3	0.25	

TABLE 4: The comparison for the results from ABAQUS/CAE and UMAT.

ABAQUS/CAE		Calling UMAT		The error analysis (%)	
Displacement (mm)	Stress (MPa)	Displacement (mm)	Stress (MPa)	Displacement (mm)	Stress (MPa)
2.352E - 03	2.131E + 02	2.163E - 03	2.195E + 02	8.036	3.003

Table 2 shows a comparison of displacement and stress between the results from running ABAQUS/CAE and running UMAT. It can be seen that the displacements from the two methods are identical, while the stress values show a small difference in magnitude between them. The biggest error developed in displacement and stress does not exceed 1%. As a result, the developed UMAT for this case worked very well for the latter FEA.

Case 2 (three elements, with each assigned one different material property). As a continuation to Case 1, in this case the verified mesh contained three elements, with each one assigned a different material property but with the same applied load of 100 N. Table 3 lists the details of the material properties and load boundary conditions. Two finite element analyses were performed using ABAQUS/CAE and UMAT. Table 4 shows a comparison for the calculated displacements and stress from the two calculations. It can be seen that the displacement and stress between the two calculations show larger errors than do those in Case 1. The displacement value had an error of 8% and the stress value 3%. This is mainly attributable to the element discretization, since three elements representing three different materials resulted in more serious nonlinearity than what occurred in Case 1.

Case 3 (three elements with a combination of various materials for elastic-plastic analysis). The previous two cases

aimed mainly at a linear analysis. Case 3 involves material nonlinearity including yielding stress for verifying the subsequent complicated analysis. The FEM model for this case continued to use three elements to discretize the model. Table 6 describes three cases of material properties with a combination of three different material parameters. Each detail is listed in Table 5. Each case involved a different load and could be simulated by using ABAQUS/CAE and UMAT. That is, for number 1 analysis three elements were assigned the same material property with a load of 100 N. For number 2 analysis, elements 1 and 3 were assigned the same material property while element 2 was assigned material different from that of the other elements, with a load of 200 N. For number 3 analysis, elements 1 and 2 were assigned one material model, but element 3 had a different material model with a load of 300 N.

Table 7 shows a comparison of the displacement and stress values between the ABAQUS/CAE and UMAT running ways. The comparison shows that the error in displacement between the two running methods dramatically decreased as the material definition changed and the load increased, from 13.9% down to 2.7%, while the stress value indicates a similar trend in error from 4.9% to 0.54%. Also from the contour plot for von Mises stress, plastic deformation did not occur in number 1 analysis mainly due to the smaller applied load, while the von Mises stress for number 3 exceeded the yielding

TABLE 5: The three different material models.

Material	Material parameters		
	Modulus of elasticity E (MPa)	Poisson's ratio	The yielding stress (MPa)
M1	380E3	0.2	200
M2	190E3	0.3	
M3	250E3	0.25	

TABLE 6: The combination of different materials for element.

Analysis	Element	Element number and assigned material model						Load (N)
1	CAX4	1	M1	2	M1	3	M1	100
2		1	M1	2	M2	3	M1	200
3		1	M1	2	M1	3	M3	300

TABLE 7: The comparison of results between ABAQUS/CAE and UMAT.

ABAQUS/CAE		Calling UMAT		Error analysis (%)	
Displacement (mm)	Stress (MPa)	Displacement (mm)	Stress (MPa)	Displacement (mm)	Stress (MPa)
1.573E - 03	2.015E + 02	1.793E - 03	2.115E + 02	13.986	4.963
4.241E - 03	4.253E + 02	4.533E - 03	4.305E + 02	6.885	1.223
6.409E - 03	6.260E + 02	6.584E - 03	6.294E + 02	2.731	0.543

stress of 200 MPa. The error decreased as material yielding occurred.

In summary, through the comparison of calculated displacement and stress values between two different running ways, ABAQUS/CAE and UMAT, it can be seen that the obtained results from UMAT approached those from ABAQUS/CAE, since the CAE running way has commonly been considered the correct way. Although there was a small difference between them in Case 2, such a discrepancy can be reduced substantially by using more elements to discretize the models. In addition, accuracy improved substantially with the introduction of plastic deformation in Case 3. We concluded that using UMAT to simulate TGO growth at high temperatures could enable FEM results within a very acceptable tolerance limit.

3. Results and Discussions

3.1. The Change in Amplitude of Surface Groove. Based on the previously described work, the major difference between the two methods (the classic method and the present work) is that the numerical simulation scheme was used to model TGO growth at an elevated temperature through multiple thermal cycles. It is widely accepted that the numerical simulation scheme in the classic method can work very well for smaller TGO thicknesses, usually less than $1\ \mu\text{m}$, while we found that the scheme in the present work can work well also for larger thicknesses of TGO. In this section, by comparing the change in surface groove amplitude resulting from the two different methods we found that for a thinner TGO the methods coincided. However, for a thicker TGO the present work continued to calculate but the classic method stopped calculating due to some error. As for the amplitude of a surface groove, it can be defined in terms of the distance

between the peripheries of the surface groove to the base of that, as illustrated in Figure 6.

Two finite element analyses, one based on the classic method and the other on the present work, were conducted to calculate the change in amplitude of a surface groove, where the FEMs were the same except for the numerical simulation scheme simulating TGO growth at high temperatures. Both schemes simulated morphological deformation for the vertical groove corresponding to the experimental observation, as illustrated in Figure 1(a). The FEM model consisted of 26,936 quadrilateral, first-order generalized plane strain elements, CPEG4 in ABAQUS, with the number of the elements determined after a mesh dependency check. Due to geometrical symmetry, half models were taken into account. The symmetric boundary condition was imposed on the side at $x = 0$. The periodic boundary condition was applied for those nodes located on the right side such that all those nodes had the same displacements in the x direction by allowing the same movement in the x direction. To avoid a rigid displacement of the overall system in the y direction, any node in the model was chosen to fix the displacement in the y direction. The material properties for this numerical simulation were taken similarly to our previous studies [6, 19, 20]. For the convenience of comparison, a TGO growth thickness of $1.2\ \mu\text{m}$ formed at high temperature was assumed for the two methods. Thus, for the classic method, the initial TGO thickness when constructing the FEM model was taken to be $1\ \mu\text{m}$. As required, the TGO could be divided into six layers. The thickening strain, ϵ_t , was applied to only the sixth layer of TGO element (closest to the metal substrate elements). It was taken as a value of 0.05 in each thermal cycle in line with (1). For the present work, it was hypothesized that $1.2\ \mu\text{m}$ of TGO needs to be uniformly formed within 24 thermal cycles. As a result, the thickness of TGO formed in each thermal cycle equaled $0.05\ \mu\text{m}$. That is to say, when

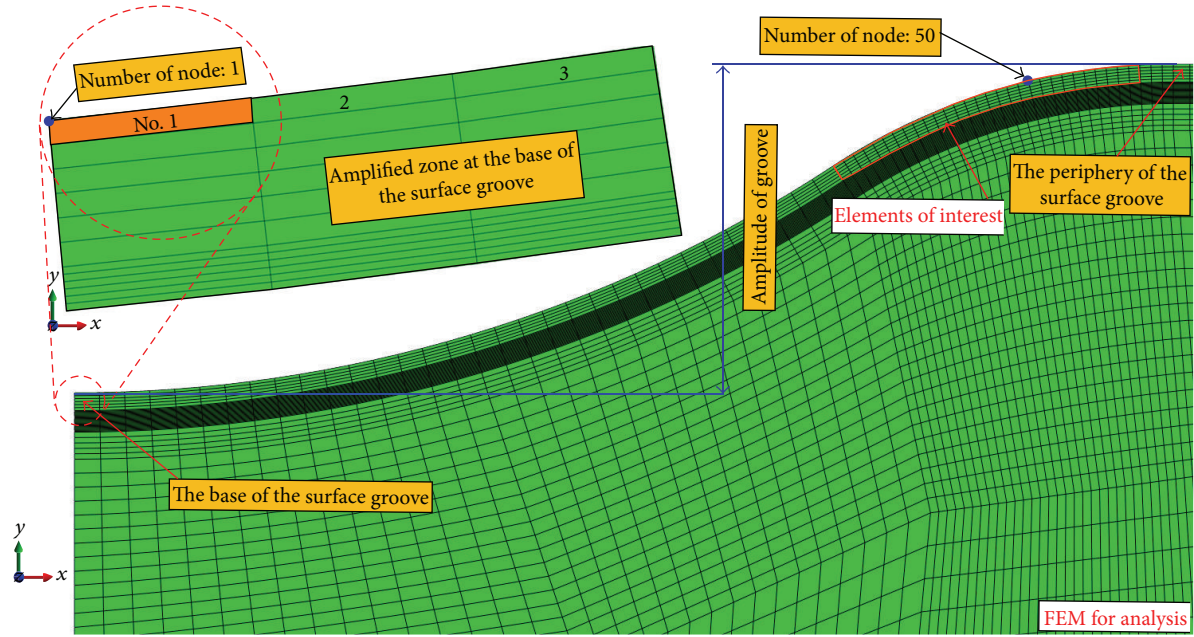


FIGURE 6: The FEM model and the detailed mesh at the base of the surface groove, as well as some reference geometry for the latter description.

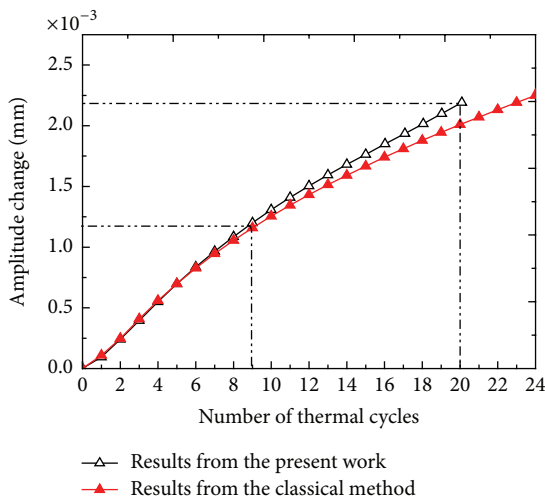


FIGURE 7: The comparison of amplitude change between two methods.

constructing the FEM model of the present work, 24 layers of elements with an equal thickness of $0.05 \mu\text{m}$ should first be meshed, and the material property for those elements at the moment should be taken the same as the metal substrate. In the first thermal cycle, the outermost layer should be transferred in material property from the metal substrate into the TGO with the aid of the ABAQUS subroutine UMAT. The procedure was repeated 24 times, finally resulting in $1.2 \mu\text{m}$ thickness of TGO formed.

Figure 7 shows the variation in amplitude change of the surface groove between the two methods with the number of thermal cycles. It can be seen that when thermal cycles 1 to 9 were run, a higher coincidence in amplitude change

between the two methods was attained, showing that the accuracy of the simulation scheme in the present work was comparable to that of the classic method. The ninth thermal cycle corresponds to a formed TGO thickness of $0.45 \mu\text{m}$, further indicating that for a thinner TGO the two methods can work very well and that the accuracy of the present work is comparable with that of the classic one. However, after the first nine thermal cycles, a difference in amplitude change between the two methods appeared slight at first and then increased significantly as the thermal cycles continued. The value of amplitude change in the present work seemed smaller than that of the classic method. This was possibly because the stress-free strain used to model TGO formation exerted a slightly greater pressure on the metal substrate to relax the higher TGO growth stress at high temperature. This may have led to a more severely plastic deformation, which was considered a requirement for displacement instability around a surface groove in the BC of TBCs. As the number of thermal cycles increased, the thickness of the newly generated TGO became greater. At the 20th thermal cycle, the FEA using the classic method stopped running in ABAQUS due to a divergence problem, while the analysis using the present method continued running until the end of the 24 thermal cycles. The 20th thermal cycle coincided with $1.0 \mu\text{m}$ of TGO thickness, which further supported the deduction, as described previously, that TGO thickness should not exceed $1.0 \mu\text{m}$ for the classic method.

3.2. Tangential Stress in the Groove Base Element. The tangential stress in the groove base element contributed greatly to the displacement instability around the surface groove, leading to a morphological change of the BC surface [20] (the metal substrate surface in this work, due to the double-layer TBC system used). Consequently, it is important to study

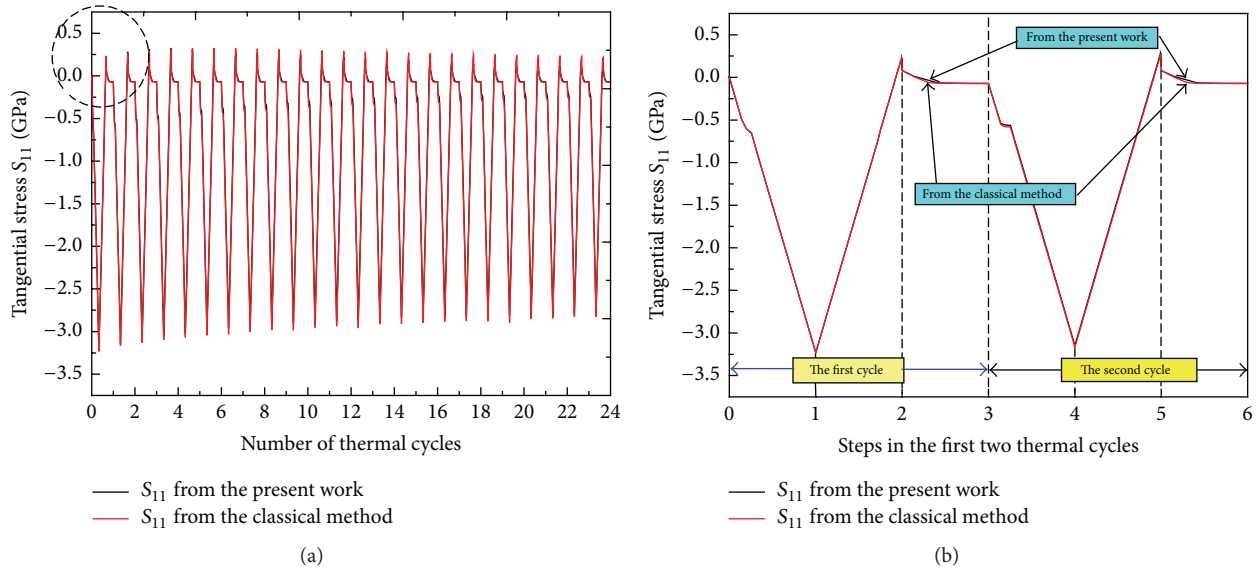


FIGURE 8: (a) The variation of the tangential stress (S_{11}) at number 1 element at the base of the surface groove against the number of thermal cycles. (b) The details for the variation of tangential stress for the first two thermal cycles.

the tangential stress to better understand the displacement instability. Figure 6 shows the element of interest in this section, labeled number 1, which was at the base of the surface groove. Both the downward displacement at the base of the groove and the substantial upward displacement at the periphery of the groove were observed in the experiment and in the numerical simulation, which was attributed to tangential stress (called “in-plane” stress in some works [15–18]). That stress increased significantly at the dwell time of a thermal cycle where TGO grew at high temperature. It is worth mentioning that the classic method cannot work for TGOs thicker than $1.0 \mu\text{m}$, which is verified in Figure 7. However, for comparison between the two methods, in this section the final TGO thickness upon 24 thermal cycles in all of the FEAs was just $1.0 \mu\text{m}$. That assured that the two methods would work well for 24 thermal cycles and enabled a valid comparison between the two methods.

Figure 8 shows the tangential stress variation in number 1 element at the base of the surface groove, with thermal cycles. Most interesting was that when the final TGO thickness was taken as $1.0 \mu\text{m}$, both FEAs worked well until the end of the 24 thermal cycles. The overall FEA results showed greater agreement between the two simulation methods, one based on a procedure using stress-free strain to model TGO formation and the other using a subroutine to calculate TGO formation cycle by cycle, for tangential stress in element number 1. This implies that the two methods were correct and maintained a higher consistency in the simulation scheme. To investigate tangential stress variation in detail, Figure 8(b) shows the amplified plot for the previous second thermal cycle (the dashed circle in Figure 8(a)). Even within each step in the first and second cycles, the tangential stresses from the two methods were still in close agreement.

Note in Figure 8(b) that the tangential stress first decreased during the thermal cycles because the temperature

also decreased from a high temperature to the ambient temperature obtained during a compression of up to 3.0 Gpa. Such a great compressive stress forced the TGO material to move downward and the metal substrate to yield. When the high temperature returned, the compression in the TGO layer relaxed significantly to an almost zero stress state. But a slight tension stress at the end of the reheating period indicated that plastic deformation developed in the metal substrate. TGO grew within the third step. The tangential stress dropped to zero first and then decreased slightly to a steady compressive stress due to TGO plasticity at the high temperature (both of them were realized by using the temperature dependent material properties, and it can be referred to in [5, 15]).

3.3. *Downward Displacement at the Base of the Groove.* Except for tangential stress in elements at the base of the surface groove, the downward displacement for the node at the groove base was also investigated for comparison between the two simulation methods. The location of node 1 is illustrated in Figure 6. The main reason for choosing node 1 was that to investigate amplitude change in a surface groove the downward displacement of node 1 must be determined. Figure 9 shows the variation of downward displacement at node 1 with the number of thermal cycles. In comparison with the higher consistency between the two methods illustrated in Figures 8(a) and 8(b), there was a significant difference between the two methods from the third thermal cycle onward. Particularly from the 15th thermal cycle, they even showed a slight contrary trend in displacement between them. In the classic method, the displacement trended upward, not downward, even reaching a positive displacement. However, for the present work the displacement at node 1 was more downward as thermal cycles continued, showing an opposite displacement direction.

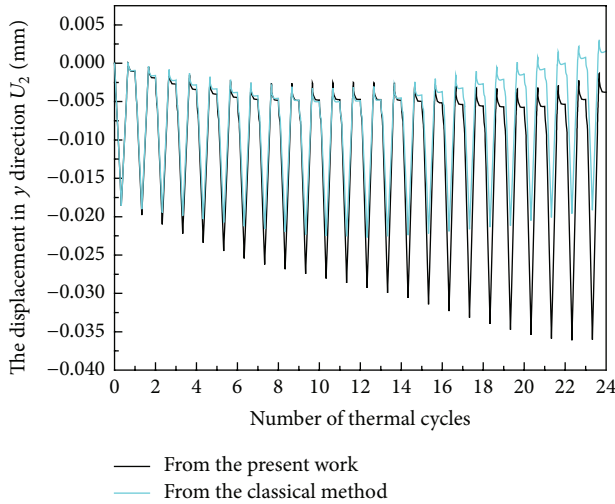


FIGURE 9: The plot of displacement in y direction for number 1 node at the base of the surface groove against the number of thermal cycles.

At the first few thermal cycles, the initial boundary condition and the applied temperature were same for both FEAs, although they used different simulation methods to simulate TGO formation at a high temperature. As also predicted by Figures 7, 8, and 9, for a thinner TGO, especially for a much thinner TGO corresponding to the first few thermal cycles, the simulation scheme was in essence similar between them. As a consequence, they showed higher consistency at the beginning of the thermal cycles. However, as thermal cycles continued, the newly generated TGO accumulated cycle by cycle and would influence mechanical performance in TBCs. In the classic method, TGO formation is simulated mainly by thickening and lengthening strains, with each thermal cycle being equal to a constant value. In that case the thickening strain was taken as 0.05 in each thermal cycle, while in the present method the newly increased TGO thickness was $0.042 \mu\text{m}$ at each thermal cycle. Furthermore, for the classic method the thickening strain was applied only at some layer of elements, usually with $1/6 \mu\text{m}$ of thickness. Obviously, the newly generated TGO thickness in each thermal cycle differed between the two methods although the final thickness was the same. TGO growth at each cycle in the present work was greater than that of the classic method. Consequently, more downward deformation was possibly produced in the present work than in the classic method due to the relatively thicker TGO thickness at the first few thermal cycles. Due to the cycle-by-cycle accumulation, a discrepancy was introduced in the downward displacement between the two methods, as shown in Figure 9.

3.4. Groove Displacement at the Periphery of the Surface Groove. The previous experiment observations illustrate that the specimen made of FeCrAlloy showed a significant change in groove profile after 24 thermal cycles as “pile-up” of the alloy at the periphery of the surface groove developed [5]. Our previous research [20] showed a similar deformation profile

at the groove periphery, although the displacement at the base of the groove seemed smaller. Therefore, deformation occurring at the groove periphery is very important in studying depth displacement instability. To illustrate the extent of deformation around the surface groove, Figure 1(d) explicitly represents it by using groove displacement, which is defined as the distance measured from the displaced location of the most outward node (node 50 marked in Figure 6) to the original position of that node [20]. Accordingly, the elements surrounding that node and consisting of the groove periphery were considered of interest.

Figure 10 shows the final resultant displacement, equal to the groove displacement, against the number of thermal cycles. Figure 10(b) is the amplification plot for the area of Figure 10(a), surrounded by a dotted line, corresponding to the 7th to 12th thermal cycles. As shown in Figure 10, analogous to the previous analysis, in the first eight thermal cycles the groove displacement for node 50 for two methods shows good agreement, much earlier than Figure 9, of three thermal cycles. However, after eight thermal cycles, a greater and greater difference between them appears in the plot. Unlike what is mentioned in Section 3.3, the discrepancy was still small even at the end of the 24 thermal cycles. The detailed plot, as illustrated in Figure 10(b), shows that during 7 to 12 thermal cycles there remained a small difference between them. The result from the classic method seems slightly larger than that from the previous analysis.

Similarly, for the first few thermal cycles, due to the same boundary condition applied and the relatively thinner TGO, both FEM methods showed a minor difference in groove displacement. As described in Section 3.3, for the present work a thicker TGO than that in the previous method was employed to conduct an FEA. The occurrence of displacement instability around the surface groove could be attributed to plastic deformation in the metal substrate and the TGO layer following the conservation of overall volume. In Section 3.3, we stated that for the present work a greater downward displacement happened at the base of the surface groove. The TGO relaxed its higher compression by displacing the node at the base in a downward movement. Consequently, the elastic strain energy stored in the TGO for the present work seemed less than that for the classic method. As a result, in the area around the periphery of the groove there was less potential for the present work than the classic method to release the stored strain energy by displacing outward at the periphery, manifested as a groove displacement. That is the reason that the groove displacement for the present work was less than that for the classic method.

3.5. Stress Distribution at the Periphery of the Groove. The driving force to enhance the outward deformation around the periphery of the surface groove cycle by cycle was the stress generated in the TGO that originated from both a thermal expansion misfit between different constituent materials and TGO growth stress during TBC dwell time at the high temperature. The tangential stress generated in TGO elements around the surface groove contributed the most to the outward deformation at this site. Figure 11 shows the

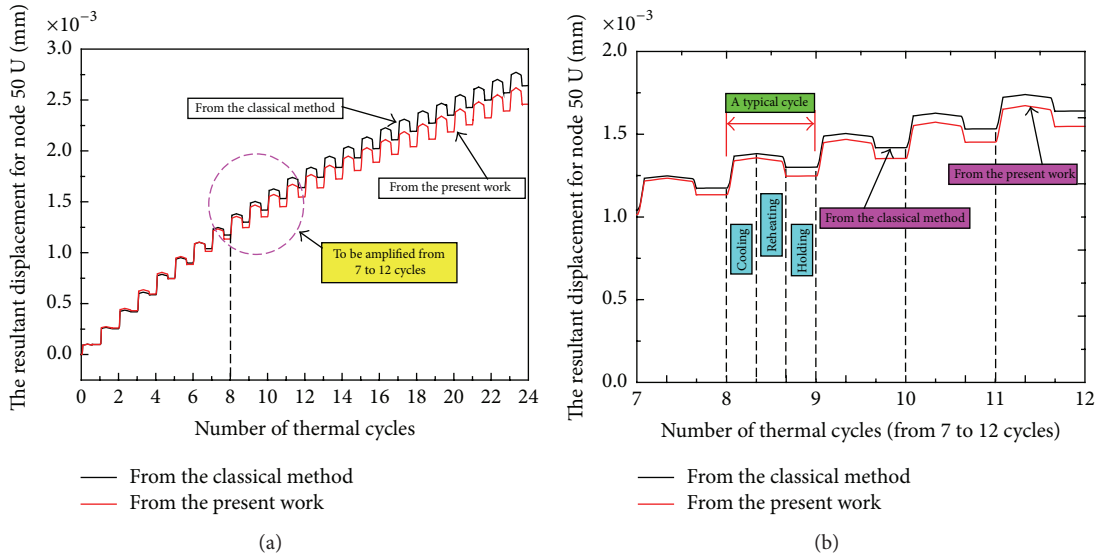


FIGURE 10: (a) The plot of the resultant displacement toward the outside direction for number 50 node which is located at the periphery of surface groove. (b) The details for the resultant displacement of number 50 node over 7 to 12 thermal cycles.

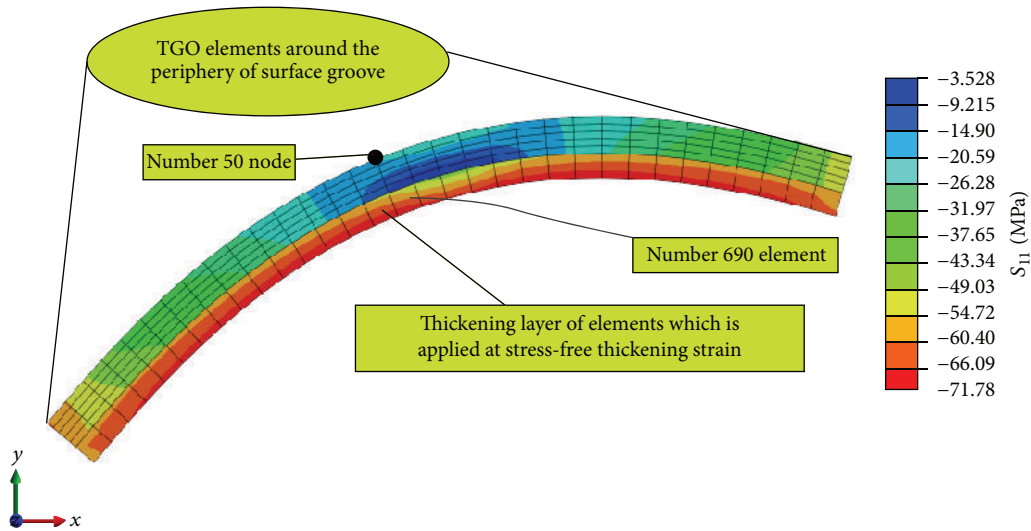
contour plot for tangential stress at TGO elements located at the periphery of the surface groove. Actually, tangential stress generated in these TGO elements was aligned with the circumferential direction of the groove, which dominated expansion of the circular section (as in Figure 11), further resulting in the occurrence of displacement instability of the surface groove.

From the comparison, we can see that the tangential stress distribution for the present work appeared more uniform than for the classic method. It can be seen from Figure 11(a) that the greatest tangential stress was distributed primarily along the innermost layer of elements, which is just applied in the thickening strain at each thermal cycle. While at the middle part of the curved section, the biggest stress value (in tension) was at the outside of the TGO growth layer, corresponding to the projection of node 50 on the thickening layer of TGO elements. In the classic method, TGO growth was realized by applying a stress-free thickening strain at only the sixth layer of elements (the red layer elements in Figure 11(a)). When ABAQUS started running, the thickening strain was suddenly applied as an insert, which possibly caused the stress fluctuation and a nonuniform distribution around the periphery of the surface groove. However, as for the specific stress values, they were almost the same: 71.78 Mpa for the classic method and 68.69 Mpa for the present work, both in compression. The tolerance in stress value lay within acceptable limit. For the present work, as depicted in Figure 11(b), the stress values over the overall TGO elements showed a smooth transition, almost without a stress gradient, in that TGO growth was modeled by linearly transforming metal substrate material to TGO material property over the cycles. From the numerical simulation itself, the result for tangential stress for the present work seemed better than that from the present method.

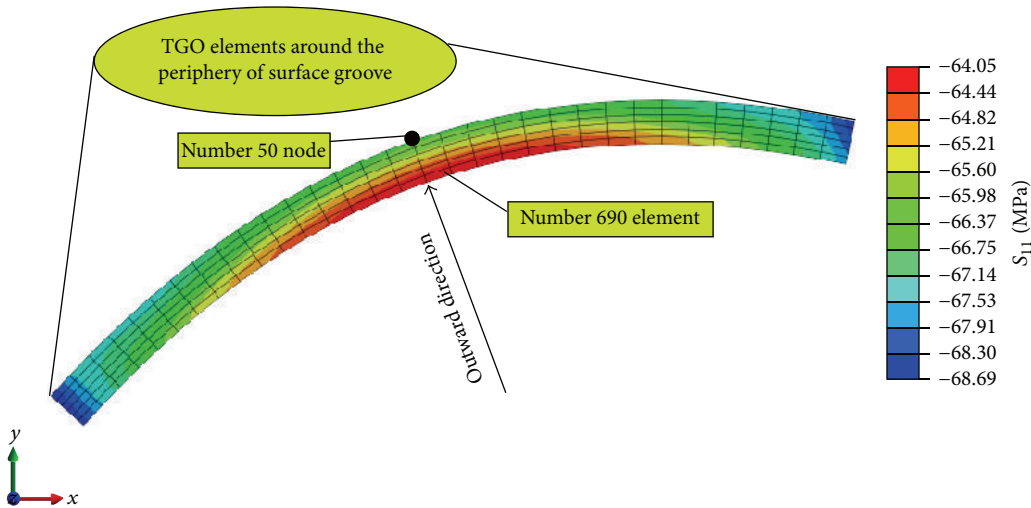
Figure 12 shows the stress variation for element 690, located at the inner side of the curve section, with the number

of thermal cycles. The stress state for the element upon 24 thermal cycles occurred in compression, with almost no stress in tension, satisfying the demand for the occurrence of displacement instability at the periphery of the surface groove. Figure 12 also shows a higher consistency in tangential stress for element 690 between the two methods in the first four thermal cycles. The possible reason for that should be the same as that previously described. However, after the fourth thermal cycle the comparison between them showed a difference in the maximum compressive stress value, and the discrepancy increased with the increasing number of thermal cycles. It is interesting that for a total of 24 thermal cycles the stress values in TGO growth (sometimes slightly in tension) were similar for the two methods. In one thermal cycle, the tangential stress always experienced three phases: compression, relaxation of compression, and constant values. These periods synchronized with the three steps of one thermal cycle. Although the two methods used different methods to simulate TGO growth at high temperatures in FEA, the consistency in stress state at TGO growth indicates that the methods were consistent, further implying the correctness of the present work. The greater and greater discrepancy in the compressive stress state, however, can be attributed primarily to the volume change induced by the newly generated TGO in each thermal cycle.

Figure 11 shows the volume change between them. The element at the sixth layer of the TGO element (counted from the outward to the inward direction) for the classic method is much thicker than that for the present work. This is because the sixth layer of TGO elements in the classic method expressed the overall TGO growth at high temperature, while for the present work the newly formed TGO upon 24 thermal cycles is not displaced in Figure 11. Actually, the final deformed TGO profile in the present work seems much thicker than that for the classic method. Notice that the final TGO thickness resulted not only from



(a) The tangential stress distribution in TGO layer from FEA using the classical method



(b) The tangential stress distribution in TGO layer from FEA in the present work

FIGURE 11: The tangential stress distribution in TGO layer around the periphery of the surface groove. (a) The result from the classical method and (b) the result from the present work.

TGO growth at high temperature but also from other strains including elastic strain, thermal expansion, and creep strains. Even in a single FEA, final TGO thickness became greater and less uniform as the lengthening strain increased [5]. Accordingly, the different final TGO thicknesses contributed to the discrepancy in compression stress value between the two methods. For the present work, the variation in thickness of TGO formed between any two thermal cycles was greater than that for the classic method. The large volume change induced by TGO formation can affect a greater compressive stress state.

4. Conclusions

A comparison in this work between two different methods, the classic method and the present work, was made for the final amplitude change in a surface groove, the downward displacement at the base node of the groove, the groove

displacement at the periphery, and the tangential stress distribution in the elements located at the base and at the periphery of the groove. The following conclusions can be drawn:

- (1) A comparison of the final amplitude change of a surface groove derived from the two methods showed greater consistency in the first nine thermal cycles. The discrepancy between the methods increased as the number of thermal cycles increased. The classic method stopped running at the 20th thermal cycle, at which TGO thickness was close to $1\mu\text{m}$, which indicated the correctness of the present work.
- (2) In a comparison made of the downward displacement at the base of the groove, the tangential stress in elements at the base and the periphery, and the groove displacement at the periphery, both methods had similar results in the first few thermal cycles.

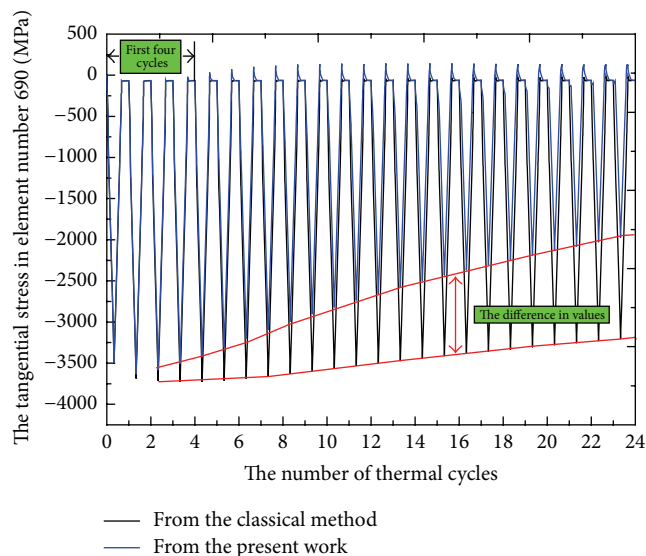


FIGURE 12: The variation of tangential stress over number 690 element against number of thermal cycles.

This demonstrated that the methods were similar in essence, although they each had a different numerical simulation scheme to model TGO growth at high temperature.

- (3) A comparison was made of different mechanical behaviors that have some effect on the displacement instability around a surface groove. The result showed that the numerical simulation scheme in the present work worked very well for a thinner TGO in comparison with the classic method but also overcame the limitation of TGO thickness and was able to simulate any TGO thickness.

Competing Interests

The authors declare no competing interests.

Acknowledgments

This work is financially supported by the Natural Science Foundation of China (11302272) and by NSAF (Grant no. U1530140).

References

- [1] GIF, *A Technology Roadmap for Generation IV Nuclear Energy Systems*, US DOE Nuclear Energy Research Advisory Committee and the Generation IV International Forum, 2012.
- [2] G. Mauer and R. Vaben, "Technology vision: current developments and challenges in thermal barrier coatings," *Surface Engineering*, vol. 27, no. 7, pp. 477–479, 2011.
- [3] V. Kumar and K. Balasubramanian, "Progress update on failure mechanisms of advanced thermal barrier coatings: a review," *Progress in Organic Coatings*, vol. 90, pp. 54–82, 2016.
- [4] A. G. Evans, D. R. Mumm, J. W. Hutchinson, G. H. Meier, and F. S. Pettit, "Mechanisms controlling the durability of thermal barrier coatings," *Progress in Materials Science*, vol. 46, no. 5, pp. 505–553, 2001.
- [5] A. M. Karlsson, J. W. Hutchinson, and A. G. Evans, "A fundamental model of cyclic instabilities in thermal barrier systems," *Journal of the Mechanics and Physics of Solids*, vol. 50, no. 8, pp. 1565–1589, 2002.
- [6] J. Ding, F.-X. Li, and K.-J. Kang, "Numerical simulation of displacement instabilities of surface grooves on an alumina forming alloy during thermal cycling oxidation," *Journal of Mechanical Science and Technology*, vol. 23, no. 8, pp. 2308–2319, 2009.
- [7] L. C. Su, W. X. Zhang, Y. L. Sun, and T. J. Wang, "Effect of TGO creep on top-coat cracking induced by cyclic displacement instability in a thermal barrier coating system," *Surface and Coatings Technology*, vol. 254, pp. 410–417, 2014.
- [8] E. P. Busso, Z. Q. Qian, M. P. Taylor, and H. E. Evans, "Effects of breakaway oxidation on local stresses in thermal barrier coatings," *Acta Materialia*, vol. 38, no. 6, pp. 1–4, 2009.
- [9] Z. Y. Han, H. Zhang, and Z. P. Wang, "Numerical simulation of TBCs residual stress by the growth of TGO on typical interface morphology," *China Welding*, vol. 21, pp. 64–68, 2012.
- [10] L. Yang, Q. X. Liu, Y. C. Zhou, W. G. Mao, and C. Lu, "Finite element simulation on thermal fatigue of a turbine blade with thermal barrier coatings," *Journal of Materials Science and Technology*, vol. 30, no. 4, pp. 371–380, 2014.
- [11] M. Ranjbar-Far, J. Absi, G. Mariaux, and F. Dubois, "Simulation of the effect of material properties and interface roughness on the stress distribution in thermal barrier coatings using finite element method," *Materials and Design*, vol. 31, no. 2, pp. 772–781, 2010.
- [12] M. Białas, "Finite element analysis of stress distribution in thermal barrier coatings," *Surface and Coatings Technology*, vol. 202, no. 24, pp. 6002–6010, 2008.
- [13] A. M. Freborg, B. L. Ferguson, W. J. Brindley, and G. J. Petrus, "Modeling oxidation induced stresses in thermal barrier coatings," *Materials Science and Engineering A*, vol. 245, no. 2, pp. 182–190, 1998.
- [14] K. Sfar, J. Aktaa, and D. Munz, "Numerical investigation of residual stress fields and crack behavior in TBC systems," *Materials Science and Engineering A*, vol. 333, no. 1-2, pp. 351–360, 2002.
- [15] A. M. Karlsson and A. G. Evans, "A numerical model for the cyclic instability of thermally grown oxides in thermal barrier systems," *Acta Materialia*, vol. 49, no. 10, pp. 1793–1804, 2001.
- [16] A. M. Karlsson, J. W. Hutchinson, and A. G. Evans, "The displacement of the thermally grown oxide in thermal barrier systems upon temperature cycling," *Materials Science and Engineering A*, vol. 351, no. 1-2, pp. 244–257, 2003.
- [17] A. M. Karlsson, C. G. Levi, and A. G. Evans, "A model study of displacement instabilities during cyclic oxidation," *Acta Materialia*, vol. 50, no. 6, pp. 1263–1273, 2002.
- [18] J. Shi, A. M. Karlsson, B. Baufeld, and M. Bartsch, "Evolution of surface morphology of thermo-mechanically cycled NiCoCrAlY bond coats," *Materials Science and Engineering A*, vol. 434, no. 1-2, pp. 39–52, 2006.
- [19] J. Ding, F.-X. Li, and K.-J. Kang, "Effects of material creep on displacement instability in a surface groove under thermo-mechanical cycling," *Surface and Coatings Technology*, vol. 204, no. 1-2, pp. 157–164, 2009.
- [20] F.-X. Li, J. Ding, and K.-J. Kang, "Morphological change occurring near a surface groove on an alumina-forming alloy

subjected to thermal and mechanical cycling,” *Surface & Coatings Technology*, vol. 204, no. 9-10, pp. 1461–1468, 2010.

- [21] G. D. Ko, *Thermally grown oxides formed on superalloy surfaces and their mechanical properties at high temperature [M.S. thesis]*, Chonnam National University, 2007.
- [22] ABAQUS version 6.10, User Documentation, Dassault Systemes, 2010.

Research Article

Effect of Chemical Corrosion on the Mechanical Characteristics of Parent Rocks for Nuclear Waste Storage

Tielin Han,^{1,2} Junping Shi,^{2,3} Yunsheng Chen,^{1,2} and Zhihui Li^{2,3}

¹Institute of Water Resources and Hydroelectric Engineering, Xi'an University of Technology, Xi'an 710048, China

²School of Civil Engineering and Architecture, Xi'an University of Technology, Xi'an 710048, China

³State Key Laboratory Base of Ecohydraulic Engineering in Arid Area, Xi'an University of Technology, Xi'an 710048, China

Correspondence should be addressed to Junping Shi; shijp@xaut.edu.cn

Received 29 March 2016; Accepted 16 May 2016

Academic Editor: Xing Chen

Copyright © 2016 Tielin Han et al. This is an open access article distributed under the Creative Commons Attribution License, which permits unrestricted use, distribution, and reproduction in any medium, provided the original work is properly cited.

Long-term immersion was adopted to explore the damage deterioration and mechanical properties of granite under different chemical solutions. Here, granite was selected as the candidate of parent rocks for nuclear waste storage. The physical and mechanical properties of variation regularity immersed in various chemical solutions were analyzed. Meanwhile, the damage variable based on the variation in porosity was used in the quantitative analysis of chemical damage deterioration degree. Experimental results show that granite has a significant weakening tendency after chemical corrosion. The fracture toughness K_{IC} , splitting tensile strength, and compressive strength all demonstrate the same deteriorating trend with chemical corrosion time. However, a difference exists in the deterioration degree of the mechanical parameters; that is, the deterioration degree of fracture toughness K_{IC} is the greatest followed by those of splitting tensile strength and compressive strength, which are relatively smaller. Strong acid solutions may aggravate chemical damage deterioration in granite. By contrast, strong alkaline solutions have a certain inhibiting effect on chemical damage deterioration. The chemical solutions that feature various compositions may have different effects on chemical damage degree; that is, SO_4^{2-} ions have a greater effect on the chemical damage in granite than HCO_3^- ions.

1. Introduction

With the rapid development of industrialization, environmental problems have become worse since the 1970s. As a result, environmental geotechnical engineering research has become one of the important research topics in this field. Studying the physical and mechanical properties of rocks provides a scientific basis for the design and operation of measures to safely assess a permanent geological storage library of nuclear wastes under the corrosion of chemical solutions.

The construction of the nuclear waste disposal repository is a lengthy, arduous, and complex strategic task. Therefore, national governments have invested huge manpower, material, and financial resources for research. In addition, the governments selected rocks with different lithology as natural barriers for nuclear waste disposal repositories owing to the differences in geological conditions found in each country. Various geological rock masses have distinct physical and

mechanical properties. Granite is widely distributed and is basically characterized by its stable performance. Thus, it is often selected for the underground disposal laboratory by many countries.

Rock mass, which is distributed in repositories of nuclear waste disposal plants, is often affected by the temperature field, stress field, seepage field, groundwater, and so forth; in studying, these researchers need to consider the coupling effect on thermohydrological, hydromechanical (HM), thermomechanical, and thermohydromechanical (THM) couplings [1–3]. Many international scholars have launched a series of studies [4–9]. For example, Millard et al. [4] adopted numerical simulation to analyze the surrounding rock of a near field repository of nuclear waste disposal based on THM and found that although temperature is almost not influenced by the THM coupling, stress is greatly affected. Blum et al. [5] used “Udec” to examine the coupling properties of HM of the far field repository of nuclear waste disposal in the fractured rock mass. Meanwhile, Zhang [6] employed

their own development program and adopted the coupling model of THM to analyze the FEBEX in situ test from the two-dimensional finite element. Their results show that the physical and mechanical properties of the rock mass surrounding the disposal are influenced by stress, seepage, and temperature fields.

During the service life of rock engineering projects, the influence of the surrounding hydrochemical environment is nonnegligible, along with that of the external load. The influence of the hydrochemical environment on the mechanics of rocks has been intensively studied in recent years, and several accomplishments have been achieved. Atkinson [7, 8], Martin [9], Charles [10], and Freiman [11] all studied the influence of different chemical solutions on the crack tip of the Si-O bond. Lawn et al. [12] systematically studied the chemical function of stress corrosion on the surface and reported the extension of the K_{Ic} critical crack by the stress corrosion. Atkinson and Meredith [13] investigated the influence of different aqueous chemical solutions on the strength and crack propagation rate of quartz and found that higher concentrations of OH^- ion result in a faster expansion rate of the quartz fracture; meanwhile, the flow solution has a certain control effect on the crack growth rate. Kirby [14] studied the effect of chemical solutions on rocks from the interaction of water, rock, and humidity; the influence of chemical corrosion; and the time effect of chemical corrosion and water pressure. Bulau et al. [15–18] studied the effect of water-rock dissolution on the crack propagation of rocks. Lajtai et al. [19] analyzed and discussed the influence of water on the mechanical features and failure of granite. Dunning et al. [20] explored the effect of chemical environment on the toughness value and crack propagation rate of rock fractures. Ning et al. [21] established a chemical damage strength model for acid solutions based on the corrosive effect of different acid solutions on the cementing materials of sandstones.

General nuclear wastes, which are buried deep in the 500–1000 m geological body from the surface, are isolated from the human survival environment and are permanently hidden through a multiple barrier system. The stress field of surrounding rocks greatly changes after excavation, which intensifies the degree of internal damage in the surrounding rock mass near the field geological repository. Microcracks, crevices, and flaws of different orders are inevitably scattered inside rocks as various types of natural aggregates form during the geologic process.

Rock failure is closely related to rock fracture. A number of scholars have applied fracture toughness to the quantitative evaluation of rock engineering stability and safety and have conducted a considerable number of experimental studies. Ciccotti et al. [22] and Saadaoui et al. [23] adopted the double torsion method to experimentally study the static fracture toughness of rocks. Cui et al. [24] comparatively analyzed two test methods for the fracture toughness of chevron-notched rocks. Ayatollahi and Aliha [25] conducted an experimental study of the fracture toughness of brittle rocks under I/II mixed-load modes. Chen and Zhang [26] investigated the fracture toughness of rocks sampled from deep strata by a laboratory test. Erarslan and Williams [27] explored the relationship between the rock fatigue failure

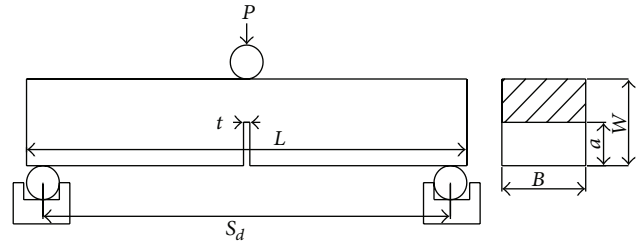


FIGURE 1: Loading sketch of the three-point bending specimens.

mechanism and rock fracture toughness in their study. Apart from the above, deterioration damage in crack rocks in different hydrochemical environments have also drawn great attention from scholars, especially those studying fracture toughness and their rock correlations. However, researches on these topics have rarely been reported in the literature.

The current study conducts several experiments, including three-point bending, uniaxial compression, and tensile splitting strength tests, on Mode-I cracked sandstone specimens under different chemical corrosions. Variation regularities in the physical and mechanical properties, such as P-wave velocity, porosity, fracture toughness K_{Ic} , compressive strength, and splitting tensile strength, of rocks damaged by different chemical solutions are also examined. The main findings of this study shall serve as a decision-making basis for the design and safe operation of the nuclear waste storage library.

2. Introduction of Tests

The granite used in the test was sampled from the hydrofluctuation zone at a typical bank slope located in the Three Gorges Reservoir Region, where the granite featured high homogeneity and integrity. As required by the test procedures [28], rectangular specimens with straight incisions were selected and the three-point bending method was adopted to measure the fracture toughness of the rocks (K_{Ic}). Figure 1 shows the loading diagram. The cross-sectional area was 50 mm × 50 mm, the length was 250 mm × 260 mm, the depth of the straight incision was 21 mm × 23 mm, and the width was 1.0 mm. After processing the specimens, the P-wave velocities of the specimens were measured. The discrete-type specimens were screened out. A total of 68 granite specimens were selected and divided into 17 groups, one of which was used to measure fracture toughness and other related mechanical characteristics of granite under normal conditions. The measurements were used as the initial values for comparative analysis. The remaining 16 groups were employed in the experimental study on a different kind of chemical corrosion.

Before the test, the granite specimens were dried at 105°C to maintain a constant weight and then cooled for mass measurement. The vacuumization method was subsequently adopted to saturate the specimens with 0.01 mol/L of Na_2SO_4 (pH = 3.0) solution, 0.01 mol/L of NaOH (pH = 12.0) solution, 0.01 mol/L of NaHCO_3 (pH = 3.0) solution, and distilled water at pH = 7.0. The chemical solutions used to immerse



FIGURE 2: Sketch map of the acoustic wave detector RSM-SY5.

the specimens should exceed the top of the specimens by 5 cm. The specimens were taken out every month to measure the P-wave velocity and test the fracture toughness. The chemical solutions were exchanged every month. The chemical corrosion time was set to 0, 1, 2, 3, and 4 months, and 4 tests were conducted in parallel for each chemical solution under each test.

To study the relationship between the fracture toughness of specimens and their compressive or splitting tensile strength, several actions were carried out. These procedures included the following: the errors arising out of specimen heterogeneity were reduced, the comparability between the fracture toughness of specimens and their compressive strength or splitting tensile strength was improved under the same conditions, and the two segments of the fractured specimen were processed into a 100 mm rectangular specimen for the uniaxial compression test and into a cylinder specimen with a diameter of 50 mm and a length of 30 mm × 35 mm for the splitting tensile strength test. The physical and mechanical parameters of the specimens were then tested in saturation to further explore the variation regularity.

3. Test Results and Analysis

3.1. Variation Regularity in Porosity and P-Wave Velocity. The P-wave velocity of granite specimens are measured using the acoustic wave detector RSM-SY5 developed by the Institute of Rock and Soil Mechanics, Chinese Academy of Sciences, Wuhan, China. The sketch map of RSM-SY5 sound wave detector is shown in Figure 2. The porosity of specimens is measured by the saturated buoyancy weighing method.

At the beginning of the test, the P-wave velocities and porosities of the saturated granite specimens were measured every month to identify the effects of the different chemical solutions on the physical properties of the specimens. The physical variables that indicated the status of the granite specimens, which included porosity change rate [(porosity after freezing and thawing cycles – initial porosity)/initial porosity] and P-wave velocity change rate [(P-wave velocity at the initial drying – P-wave velocity after freezing and thawing cycles)/P-wave velocity at the initial drying], were defined. The porosity and P-wave velocity change rates of the granite specimens under various chemical solutions at different chemical corrosion times were determined, as shown in Figure 3.

Figure 3 implies that the physical properties of the granite specimens show the same variation trend under different chemical solutions. With the increase of chemical corrosion time, the porosity of the granite specimens gradually increased, whereas the P-wave velocity gradually decreased. Both the porosity and P-wave velocity change rates of the specimens increased as chemical corrosion time increased.

Differences existed in the porosity and P-wave velocity of the granite specimens under different chemical solutions. The porosity and P-wave velocity change rates of the granite specimens were the highest when they were immersed in the 0.01 mol/L Na₂SO₄ (pH = 3.0) solution, rated the lowest when they were submerged in the strong alkaline 0.01 mol/L NaOH (pH = 12.0) solution, and ranked in the middle when they were submersed in distilled water. Hence, the acid solution aggravated the chemical damage deterioration of the granite specimens. However, the strong alkaline solution had a certain inhibiting effect on the chemical damage of the specimens.

Figure 3 also demonstrates that various chemical solutions might have distinct effects on the physical damage in the granite specimens. The effect of the 0.01 mol/L Na₂SO₄ (pH = 3.0) on the porosity and P-wave velocity of the granite specimens was greater than that of the 0.01 mol/L NaHCO₃ (pH = 3.0) under the same conditions, thus indicating that SO₄²⁻ ions aggravated the chemical damage in the specimens.

Figure 4 shows the relationship between the porosity and P-wave velocity of the granite specimens under different water chemical solutions. The diagram illustrates that the porosity of the granite specimens increased under various water chemical solutions, whereas the P-wave velocity showed a gradually deteriorating trend. Therefore, the consistency of both properties was significant, indicating that the P-wave velocity of granite specimens after being chemically corroded could be used to indirectly reflect the porosity change rate.

3.2. Test Result Analysis of the Fracture Toughness K_{IC} of the Granite Specimens. The fracture toughness of the granite specimens under different conditions was calculated on the basis of the K_{IC} computational formula specified in the Rock Test Procedure for Water Resources and Hydropower Engineering [28]. Figure 5 shows the relationship between the K_{IC} of the granite specimens and chemical corrosion time under different water chemical solutions. The computational formula of the fracture toughness K_{IC} is expressed as follows:

$$K_{IC} = 0.25 \frac{S_d P_{max}}{B B^{1.5}} y \left(\frac{a}{B} \right), \quad (1)$$

$$y \left(\frac{a}{B} \right) = \frac{12.75 (a/B)^{0.5} [1 + 19.65 (a/B)^{4.5}]^{0.5}}{(1 - a/B)^{0.25}},$$

where K_{IC} refers to the fracture toughness (MPa·m^{1/2}); B denotes the specimen width (cm), which is equal to the specimen height W (cm); S_d represents the distance between two supporting points (cm); P_{max} symbolizes the load leading to the fracture failure (N); and a indicates the depth of straight

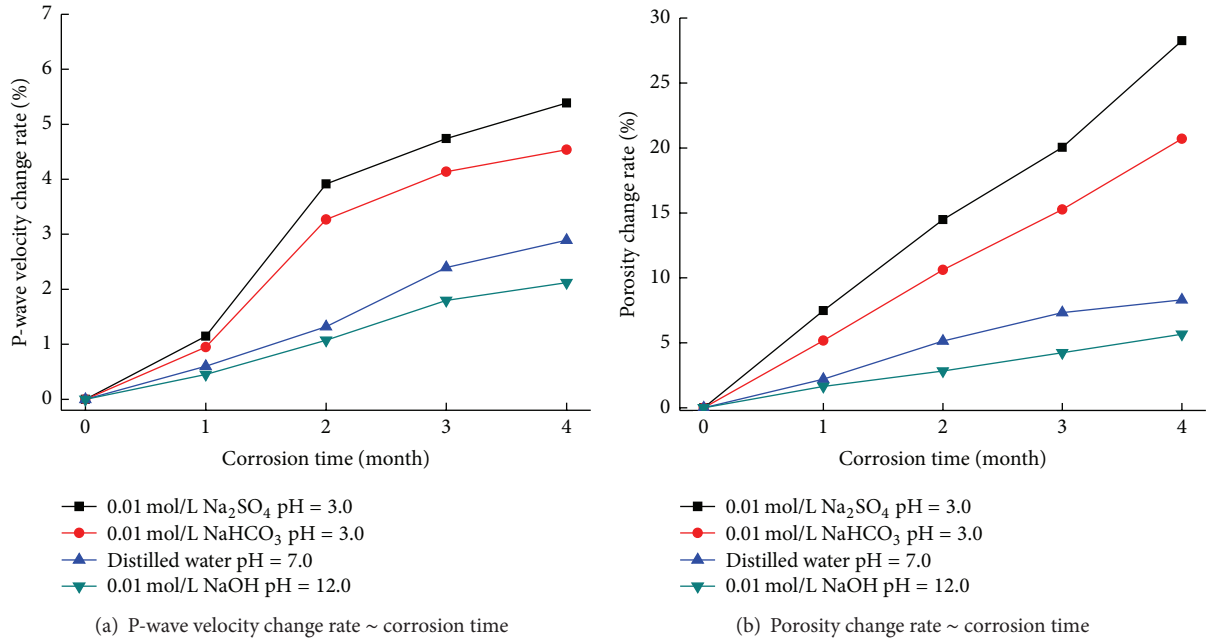


FIGURE 3: Relationships between porosity, P-wave velocity of granite specimens, and corrosion time under different chemical solutions.

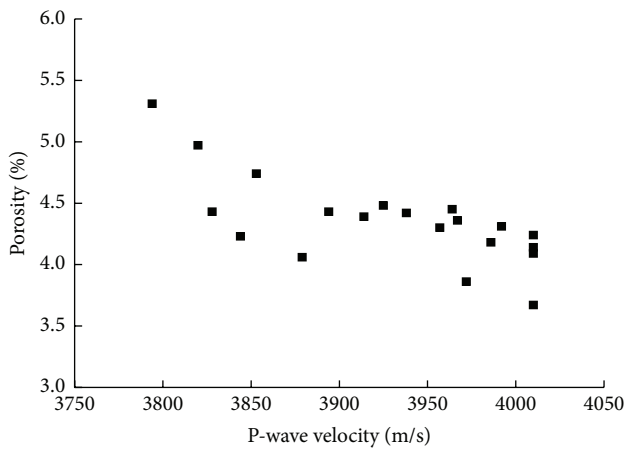


FIGURE 4: Relationship between porosity and P-wave velocity of granite specimens under different chemical solutions.

incision (cm). In this experiment, $S_d = 16.6$ cm, $W = B = 5$ cm, and $a = 22$ mm to 23 mm.

As shown in Figure 5, the granite specimens under different water chemical solutions showed a basically identical trend in fracture toughness K_{IC} as the chemical corrosion time increased. The fracture toughness K_{IC} of the granite specimens presented with varying degrees of deterioration after chemical corrosion. As the chemical corrosion time increased, the deterioration degree also gradually increased. Nevertheless, the degrees of deterioration shown by the granite fracture toughness differed when they were immersed in different chemical solutions.

Meanwhile, the effect of the solution pH value is presented here. The degree of deterioration of the fracture toughness K_{IC} of the granite specimens was the highest when

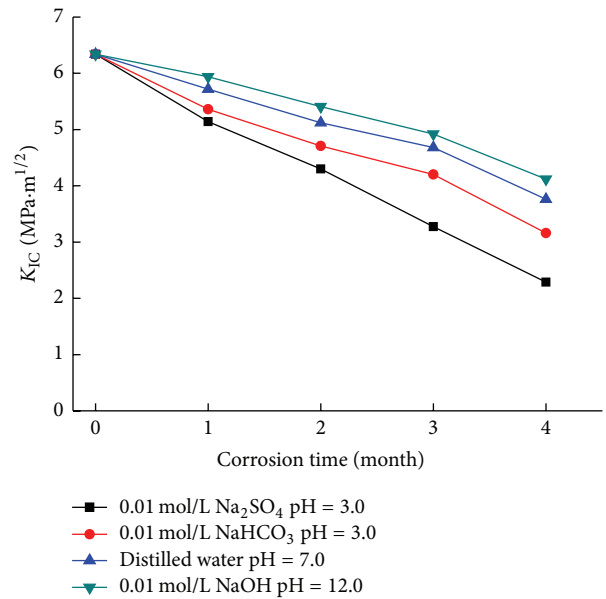


FIGURE 5: Relationship between K_{IC} of granite specimens and corrosion time under different water chemical solutions.

they were immersed in the 0.01 mol/L Na₂SO₄ (pH = 3.0) solution, ranked in the middle when they were submerged in distilled water, and rated the lowest when they were submerged in the 0.01 mol/L NaOH (pH = 12.0) solution. Thus, the acid environment aggravated the deterioration of the granite specimens' fracture toughness. However, the strong alkaline environment had a certain inhibiting effect on the chemical damage deterioration of the granite.

Moreover, as shown in Figure 5, the solutions of different chemical compositions had various effects on the chemical

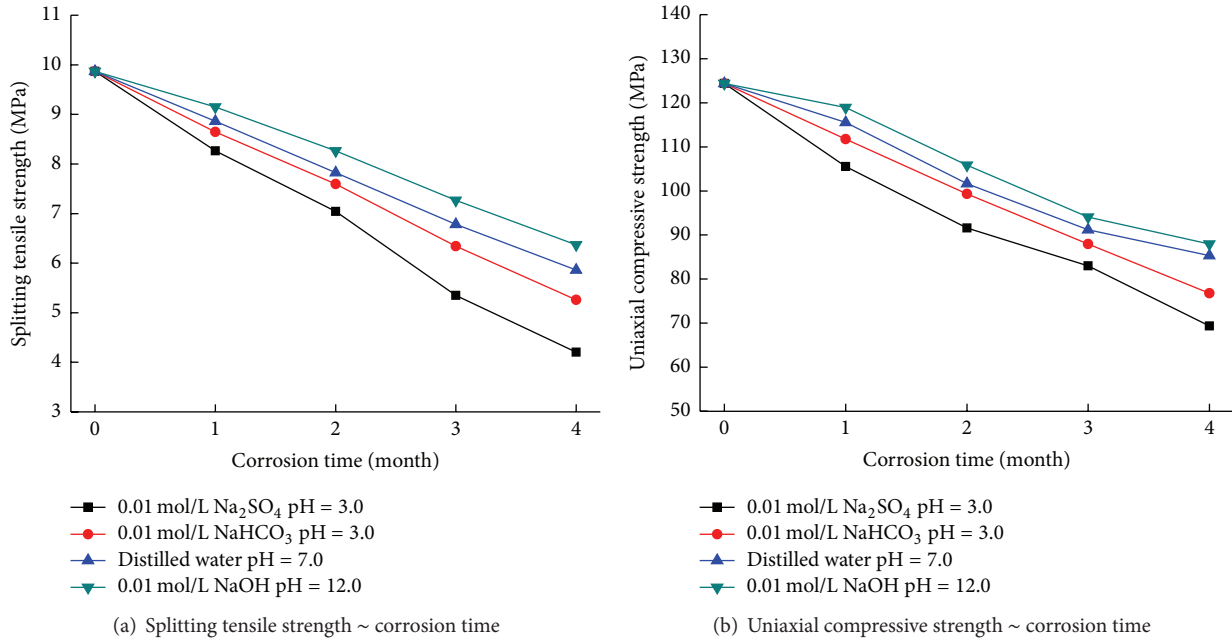


FIGURE 6: Relationships between the granite specimens' splitting tensile strength and uniaxial compressive strength as well as the chemical corrosion time under different water chemical solutions.

damage of the granite fracture toughness K_{IC} , although the acid environment aggravated the deterioration of the fracture toughness K_{IC} of the granite specimens. Under the same chemical corrosion period, the deterioration degree of the granite fracture toughness K_{IC} was lower in 0.01 mol/L NaHCO₃ (pH = 3.0) than in 0.01 mol/L Na₂SO₄ (pH = 3.0). Hence, SO₄²⁻ ions had a greater effect on the chemical damage of granite specimens than HCO₃⁻ ions.

3.3. Analysis of the Tensile and Compressive Test Results of Granite Specimens. Figure 6 shows the relationships among the granite specimens' splitting tensile strength and uniaxial compressive strength as well as the chemical corrosion time under different water chemical solutions.

As seen in Figure 6, as the chemical corrosion time increased, the splitting tensile strength and compressive strength of the granite specimens showed gradually deteriorating trends under different water chemical solutions. However, differences existed in the deterioration degrees of the splitting tensile strength and compressive strength of the specimens when they were immersed in different water chemical solutions.

When the solution concentration and pH value remained unchanged, the chemical deterioration degrees of the tensile strength and compressive strength of granite specimens were higher in 0.01 mol/L Na₂SO₄ (pH = 3.0) than in pH = 7.0 distilled water and in 0.01 mol/L NaOH (pH = 12.0). The deterioration degrees of the tensile strength and compressive strength of the granite specimens were also higher in pH = 7.0 distilled water than in the alkaline 0.01 mol/L NaOH (pH = 12.0) solution. Therefore, the strong acid solution aggravated the chemical damage deterioration of the tensile strength and compressive strength of the granite. On the contrary, in

the strong alkaline environment (NaOH solution), a certain inhibiting effect existed to mitigate the chemical damage deterioration of the granite specimens.

When the solution concentration and pH value remained unchanged, the chemical damage deterioration degrees of the tensile strength and compressive strength of the granite specimens were higher in the 0.01 mol/L Na₂SO₄ (pH = 3.0) solution than in the 0.01 mol/L NaHCO₃ (pH = 3.0) solution. Therefore, SO₄²⁻ ions aggravated the chemical deterioration degrees of the tensile strength and compressive strength of the granite specimens.

3.4. Analysis of the Relations between the Splitting Tensile Strength, Uniaxial Compressive Strength, and K_{IC} of the Granite Specimens. Previous studies have reported existing relations between the strength characteristics and fracture toughness of rocks. In the current study, the relationships between the splitting tensile strength, uniaxial compressive strength, and fracture toughness K_{IC} of the granite specimens were evaluated based on the summary of the test data in this study. The results are shown in Figure 7.

Based on the diagram shown in Figure 7, a linear relationship existed between the splitting tensile strength and K_{IC} and between the uniaxial compressive strength and K_{IC} of granite specimens that were damaged under different chemical solutions. The relations could be, respectively, expressed as follows:

$$K_{IC} = 0.6746\sigma_t - 0.2732, \tag{2}$$

$$R^2 = 0.9797,$$

$$K_{IC} = 0.06646\sigma_c - 1.8555, \tag{3}$$

$$R^2 = 0.9549,$$

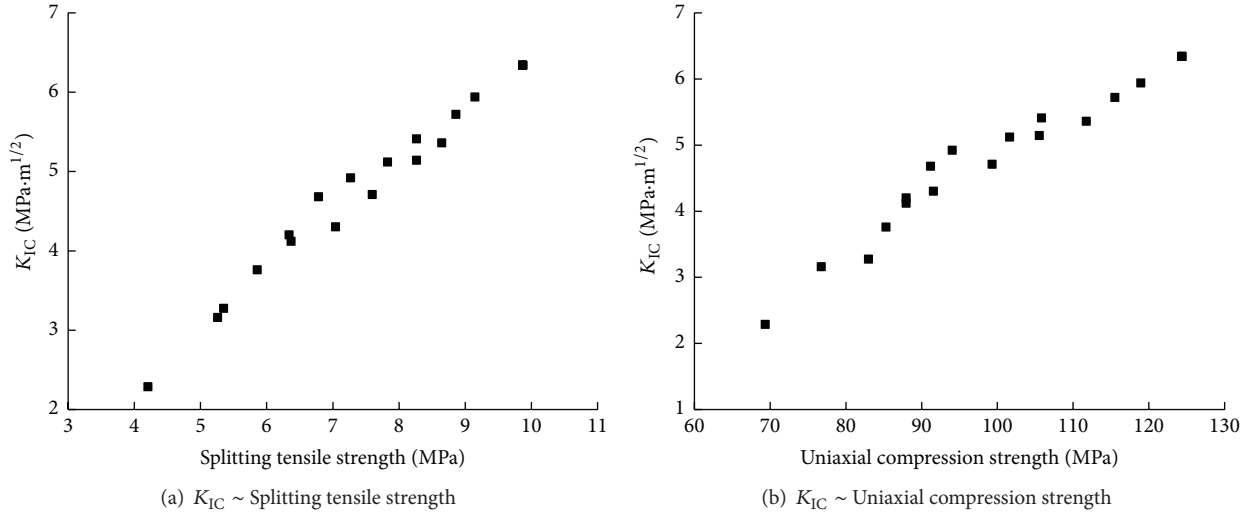


FIGURE 7: Relationship between splitting tensile strength, uniaxial compressive strength, and K_{IC} of granite specimens.

where σ denotes the uniaxial compressive strength of the granite specimens, and σ_t refers to the splitting tensile strength of the granite specimens.

To gain a better understanding of the effects of chemical solutions on the chemical damage degrees of fracture toughness, splitting tensile strength, and uniaxial compressive strength of the granite specimens, the chemical damage factor K_{cf} can be defined as follows:

$$K_{cf} = \frac{f_0 - f_N}{f_0} \times 100\%, \quad (4)$$

where f_0 denotes the mechanical characteristic value of the granite specimens under normal conditions, and f_N refers to the mechanical characteristic value of the granite specimens when they underwent N months chemical corrosion. A high K_{cf} indicates weak resistance capacity of the granite specimens against chemical corrosion.

Figure 8 shows the relationship between the deterioration rate of mechanical characteristics (including fracture toughness, splitting tensile strength, and uniaxial compressive strength of the granite specimens) and the chemical corrosion time identified based on (4) under different water chemical solutions.

Local and international scholars, such as Zhang et al. [29, 30], Golshani et al. [30–32], and Deng et al. [33, 34], have explored the relationship between fracture toughness and tensile strength of rocks. Their findings showed a linear relationship between fracture toughness K_{IC} and tensile strength of granite. Deng et al. [34] deduced a formula to explain the relationship between fracture toughness K_{IC} and tensile strength for Mode-I cracked rocks. This formula is expressed as

$$r = \frac{1}{2\pi} \left(\frac{K_{IC}}{\sigma_t} \right)^2, \quad (5)$$

where r denotes the crack propagation radius.

The findings in the literature [30–33] state that the crack propagation radius is large and small when the rock strength is high and low, respectively. In the current study, the crack propagation radius of granite specimens was analyzed under the test conditions specified here to evaluate the effects of different chemical solutions on the crack propagation radius of rocks. The results are shown in Figure 9.

As shown in Figure 9, after the effect of chemical corrosion, the crack propagation radius of the granite specimens generally showed a gradually decreasing trend, indirectly indicating that the strength characteristics of the granite specimens had an increasing deterioration tendency. The results were consistent with the analysis of the deterioration regularity in the splitting tensile strength and the compressive strength of the granite specimens. Equation (5) indicates that the deterioration degree of the specimen fracture toughness is significantly higher than that of the splitting tensile strength when the splitting tensile strength and crack propagation radius of the granite specimens simultaneously decrease. This condition serves as a good explanation for the test phenomenon in Figure 8; that is, the deterioration degree of the specimen fracture toughness is the highest, followed by those of the splitting tensile strength and compressive strength the lowest.

4. Analysis of the Damage Variable Mechanism under Chemical Corrosion

4.1. Damage Variable. Based on the preceding analysis on the damage deterioration degree of granite specimens under the effect of chemical solutions, the damage variable D can be expressed according to the changes in porosity given by

$$D = \frac{n_N - n_0}{1 - n_0}, \quad (6)$$

where n_0 denotes the porosity of the granite specimens at the initial state, and n_N refers to the porosity of the granite

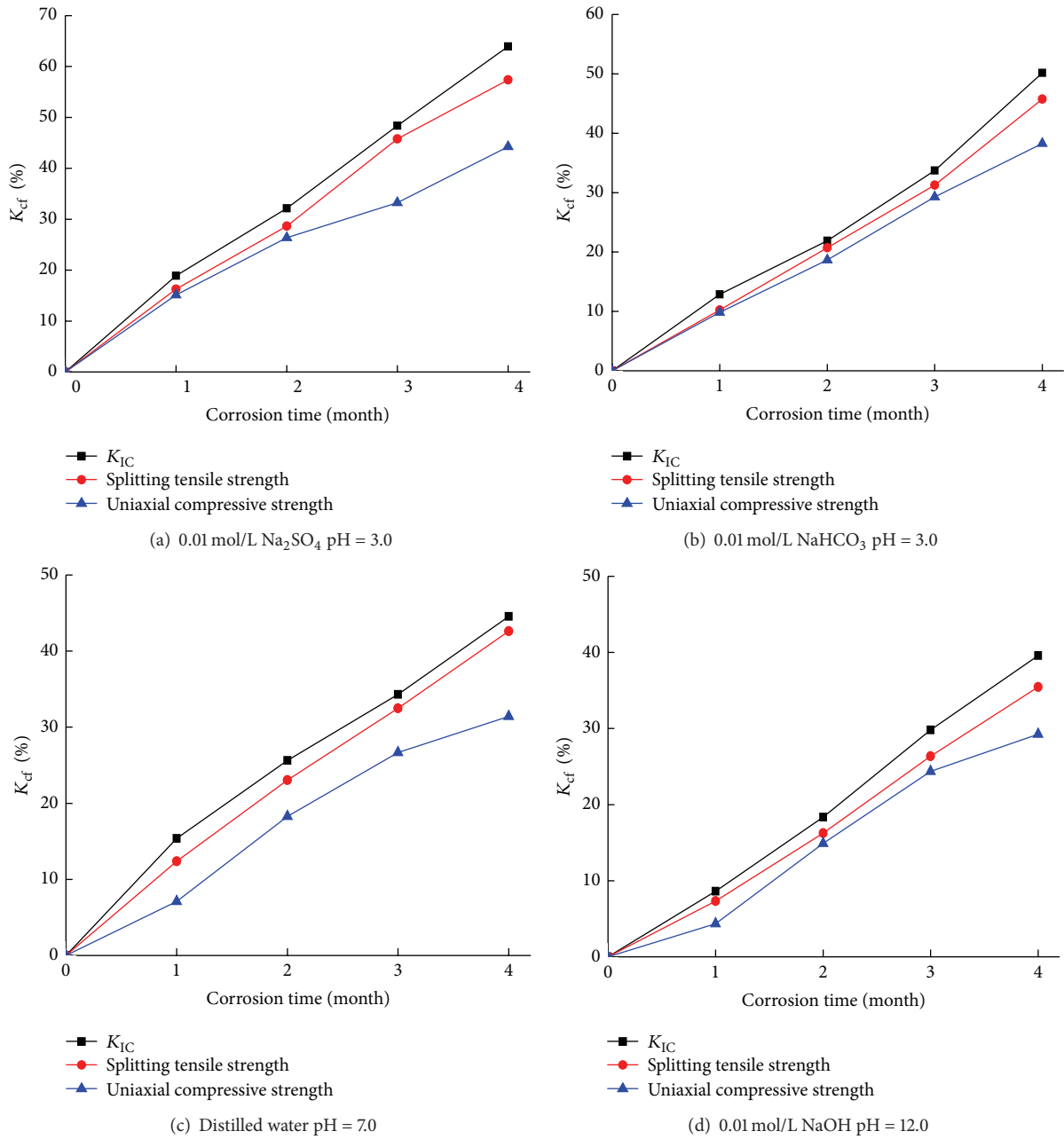


FIGURE 8: Relationship between the deterioration rate of the mechanical characteristics of granite specimens and corrosion time under different water chemical solutions.

specimens under the effect of chemical corrosion after N months of chemical corrosion.

The damage variable of the granite specimens under the effects of different chemical solutions for different chemical corrosion times was evaluated based on (6). The results are shown in Figure 9. As shown in the diagram, as the chemical corrosion time increased, the damage variable of the granite specimens under different conditions gradually increased. A certain distinction existed in the variation regularity in the damage variable when the specimens were immersed in different chemical solutions.

The damage variable of the granite specimens was higher in the 0.01 mol/L Na_2SO_4 (pH = 3.0) solution than in the

alkaline 0.01 mol/L NaOH (pH = 12.0) solution or in the pH = 7.0 distilled water. The damage variable of the specimens in the alkaline 0.01 mol/L NaOH (pH = 12.0) solution was the lowest; that is, $D_{\text{Na}_2\text{SO}_4} > D_{\text{Distilled water}} > D_{\text{NaOH}}$. Thus, the 0.01 mol/L Na_2SO_4 (pH = 3.0) solution aggravates the chemical damage deterioration of the granite. By contrast, the NaOH solution had a certain inhibiting effect on the chemical damage deterioration of the granite specimens.

When the solution concentration and pH value remained unchanged, the chemical damage deterioration degrees of the tensile strength and compressive strength of the granite specimens were higher in the 0.01 mol/L Na_2SO_4 (pH = 3.0) solution than in the 0.01 mol/L NaHCO_3 (pH = 3.0) solution.

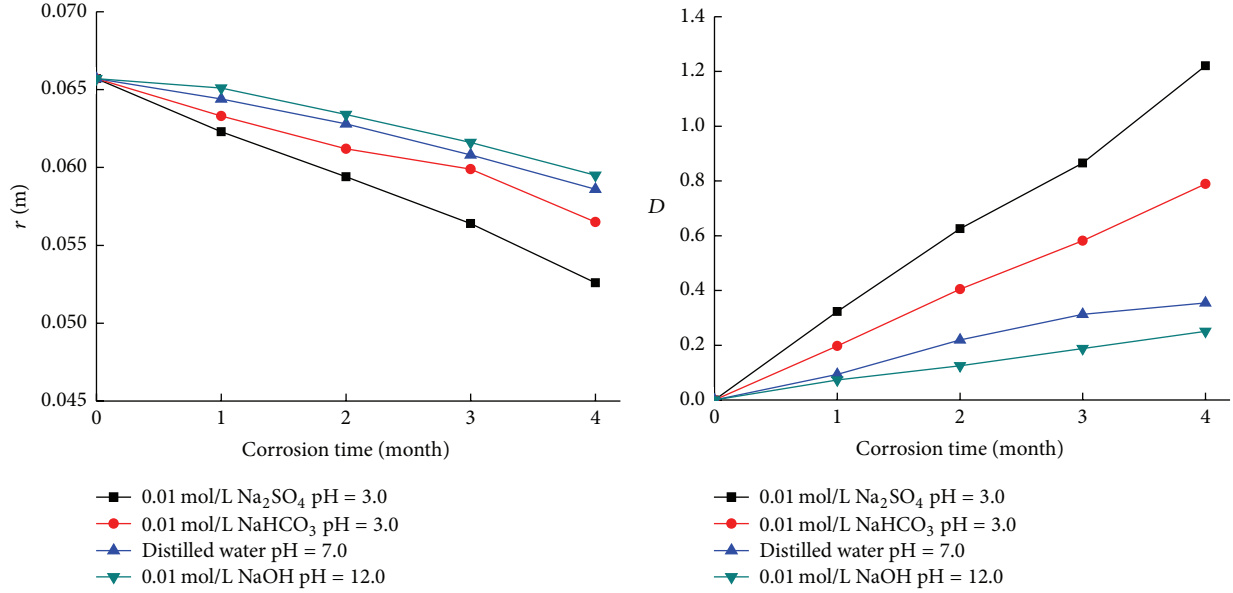


FIGURE 9: Relationships between crack propagation radii, damage variable of granite specimens, and corrosion time under different water chemical solutions.

Therefore, SO_4^{2-} ions aggravated the chemical deterioration degrees of the tensile strength and compressive strength of the granite specimens.

4.2. Effect of Chemical Corrosion Damage on the Mechanical Parameters of the Granite Specimens. The damage variable for the granite specimens that underwent different chemical corrosion times in various chemical conditions was calculated based on (6). Figure 10 shows the relationship between the damage variable and physical mechanical parameters, including P-wave velocity, fracture toughness K_{IC} , splitting tensile strength, and compressive strength of the granite specimens.

As shown in Figure 10, the P-wave velocity, fracture toughness K_{IC} , splitting tensile strength, and compressive strength of the granite specimens affected by chemical solutions gradually deteriorated as the damage of the specimens became increasingly severe. Consequently, chemical corrosion led to the gradual deterioration of the specimens. Moreover, as the chemical corrosion time increased, the damage deterioration of specimens also increased. The accumulated damage might result in the deterioration of the physical and mechanical parameters of the granite to varying extent.

Linear regression was conducted for Figure 10. The respective relationships between the mechanical parameters and the damage variable of the granite specimens were obtained as follows:

$$K_{IC} = 6.2546e^{-0.7815D}, \quad (7)$$

$$R^2 = 0.9478,$$

$$\sigma_t = 9.509e^{-0.6728D}, \quad (8)$$

$$R^2 = 0.9260,$$

$$\sigma = 120.26e^{-0.4834D}, \quad (9)$$

$$R^2 = 0.9723,$$

$$v_p = -238.58D + 4001.2, \quad (10)$$

$$R^2 = 0.9478.$$

5. The Engineering Properties of Marble after Chemical Solutions

The engineering properties of a rock mass are described by the relevant quantitative physical and mechanical properties. Accordingly, this test data was validated by calculating two parameters, the saturated uniaxial compressive strength (R_c), and the weathering reduction factor of strength, respectively.

The degree of rock hardness is determined by the saturated uniaxial compressive strength of the rock. The hardness degree of our granite specimens immersed in the chemical solutions was divided based on the standard specified in the Standard for Engineering Classification of Rock Masses (2014), GB/T 50218-2014. The results show that the hardness degree of granite specimens subjected to various degrees of deterioration after chemical solution was less than that of natural sandstone.

The weathering reduction factor of strength is equal to the strength of granite after chemical corrosion, divided by its initial natural strength. Statistical analysis of test results showed that the weathering degree of natural granite was weak weathering, but that of the granite specimens was aggravated after the chemical corrosion. With the chemical etching time increased, the weathering degree of granite gradually increased. Nevertheless, the weathering degree of the specimens differed when they were immersed in different chemical solutions, causing differing weathering

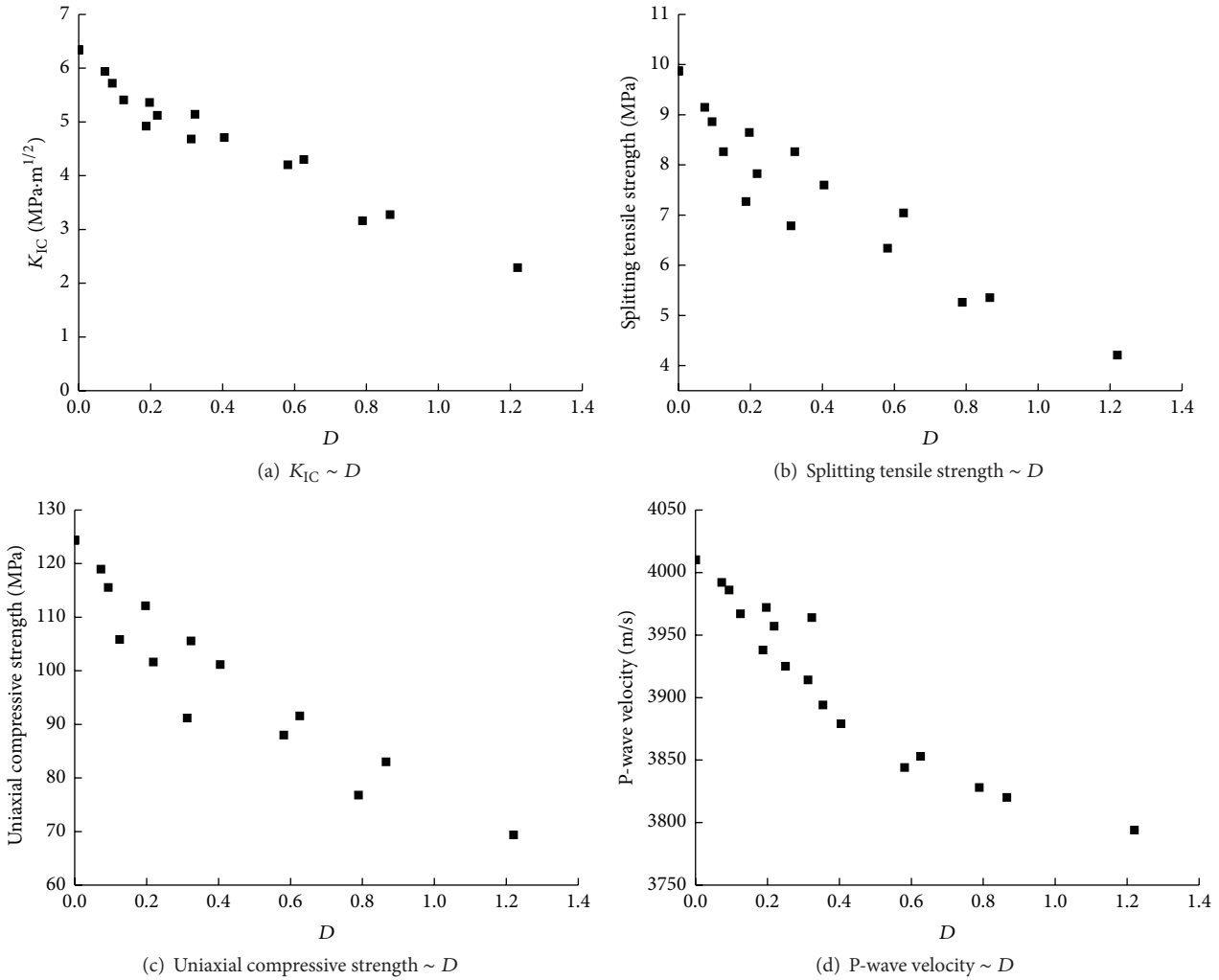


FIGURE 10: Relationship between physical and mechanical parameters and damage variable of marble specimens.

degrees with corrosion time. The greater the influence of chemical solutions on the deterioration degree of granite, the earlier the chemical etching time happened. The weathering degree of granite specimens converted from weak weathering to moderate weathering in different chemical solutions. Because the deterioration degree of granite was greater in the 0.01 mol/L Na_2SO_4 (pH = 3.0) and 0.01 mol/L NaHCO_3 (pH = 3.0) solutions than that in the 0.01 mol/L NaOH (pH = 12.0) and distilled water, strong weathering of granite in 0.01 mol/L Na_2SO_4 (pH = 3.0) and 0.01 mol/L NaHCO_3 (pH = 3.0) solutions happened one month earlier than that in 0.01 mol/L NaOH (pH = 12.0) solution and two months than in distilled water.

6. Conclusions

(1) Granite specimens under the effects of different chemical solutions showed an overall remarkably weakening trend. The splitting tensile strength, compressive strength, and K_{IC} of the specimens displayed a roughly identical deteriorating trend as the chemical corrosion time increased. However, variations

in the deterioration degrees of the mechanical parameters were observed. The deterioration degree of fracture toughness was the highest, followed by those of splitting tensile strength and compressive strength is the lowest.

(2) Different effects of various chemical solutions on the chemical damage deterioration degree of the granite specimens were observed. The 0.01 mol/L Na_2SO_4 (pH = 3.0) solution aggravated the chemical damage deterioration of the granite specimens. By contrast, the 0.01 mol/L NaOH (pH = 12.0) solution had a certain inhibiting effect on the granite specimens. Moreover, the 0.01 mol/L Na_2SO_4 (pH = 3.0) solution had a greater effect on the chemical damage deterioration degree of the granite specimens than the 0.01 mol/L NaHCO_3 (pH = 3.0) solution. Hence, SO_4^{2-} ions could aggravate the damage deterioration of the granite specimens.

(3) A good linear relationship existed between the fracture toughness K_{IC} , splitting tensile strength, and compressive strength of the granite specimens that underwent chemical corrosion. After being affected by chemical solutions, the crack propagation radius of the granite specimens generally

showed a gradually decreasing trend. Such a result indirectly indicated that the strength characteristics of the granite specimens had a gradually deteriorating trend.

(4) The damage variable was established based on the changes in the porosities of the granite specimens. The damage variable gradually increased as the chemical corrosion time increased. As the damage of the specimens became increasingly severe, the K_{IC} , splitting tensile strength, compressive strength, and P-wave velocity of the granite specimens affected by the chemical solutions also gradually deteriorated. The relationships between the fracture toughness K_{IC} , splitting tensile strength, compressive strength of the specimens, and damage variable showed an exponential function, whereas the relations between the P-wave velocity of the granite specimens and the damage variable were linear.

Competing Interests

The authors declare that they have no competing interests.

Acknowledgments

The authors gratefully acknowledge the support of the National Natural Science Foundation of China (nos. 11302167 and 10972180).

References

- [1] J. Rutqvist, L. Börgesson, M. Chijimatsu et al., "Thermohydromechanics of partially saturated geological media: governing equations and formulation of four finite element models," *International Journal of Rock Mechanics and Mining Sciences*, vol. 38, no. 1, pp. 105–127, 2001.
- [2] V. Guvanasen and T. Chan, "A new three-dimensional finite element analysis of hysteresis thermohydromechanical deformation of fractured rock mass with dilatance in fractures," in *Proceedings of the 2nd Conference on Mechanics of Jointed and Faulted Rocks*, pp. 347–442, Vienna, Austria, April 1995.
- [3] Y. Ohnishi and A. Kobayashi, "Thames," in *Coupled Thermo-Hydro-Mechanical Processes of Fractured Media*, O. Stephansson, L. Jing, and C.-F. Tsang, Eds., vol. 79, pp. 545–549, Elsevier, 1996.
- [4] A. Millard, A. Rejeb, M. Chijimatsu et al., "Numerical study of the THM effects on the near-field safety of a hypothetical nuclear waste repository—BMT1 of the DECOVALEX III project. Part 2: effects of THM coupling in continuous and homogeneous rocks," *International Journal of Rock Mechanics and Mining Sciences*, vol. 42, no. 5–6, pp. 731–744, 2005.
- [5] P. Blum, R. Mackay, M. S. Riley, and J. L. Knight, "Performance assessment of a nuclear waste repository: upscaling coupled hydro-mechanical properties for far-field transport analysis," *International Journal of Rock Mechanics and Mining Sciences*, vol. 42, no. 5–6, pp. 781–792, 2005.
- [6] Y. J. Zhang, "Coupled thermo-hydro-mechanical model and 2D FEM analysis for FEBEX in-situ test," *Chinese Journal of Geotechnical Engineering*, vol. 29, no. 3, pp. 313–318, 2007 (Chinese).
- [7] B. K. Atkinson, "A fracture mechanics study of subcritical tensile cracking of quartz in wet environments," *Pure and Applied Geophysics*, vol. 117, no. 5, pp. 1011–1024, 1979.
- [8] B. K. Atkinson, "Subcritical crack growth in geological materials," *Journal of Geophysical Research*, vol. 89, no. 6, pp. 4077–4114, 1984.
- [9] R. J. Martin, "Time-dependent crack growth in quartz and its application to the creep of rocks," *Journal of Geophysical Research*, vol. 77, no. 8, pp. 1406–1419, 1972.
- [10] R. J. Charles, "Static fatigue of glass. II," *Journal of Applied Physics*, vol. 29, no. 11, pp. 1554–1560, 1958.
- [11] S. W. Freiman, "Effects of chemical environments on slow crack growth in glasses and ceramics," *Journal of Geophysical Research*, vol. 89, no. 6, pp. 4072–4076, 1984.
- [12] B. R. Lawn, M. V. Swain, and K. Phillips, "On the mode of chipping fracture in brittle solids," *Journal of Materials Science*, vol. 10, no. 7, pp. 1236–1239, 1975.
- [13] B. K. Atkinson and P. G. Meredith, "Stress corrosion cracking of quartz: a note on the influence of chemical environment," *Tectonophysics*, vol. 77, no. 1–2, pp. 1–11, 1981.
- [14] S. H. Kirby, "Introduction and digest to the special issue on chemical effects of water on the deformation and strengths of rocks," *Journal of Geophysical Research*, vol. 89, no. 6, pp. 3991–3995, 1984.
- [15] J. R. Bulau, B. R. Tittmann, M. Abdel-Gawad, and C. Salvado, "Role of aqueous fluids in the internal friction of rock," *Journal of Geophysical Research*, vol. 89, no. 6, pp. 4207–4212, 1982.
- [16] C. J. Simmons and S. W. Freiman, "Effect of corrosion processes on subcritical crack growth in glass," *Journal of the American Ceramic Society*, vol. 64, no. 11, pp. 683–686, 1981.
- [17] N. G. Swoboda-Colberg and J. I. Drever, "Mineral dissolution rates in plot-scale field and laboratory experiments," *Chemical Geology*, vol. 105, no. 1–3, pp. 51–69, 1993.
- [18] T. A. Michalske and S. W. Freiman, "A molecular interpretation of stress corrosion in silica," *Nature*, vol. 295, no. 5849, pp. 511–512, 1982.
- [19] E. Z. Lajtai, R. H. Schmidtke, and L. P. Bielus, "The effect of the time-dependent deformation and fracture of granite," *International Journal of Rock Mechanics and Mining Science & Geomechanics Abstracts*, vol. 24, no. 4, pp. 247–255, 1987.
- [20] J. Dunning, B. Douglas, M. Miller, and S. McDonald, "The role of the chemical environment in frictional deformation: stress corrosion cracking and comminution," *Pure and Applied Geophysics*, vol. 143, no. 1, pp. 151–178, 1994.
- [21] L. Ning, Z. Yunming, S. Bo, and S. Gunter, "A chemical damage model of sandstone in acid solution," *International Journal of Rock Mechanics and Mining Sciences*, vol. 40, no. 2, pp. 243–249, 2003.
- [22] M. Ciccotti, G. Gonzato, and F. Mulargia, "The double torsion loading configuration for fracture propagation: an improved methodology for the load-relaxation at constant displacement," *International Journal of Rock Mechanics and Mining Sciences*, vol. 37, no. 7, pp. 1103–1113, 2000.
- [23] M. Saadaoui, P. Reynaud, G. Fantozzi, F. Peronnet, and J. P. Caspar, "Slow crack growth study of plaster using the double torsion method," *Ceramics International*, vol. 26, no. 4, pp. 435–439, 2000.
- [24] Z. D. Cui, D. A. Liu, G. M. An, B. Sun, M. Zhou, and F. Q. Cao, "A comparison of two ISRM suggested chevron notched specimens for testing mode-I rock fracture toughness," *International Journal of Rock Mechanics and Mining Sciences*, vol. 47, no. 5, pp. 871–876, 2010.
- [25] M. R. Ayatollahi and M. R. M. Aliha, "Fracture toughness study for a brittle rock subjected to mixed mode I/II loading,"

- International Journal of Rock Mechanics and Mining Sciences*, vol. 44, no. 4, pp. 617–624, 2007.
- [26] M. Chen and G.-Q. Zhang, “Laboratory measurement and interpretation of the fracture toughness of formation rocks at great depth,” *Journal of Petroleum Science and Engineering*, vol. 41, no. 1–3, pp. 221–231, 2004.
- [27] N. Erarslan and D. J. Williams, “The damage mechanism of rock fatigue and its relationship to the fracture toughness of rocks,” *International Journal of Rock Mechanics and Mining Sciences*, vol. 56, pp. 15–26, 2012.
- [28] The Professional Standard Compilation Group of People’s Republic of China, *DL/T5368-2007 Specifications for Rock Tests in Water Conservancy and Hydroelectric Engineering*, China Water Power Press, 2007 (Chinese).
- [29] Z. X. Zhang, “An empirical relation between mode I fracture toughness and the tensile strength of rock,” *International Journal of Rock Mechanics and Mining Sciences*, vol. 39, no. 3, pp. 401–406, 2002.
- [30] Z. X. Zhang, S. Q. Kou, P. A. Lindqvist et al., “The relationship between the fracture toughness and tensile strength of rock,” in *Strength Theory: Application, Development & Prospects for 21st Century*, pp. 215–223, Science Press, Beijing, China, 1988.
- [31] A. Golshani, Y. Okui, M. Oda, and T. Takemura, “A micromechanical model for brittle failure of rock and its relation to crack growth observed in triaxial compression tests of granite,” *Mechanics of Materials*, vol. 38, no. 4, pp. 287–303, 2006.
- [32] A. Golshani, M. Oda, Y. Okui, T. Takemura, and E. Munkhtogoo, “Numerical simulation of the excavation damaged zone around an opening in brittle rock,” *International Journal of Rock Mechanics and Mining Sciences*, vol. 44, no. 6, pp. 835–845, 2007.
- [33] H. F. Deng, J. L. Li, M. Zhu, X. F. Yuan, and Q. Luo, “Experimental research on fracture mechanical effect of sandstone under water corrosion,” *Chinese Journal of Rock Mechanics and Engineering*, vol. 31, no. 7, pp. 1342–1348, 2012 (Chinese).
- [34] H. F. Deng, M. Zhu, J. L. Li, Y. Wang, Q. Luo, and X. F. Yuan, “Study of mode-I fracture toughness and its correlation with strength parameters of granite,” *Chinese Journal of Rock and Soil Mechanics*, vol. 33, no. 12, pp. 3585–3591, 2012 (Chinese).